Title
Micro-scale Processing of Silk Protein

Author
Breslauer, David Nate

Publication Date
2010

Peer reviewed|Thesis/dissertation

Micro-scale Processing of Silk Protein

by

David Nate Breslauer

A dissertation submitted in partial satisfaction of the

requirements for the degree of

Joint Doctor of Philosophy
with University of California, San Francisco

in

Bioengineering

in the

Graduate Division

of the

University of California, Berkeley

Committee in charge:

Professor Luke P. Lee, Chair
Professor Susan J. Muller
Professor Jay T. Groves
Professor Tejal A. Desai

Spring 2010

Abstract

Micro-scale Processing of Silk Protein

by

David Nate Breslauer

Joint Doctor of Philosophy
with University of California, San Francisco

University of California, Berkeley

Professor Luke P. Lee, Chair

Silkworm silk fibers have been in use for over 5000 years in clothing and textiles. These fibers are unwound from the cocoon that is spun by the worm to protect itself during metamorphosis. More recently, spider silk has received a significant amount of research attention due to its exceptional mechanical properties. Spider silk has a breaking strength comparable to steel (>1GPa), and an extensibility closer to nylon (>30%), giving it an extremely high toughness (energy to breakage). Unlike silkworms, however, spiders cannot be farmed for mass silk cultivation. Therefore, a tremendous amount of effort has been put forth toward understanding how silk fibers are spun, and how to reproduce them artificially. The problem is two-fold: silk protein must be obtained (generally through dissolution of cocoons) and that protein must be spun into a fiber. All spinning efforts to date have failed to produce native-quality fibers, and it has become apparent that the complexity of the silk gland is crucial to replicate during the spinning process. Furthermore, efforts to process silk proteins have led to the realization that silk protein provides a unique platform material for a wide variety of biotechnologies. This dissertation focusses on the processing of silk proteins into fibers and various microstructures. Simulations of flow in the spider and silkworm silk gland demonstrate the importance of gland geometry on fiber formation. A hydrodynamic focussing system is developed to spin silkworm fibers, as well as extended to form silk microspheres. A biomimetic microfluidic system is developed that mimics the silk gland geometry and also allows mass transport into and out of the silk solution during spinning. Finally, dissolved silkworm silk is demonstrated to be a useful material for the high fidelity and high aspect ratio molding of nano- and micro-structures.

Acknowledgements

I have always wanted to pursue research and my own ideas, and my time in the UC Berkeley/UCSF Bioengineering Graduate Group has given me the opportunity to do so. I am grateful to my advisor, Luke Lee, for allowing me total freedom in lab to do as I pleased, and always being primarily concerned with my personal and professional growth. Luke has supported me throughout all my research endeavors, even when our research passions diverged (i.e. I became obsessed with silk.) I am extremely grateful to have met Susan Muller in my early years of graduate school. Susan has been an indispensable intellectual resource, an excellent co-advisor, and a fun person with whom to interact. As with Luke, Susan stood behind all my research endeavors, no matter how tangential to my thesis work. I am also appreciative to have had Dorian Liepmann as a graduate advisor and friend in the department; his enthusiasm is contagious. Lastly, as a brief research aside (the CellScope), I had the pleasure of working with Dan Fletcher, who is a brilliant scientist, engineer, and team manager. The UC Berkeley Bioengineering staff and lecturers are just as deserving of mention: Rebecca, Pam, Jennifer, Catherine, Terry, Megan, Amy, Tere, Mona, Cindy, Allison, and Lindsay. Without them, I do not know how anything would get done.

My time in graduate school and the BioPOETS lab falls into two generations. In my first two to three years, I was young and new. I thank my friends and labmates from that time for helping me grow: Michelle Khine, Tanner Nevill, Dino Di Carlo, and Shelly Gulati. I am still friends with these people, and they continue to provide me with support and guidance. Somewhere halfway through my third year, I started to become a “senior student” and people began coming to me for advice and support. I feel privileged to have had some wonderful labmates and friends: Frankie Myers, Rick Henrikson, John Waldeisen, Brendan Turner, Eric Lee, Liz Wu, Sisi Chen, and Debkishore Mitra.

I would like to thank my friends, outside of lab and graduate school, for their support: Peter White, David Casterton, Jeremy Krompier, Dan Cohen, Matt Crow, and Jill Gersh. Most importantly, I thank my loving parents (George and Yvette), sister (Michelle), and the rest of my family who have never doubted my abilities and have supported me unconditionally.

Finally, I extend my most sincere gratitude to JJH. She has helped me get to where I am and to where I will be.

Table of Contents

Chapter 1. Introduction to Silk: Proteins, Processing, and Fibers 1
1.1 Overview 2
1.2 Silk Protein 4
1.3 Silk in Solution Form (Silk “Dope”) 4
1.4 *In Vivo* Silk Spinning 5
1.5 Silk Fibers 8
1.6 Sources of Silk Protein used in Experiments 10
1.7 Spinning Artificial Silk Fibers 11
1.8 Other Microscale Uses of Silk 16
1.9 Scope of the Dissertation 20
Chapter 2. Simulation of Flow in the Silk Gland 21
2.1 Abstract 22
2.2 Introduction 22
2.3 Methods Section 23
2.4 Results and Discussion 25
2.5 Conclusions 39
2.6 Acknowledgment 40
Chapter 3. Laminar Flow Focusing of Silk 41
3.1 Abstract 42
3.2 Introduction 42
3.3 Experimental 43
3.4 Results and Discussion 44
3.5 Summary 50
3.6 Acknowledgement 51
Chapter 4. A Biomimetic Microfluidic Silk Gland 52
4.1 Abstract 53
4.2 Introduction 53
4.3 Experimental 54
4.4 Results 56
4.5 Discussion and Future Work 62
4.6 Acknowledgement 63
Chapter 5. Generation of Monodisperse Silk Microspheres Prepared with Microfluidics 64
5.1 Abstract 65
5.2 Introduction 65
5.3 Experimental 66
5.4 Results and Discussion 67
5.5 Conclusions 72
5.6 Acknowledgment 73
Chapter 6. High Fidelity and High Aspect Ratio Silk Nano- and Micro-molding 74
6.1 Abstract 75

6.2 Introduction 75
6.3 Experimental 76
6.4 Results and Discussion 77
6.8 Conclusions 82
6.9 Acknowledgement 82
Chapter 7. Concluding Remarks 84
References 87
Appendices 94
Appendix A - Preparation of Aqueous *Bombyx Mori* Silk Solution 95
Appendix B - Preparation of Concentrated (20-30%) Aqueous *Bombyx Mori* Silk Solution 99
Appendix C - Raising and Dissecting Silkworms 101
Appendix D - Fiber Mechanical Tester 103

Chapter 1. Introduction to Silk: Proteins, Processing, and Fibers

1.1 Overview

Silk is a fine and lustrous fiber, produced by several insects, most notably silkworms and spiders (Vollrath and Knight 2001). Silkworms produce silk to form cocoons within which they metamorphosize into moths (Figure 1a). The 5000 year old sericulture industry has completely domesticated the *Bombyx Mori* silkworm and has perfected the art of unreeling these cocoons into their single fiber components to be woven into fabrics. Orb weaving spiders, on the other hand, produce up to seven different kinds of silk per individual, with the chemical composition and mechanical properties of each type of silk tailored for its specific use (Vollrath and Knight 2001) (Figure 1b).

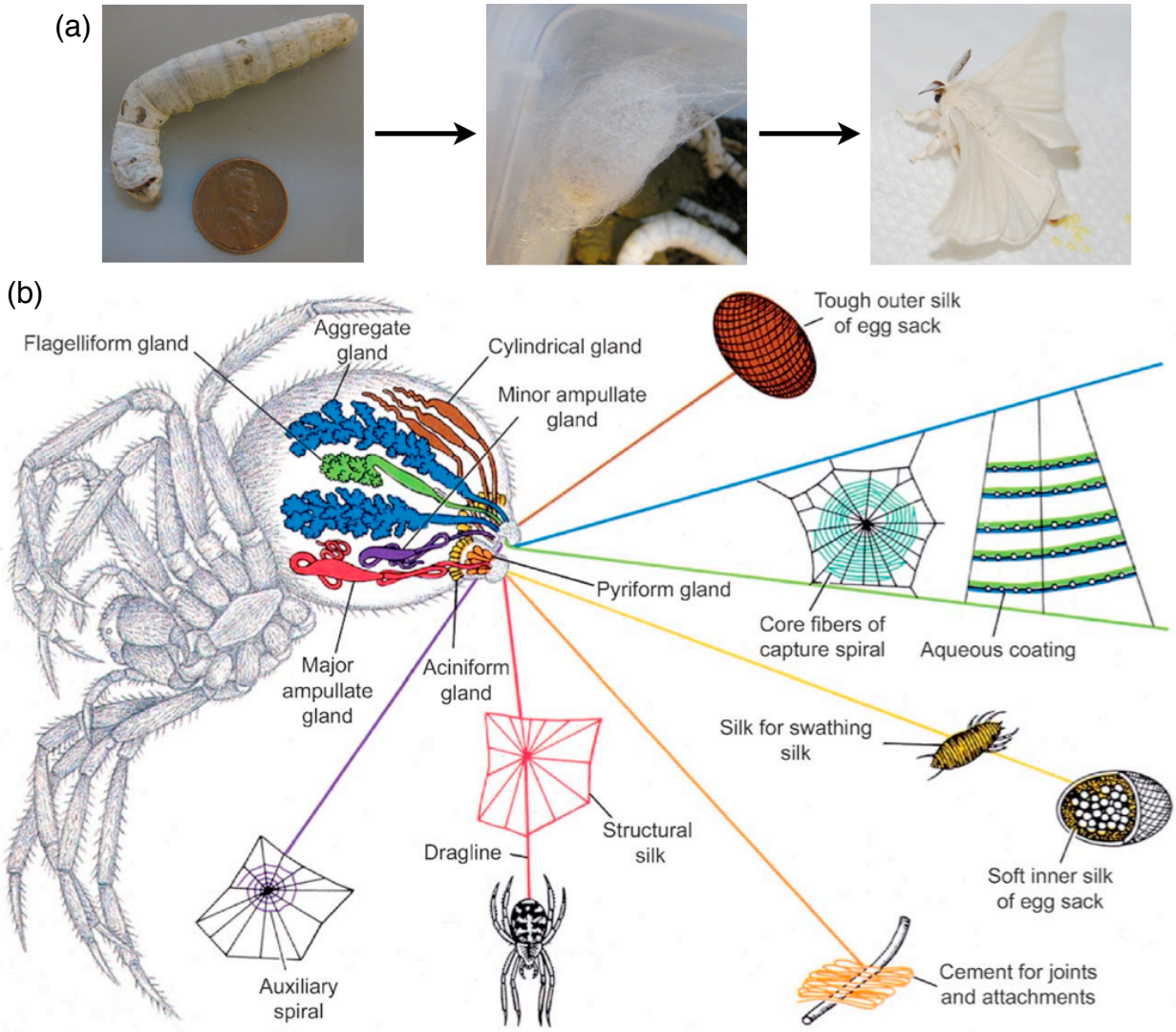

Figure 1. Uses of silk in silkworm and spiders. (a) A silkworm (*B. mori)* uses silk to build a cocoon to protect itself during metamorphosis into a moth. Moth image copyright 2009 Fastily. (b) Orb weaving spiders produce different silk fibers tailored for different uses. Reprinted from (Vollrath 2000) with permission from Elsevier.

Spider silk is often fabled for its incredible mechanical properties (e.g. Spiderman), which are substantially better than those of silkworm fibers (Figure 2). In these cases, the specific type of spider silk in reference is the dragline silk, used to support orb webs as well as a safety line. Dragline silk has a breaking strength comparable to steel (>1GPa), and an extensibility closer to nylon (>30%), giving it an extremely high toughness (energy absorbed to breakage). As such, it has been subject to significantly more investigation than the other types of silk fibers.

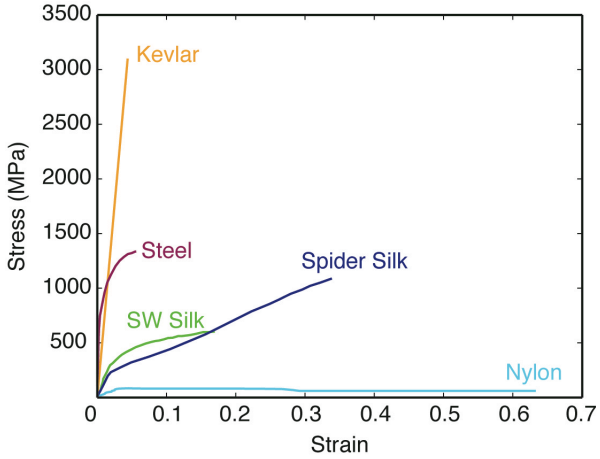

Figure 2. Stress-strain curve of various common materials in comparison with spider and silkworm (SW) silk. Spider silk has a high breaking strength combined with a high extensibility. Data from references (Ming-Liang, Nair et al. 1994; Lesuer, Syn et al. 1999; Perez-Rigueiro, Viney et al. 2000; Lawrence, Vierra et al. 2004; Weber 2010).

Whereas silkworms can easily be farmed over large areas and grown in dense environments for the collection of massive amounts of silk, spiders have completely evaded mass cultivation. Unlike silkworms, spiders are carnivorous, territorial, and produce low quantities of silk (Vollrath and Knight 2001). Therefore, despite the impressive and desirable mechanical properties of spider silk, it is unobtainable in commercially useful quantities. As a consequence, massive efforts have been put forth to generate recombinant spider silk protein for mass production, however their success has been very limited. To date, there has been a complete inability to form fibers from recombinant spider silk that duplicate the exceptional mechanical properties of naturally spun silk fibers (Vollrath 2000). Even attempts at solubilizing natural fibers and re-spinning them have proven unsuccessful. These past—and failed— attempts at forming native-quality spider silk fibers were mostly based on forcing the silk protein through a syringe, or small hole. Within the spider and silkworm, however, fiber formation is an extremely carefully and dynamically controlled process involving complex fluid dynamics, biophysics, and biochemistry (Knight and Vollrath 1999; Vollrath and Knight 2001; Dicko, Vollrath et al. 2004; Asakura, Umemura et al. 2007). In fact, silk is produced and polymerized at low temperatures and pressures, from aqueous solvents, unlike most industrial fiber spinning processes. Upon close examination, silk glands can actually be perceived as complex microfluidic systems. With the development of modern microfabrication and microfluidic technologies, it is believed that by replicating the

complexity of the *in vivo* silk gland, we will be able to spin spider silk fibers that have comparable mechanical properties to those that are naturally spun.

This dissertation focuses on the study of silk spinning both computationally and experimentally, with an emphasis on using microfabrication and microfluidic technologies for the processing of silk proteins into fibers and other structures. Within this introduction, I provide an overview of both silkworm and spider silk protein, spinning, and fibers as well as a review of the literature on the micro-scale processing of silk protein and the applications derived therefrom.

1.2 Silk Protein

Silk fibers are protein-based materials, with the core silk proteins referred to as "fibroins". *Bombyx mori* fibroin consists of three proteins that form a 2.3 MDa multimeric complex in a 6:6:1 molar ratio: the so-called "heavy chain" (~350 kDa), "light chain" (~26 kDa), and the glycoprotein P25 (~30 kDa) (Inoue, Tanaka et al. 2000). Silkworm fibroin amino acid sequences consist primarily of repeats of glycine alternating with alanine, serine, threonine, and valine (Dicko, Kenney et al. 2006).

Spider dragline fibroin from the major ampullate gland (called spidroin) consists of two proteins: MaSp1 (~250 kDa) and MaSp2 (~320 kDa) (Chinali, Vater et al. 2010). MaSp1 is the most abundant protein in the dragline fiber, with MaSp2 heterogeneously distributed throughout the fiber (Sponner, Unger et al. 2005). Both MaSp1 and MaSp2 contain polyalanine and glycine-alanine repeats, thought to form crystalline β-sheet domains. MaSp2, however, contains significantly more proline than MaSp2, which is thought to confer much of the elasticity to the fiber (Liu, Shao et al. 2008). It should be noted that the vast majority of studies on spider silk and silk production are performed on *Nephila*, *Aranaea*, and *Latrodectus* spiders because of their large size and availability. Because of the known similarities among the spiders, it is assumed that most knowledge obtained from one equally applies to the others.

The definitive structure of silk protein in its various states (solution vs. fiber) is not entirely understood. It is well established that both fibroins and spidroins undergo a water-soluble random coil/α-helix (called "silk I") to water-insoluble β-sheet (called "silk II") transition during spinning (Jin and Kaplan 2003). However, both the fiber and solution are unstable, undergoing irreversible structural transitions over time and upon exposure to stresses (Sirichaisit, Brookes et al. 2003; Holland, Terry et al. 2006). This, combined with handling difficulties and the inherent biological variability of silk fibers, has made it difficult to fully understand the structure and folding of silk proteins.

1.3 Silk in Solution Form (Silk "Dope")

Silk is stored in the silk gland in high concentrations (25-30 wt%), with water as a solvent (Vollrath and Knight 2001). It has long been known that silk fibroin exhibits unique responses to fluidic forces, such as varying liquid crystalline textures (Willcox, Gido et al. 1996; Knight and Vollrath 1999), non-Newtonian flow profiles (Yamaura,

Okumura et al. 1985; Holland, Terry et al. 2006), and flow-induced crystallization (Iizuka 1966; Iizuka 1983; Yamaura, Okumura et al. 1985; Knight, Knight et al. 2000). Silk is, in fact, a lyotropic liquid crystal and develops unique liquid crystalline textures depending on processing conditions and concentrations (Kerkam, Viney et al. 1991; Willcox, Gido et al. 1996; Asakura, Umemura et al. 2007). Generally, liquid crystalline solutions exhibit shear-thinning behavior, whereby the viscosity of the solution decreases as a function of increasing imposed shear rate, and both regenerated and native fibroin and spidroin solutions have been shown to have this characteristic (Holland, Terry et al. 2007). Despite the large difference in protein composition of spider and silkworm silks, the rheologies of the proteins in their solution state (before undergoing the phase transition into a fiber) are extremely similar (Holland, Terry et al. 2006). Because silkworms and spiders evolved independently, this is a unique example of convergent evolution, suggesting that these rheological properties are of strong significance for the ambient temperature and pressure silk spinning process.

Because fiber spinning is a largely extensional process, understanding the extensional viscosity of spinning solutions is critical. Extensional viscosity is the resistance of a fluid to tensile stretching, and can be a function of strain rate and accumulated strain in non-Newtonian fluids. Unfortunately, extensional rheometers are not nearly as prevalent as shear rheometers, and complete constitutive models of non-Newtonian fluids can be extremely complex. So far, the work of Kojic et al. has been the only one to study the extensional rheology of silk, looking at extracted *N. clavipes* dope (Kojic, Bico et al. 2006). Their results showed a combination of high extensional viscosity and strain-hardening at large strain rates. The latter result was also due to solidification of the filament, because of diffusion of water out of the silk during stretching. It is likely that the high strain-rate extensional behavior of silk will be of critical importance to fully understanding the spinning process in the future.

Despite the rheological similarities of spider and silkworm dope, it is stored differently depending on the organism. Spiders easily build a new web every day and must always have liquid silk ready to spin. Silkworms, on the other hand, store their dope until they are ready to spin their entire cocoon. Silk solution is highly unstable, and to prevent it from crystallizing over this long storage period, silkworms maintain their dope in a gel state before converting it to a solution state before spinning. The gel state is primarily maintained through high calcium concentrations, and is broken down to a spinnable liquid state through calcium removal and the addition of potassium ions (Zhou, Chen et al. 2005). In the days before cocoons spinning, silkworms gradually convert their gel dope to a solution state (Holland 2010). This can make native silkworm dope difficult to study, as it is hard to consistently extract dope in the same state from worm to worm.

1.4 *In Vivo* Silk Spinning

Many of the processes by which silk protein is secreted, processed, and crystallized into fiber form are known, however the reasons why they actually work in creating such phenomenal fibers are still unclear. The spider and the silkworm silk glands operate

extremely similarly, with slight changes in chemistry along the length of the gland and the additional secretion of a thick sericin coating around the protein and fiber in the silkworm.

An *Araneus diadematus* major ampullate gland is shown in Figure 3a and a schematic of the system is depicted in Figure 3b with the critical mechanistic components labeled. Silkworm glands look very similar, but are much larger. Initially, high concentrations of silk protein are secreted within the gland, from the wall epithelial cells, into an aqueous bath (i, in figure). The protein droplets slowly move down the length of the gland and coalesce at the entry of what is referred to as the "S-shaped duct" (ii). This duct acts as an extremely long funnel, extending and orienting the protein molecules along the fiber axis through a gradual taper in diameter from approximately 200 µm to 10 µm. Simultaneously, the epithelial cells lining the wall of the duct actively transport various ions (e.g. H^+, K^+) into and out of the silk solution (iii). These ions help regulate the crystallization and solidification of the protein by either stabilizing its unfolded form or inducing folding into a β-sheet structure. Table 1 details the ionic changes along the length of spider and silkworm silk gland, and their effect (if known) on the dope. Near the end of the duct, the forming silk fiber detaches from the gland wall, and water diffuses out of the protein, concentrating the protein solution (iv). Through the combination of ionically- and shear-regulated structural changes and solvent removal, the liquid dope increases in viscosity and spinnability. A muscle around the gland grips the fiber and is believed to induce additional tension in the fiber, increasing molecular alignment and mechanical properties-- referred to as a double-draw in industrial spinning (v) Lastly, excess water is then reabsorbed by the organism (vi).

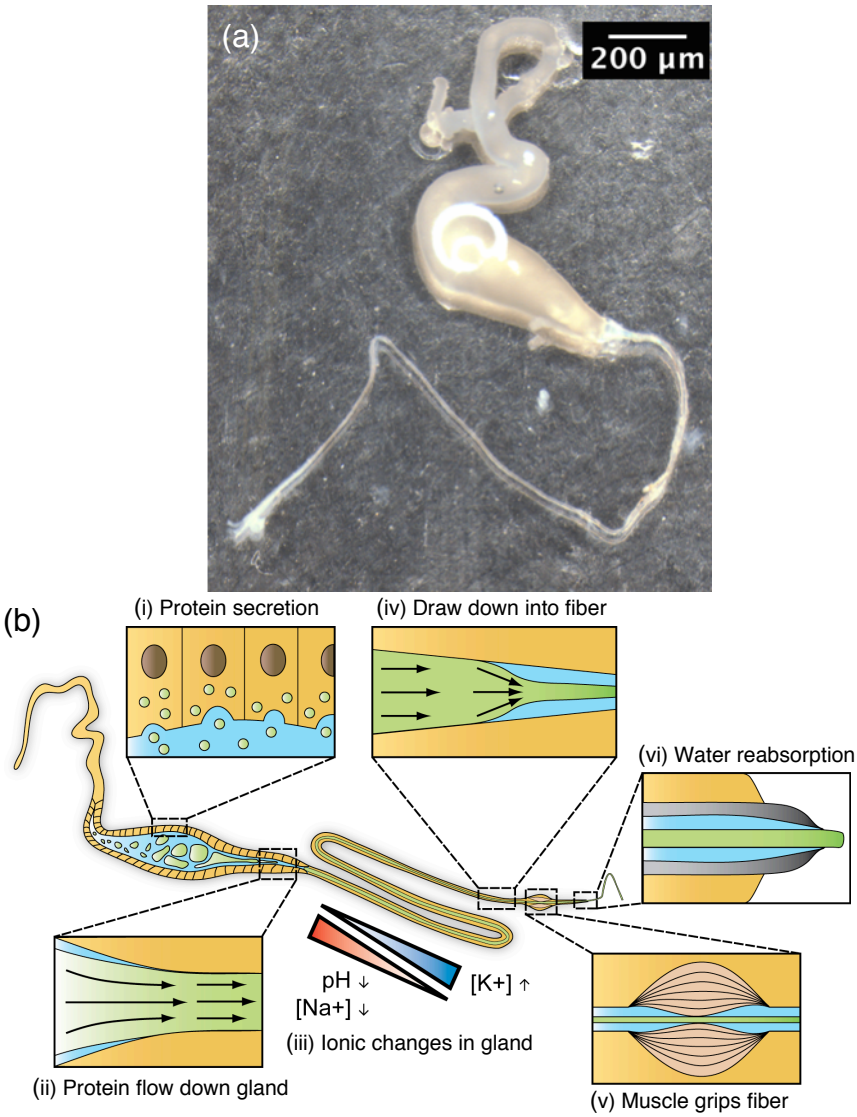

Figure 3. Mechanism of fiber formation in the spider major ampullate gland. (a) An excised *A. diadematus* major ampullate gland. (b) Schematic process of silk secretion and fiber formation, from left to right. Silk protein is represented in green, and the gland cells/wall in orange. Flow is from left to right. Adapted from Michael Ellison, Clemson University.

Because of their different uses of silk, spiders and silkworms draw their fibers in very different manners. Silkworms spin and deposit their silk by moving their heads (and thus spinnerets) in a “figure eight” pattern, creating layer upon layer of silk fibers and eventually forming a cocoon (Shao and Vollrath 2002). Because dragline silk is the structural basis for the web and the spider safety line, it is spun under the weight of the spider falling (Gosline, Guerette et al. 1999). It has been classically accepted that both organisms spin their silks at a rate of ~1 cm/s, and this rate is often used during artificial reeling of silk from spiders or silkworms. However, recent measurements have revealed that physiological dragline spinning speeds actually range from 0.05 to 1.30 m/s (Ortlepp and Gosline 2004). Evidence suggests that spiders, and perhaps silkworms,

actively control the tension in the fiber during the spinning process, contributing to the large variability in mechanical properties of fibers taken directly from webs (Boutry and Blackledge 2009). Because artificially reeled silk is spun at a constant rate, the resultant fibers have consistent mechanical properties (Vollrath, Madsen et al. 2001). However, artificial reeling can significantly alter the protein structure and mechanical properties of a silk fiber from what is actually produced in nature (sometimes even improving fiber properties) (Shao and Vollrath 2002).

Table 1. Ionic concentration changes along the length of the silk gland in the spider and silkworm, and how these changes affect the silk dope.

ion	Silkworm	Spider
pH	↓ 6.9 to 4.8, induce *β*-sheet formation	↓ 6.9 to 6.3, induce *β*-sheet formation
K^+	↑ break down gel state	↑ induce *β*-sheet formation
Na^+	↑ weaken gel state	↓ induce *β*-sheet formation
Ca^{2+}	↓ calcium maintains the gel state	unknown
Cu^{2+}	↑ induce *β*-sheet formation	unknown
Mg^{2+}	↑ induce *β*-sheet formation	unknown
Zn^{2+}	↑ induce *β*-sheet formation	unknown

1.5 Silk Fibers

Silk is generally spun as a pair of fibers. Silkworms spin composites of two silk fibers out of a single spinneret, surrounded by and adhered together with a sericin protein coating (Hardy, Roemer et al. 2008) (Figure 4a). The individual silkworm silk fibers are 10-12 µm in diameter with a triangular cross-section. In spiders, each spinneret produces a single fiber from a single gland, but two fibers are wound around each other (Figure 4b). A dragline silk fiber ranges from 2-5 µm depending on the type and size of the spider, with a circular cross-section (Hardy, Roemer et al. 2008). It is not known why spider and silkworm silks differ in cross-sectional shape.

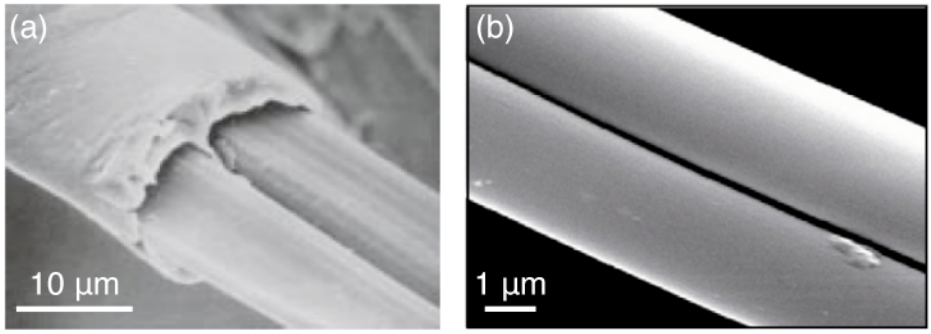

Figure 4. Silk from silkworms and spiders. (a) *B. mori* silk, which is a composite of two individual filaments coated in sericin. Reprinted from (Shao and Vollrath 2002) by permission from Macmillan Publishers Ltd: Nature, copyright 2002. (b) Major ampulate silk threads from an *A. diadematus* spider. Reprinted from (Hardy, Roemer et al. 2008) with permission from Elsevier.

In addition to serving as a glue, silkworm sericin is believed to retain water in the fiber. Dragline silk has also been recently shown to have a coating layer-- a glycoprotein coat further surrounded by a lipid coating (Sponner, Vater et al. 2007). Like sericin, it is likely that these coatings help retain water in spider silk fibers, and water content has been shown to be very important for fiber mechanical properties (Liu, Shao et al. 2005; Liu, Shao et al. 2008; Agnarsson, Boutry et al. 2009). Dragline fibers additionally have the unique hydration response of super contraction. After spinning, upon rehydration, they contract up to 50% of their length (Agnarsson, Boutry et al. 2009). It is unclear what purpose this feature has, but it has been thought to be a means of tightening the web when it undergoes sagging from water droplets. However, the poor creep response of supercontracted silk makes this a questionable hypothesis (Bell, McEwen et al. 2002).

The fibers themselves are semi-crystalline, with the silk II β-sheets forming the crystalline fraction, and silk I helical and amorphous chains linking the crystals together (Gosline, Guerette et al. 1999) (Figure 5). The crystalline domains confer strength upon the fiber, and the amorphous domains confer elasticity. The crystals have a length-to-width aspect ratio of five, and the alignment of their long axis along length of the fiber is thought to be important for its tensile strength. Silk dope is initially secreted in an isotropic state, and these crystals form and become aligned within the silk gland during the spinning process.

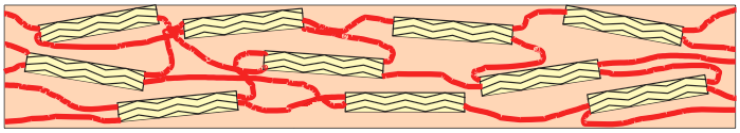

Figure 5. Proposed molecular structure of a silk fiber. The fiber is composed of β-sheet crystals connected by amorphous linkers. Used with permission from (Gosline, Guerette et al. 1999).

1.6 Sources of Silk Protein used in Experiments

Throughout the literature, different sources of silk protein are used as a basis for studying the protein structure, function, and rheology. It has only recently become appreciated that these varied sources and preparation methods of silk are substantially different and not necessarily representative of native silk protein (Yamada, Nakao et al. 2001; Holland, Terry et al. 2007). It is thus important to consider the type of silk protein used in each study. There are three main sources:

a. Silk Glands

Per organism, spiders and silkworms produce relatively low quantities of silk protein that can be excised for use. However, this silk is the only one known to produce native quality fibers. A *N. clavipes* spider contains 1-2 µL of silk protein per major ampullate gland, whereas a large silkworm can contain about 100 µL of silk protein per gland. Difficulties remain, however, in how much of this protein is actually usable, as its concentration and structure varies throughout the length of the gland. In addition, in the silkworm, the protein is coated with a sericin glue that needs to be washed off, potentially contaminating and diluting the silk protein. An attempt was made to culture silkworm glands for continuous production of silk protein, but yields were low and the organ only survived a few days in culture (Asakura, Sakaguchi et al. 1993).

b. Silkworm Cocoons

Silkworm cocoons are easily obtainable at low cost, and dissolving the cocoon fibers can provide an abundance of silk protein. Throughout the literature, dissolved cocoon silk is referred to as reconstituted silk fibroin (RSF). Dissolution processes differ slightly, but basically consist of removing the sericin from the cocoon in hot/boiling water (degumming), and subsequently dissolving the silk fiber in a saturated chaotropic solution. To date, all attempts to spin native quality fibers from dissolved cocoon silk have proven unsuccessful, and its use has largely been relegated to the study of silk protein structure and the creation of medical devices (Altman, Diaz et al. 2003).

Recently, it has been shown that the dissolution process significantly degrades the silk protein (Yamada, Nakao et al. 2001; Holland, Terry et al. 2007), and that even highly concentrated reconstituted silk dope exhibits vastly different rheology than native silk dope. A protocol has now been published that describes how to dissolve cocoons without degrading the silk protein (Yamada, Nakao et al. 2001). However, the concentration yields (0.1% w/v) are prohibitively low for making a native concentration solution. Thus it is highly unlikely that RSF will be useful as a source material for native quality fiber spinning, and because of protein degradation, must be considered cautiously when used a model system for studying structural changes of silk protein.

A common procedure to create a more spinnable solution is to dehydrate a film of RSF and redissolve it in hexafluoroisopropanol (HFIP). HFIP-RSF is highly viscous and can be wet spun into decent (but not native) quality fibers (Zhao, Yao et al. 2003). This

spinnability is likely because HFIP causes RSF to fold into an *α*-helical state upon dissolution (Trabbic and Yager 1998). HFIP, however, is an extremely hazardous organic solvent and preferably avoided.

c. Recombinant Proteins

There have been many attempts to create recombinant systems (bacteria, yeast, etc.) that express spider silk proteins. Their yields are always extremely low, which is specifically problematic for obtaining the concentrations needed for native-like spinning (Kluge, Rabotyagova et al. 2008). Furthermore, high purity has been difficult to obtain (Lazaris, Arcidiacono et al. 2002). Lastly, and perhaps most critically, all recombinant silk proteins to date have actually been truncated silk-like fragments or attempts to stitch together consensus repeat units of the protein sequence (Kluge, Rabotyagova et al. 2008). None of these proteins has been able to produce a native quality fiber, and most are being explored for their utility in medical devices (Hardy, Roemer et al. 2008).

It was not until 2007 that a full length silk sequence was published (Ayoub, Garb et al. 2007), and it is now believed that the complexity of the full protein (highly conserved N- and C-termini, varying block repeat sizes) is critical for spidroin solubility, processing, and fiber mechanical properties (Ayoub, Garb et al. 2007; Kluge, Rabotyagova et al. 2008).

1.7 Spinning Artificial Silk Fibers

a. Conventional Fiber Spinning

Conventional spinning methods have been applied to silk proteins, with the most common being wet spinning and electrospinning. In electrospinning, polymer solution is extruded through a metal orifice into a strong electric field (~30 kV/cm), which charges the polymer and pulls it on to a collector plate (Chew, Wen et al. 2006). Electrospinning readily produces non-woven mats; however reeling a single fiber is difficult using this process. Therefore, all electrospun silk has been limited to tissue engineering and drug delivery applications.

In wet spinning, a dissolved polymer dope is extruded through a spinneret into a non-solvent bath and at least one drawing step is performed in the spin process to increase polymer molecule alignment along the fiber axis and improve mechanical properties (Trabbic and Yager 1998). Methanol is the most commonly used non-solvent when spinning silk proteins because it causes extremely rapid precipitation of the protein and conversion to a *β*-sheet folded structure (Um, Kweon et al. 2004). However, this process almost always results in brittle fibers.

Whether it was due to the lack of native-quality dope, the spinning method, or most likely the combination thereof, standard spinning methods have never successfully duplicated the natural spinning conditions or the material properties of natural silk fibers.

b. Microfabricated Wet Spinning

Whereas spinning processes can be considered “microscale” because spinneret outlets often have diameters on the order of 10 to 100 µm, the equipment usually requires large volumes of material which are not readily available when dealing with silk. To address this problem, Liivak et al. developed a microfabricated wet spinning apparatus capable of spinning as little as 10 mg of protein (Liivak, Blye et al. 1998) (Figure 6). The device consisted of a silicon wafer etched to have a 80, 100, 120, 140, or 160 µm square outlet. The system proved advantageous for rapidly testing a large range of fiber spinning conditions, using minimal amounts of protein, but never produced native-quality fibers. As with every attempt to spin fibers from silk proteins, it is important to note the source material used. The authors made fibers from HFIP-RSF (2.5 wt.-%), as well as artificially reeled *N. clavipes* dragline silk dissolved in HFIP (1 wt.-%), wet spun into methanol. As mentioned, HFIP maintains silk in a coiled state and creates the most spinnable solution, but potentially degrades the fibroin.

As the scientific supply industry has progressed, it is unclear if such a simple microfabricated device retains its value. Glass capillaries with nano- to micro-size orifices can now easily be purchased, and have been used to extrude silk fibers (Ghosh, Parker et al. 2008). Micron-scale bore tubing is also available for purchase, with a variety of syringe attachments. The latter has also been used to successfully spin small quantities of silk proteins and is now common for lab-scale wet spinning experiments (Teule, Cooper et al. 2009).

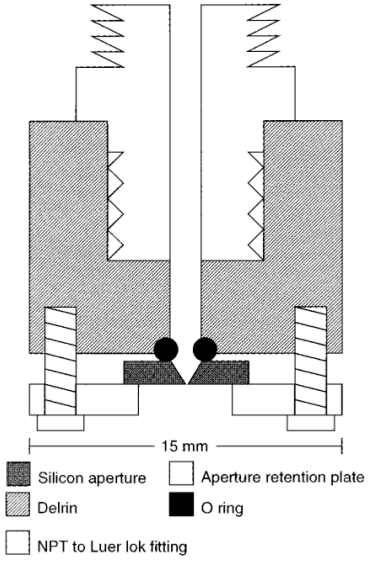

Figure 6. A microfabricated wet spinning system used to spin small quantities of silk protein. Reprinted from (Liivak, Blye et al. 1998). Copyright 1998 American Chemical Society.

c. Microfluidic Laminar Flow Systems

Upon shrinking to the microscale, the dominant forces of physical phenomena change. Microfluidic flow is generally laminar as opposed to turbulent, meaning that viscous forces dominate over inertial forces. Laminar flow allows precise calculation of mass transport as a function of time and the convective flow profile for laminar flow is straightforward to calculate from parameters such as channel geometry, pressure drop, and fluid properties. Due to translation invariance, fluid streamlines remain constant over time, and mixing of laminar flow streams occurs primarily by diffusion (Figure 7).

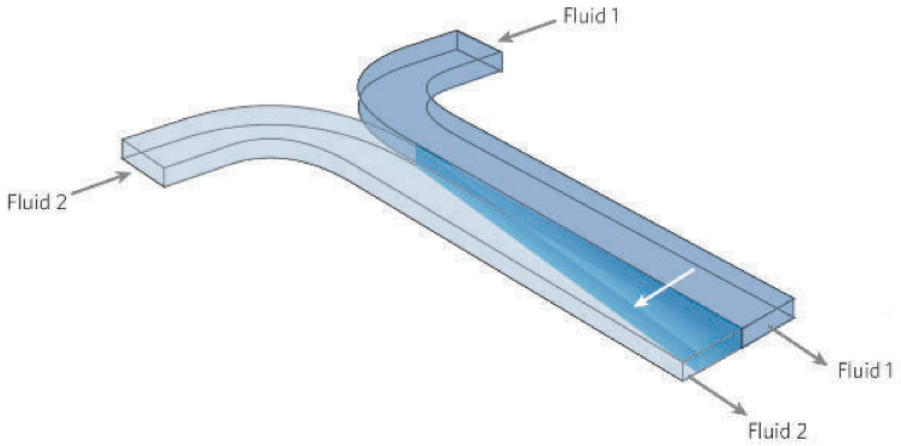

Figure 7. Laminar flow in a microfluidic channel. Fluid 1 and fluid 2 flow adjacently in the channel, and mix only due to the lateral diffusion of molecular species over time. Reprinted from (Atencia and Beebe 2005) by permission from Macmillan Publishers Ltd: Nature, copyright 2004.

Leveraging these physical phenomena and the ability to microfabricate complex flow channels, several researchers have used microfluidic laminar flow streams to create fibers from various materials-- controlling mass transport into and out of a centrally confined laminar flow stream with a coagulating sheath flow (Shin, Park et al. 2007; Hwang, Khademhosseini et al. 2008). These systems have more recently been applied to silk proteins, and because diffusion of ions from the sheath flow occurs slowly over the length of the of the flow, they have received attention as a more “biomimetic” methodology for spinning silk fibers. A particularly advantageous feature is that if built from the proper materials, laminar flow systems present unique opportunities for performing molecular spectroscopy as a function of flow time and diffusive mixing (Martel, Burghammer et al. 2008). Lastly, the ability to use microfabrication technologies to create channels with specific geometries (e.g. contractions and expansions), enables further exploration of microscale flow profiles on silk protein assembly and fiber spinning.

Martel et al. initially microfabricated a T-junction geometry to study silk protein folding and aggregation as a function of the diffusion time with X-ray diffraction (Martel

2008) (Figure 8). Their sheath flow was a pH 2 buffer co-flowing with 0.5% w/v non-degraded RSF. The system proved largely unusable as it suffered from clogging due to the rapid aggregation of silk fibroin. Microfabrication technologies readily create low aspect ratio, rectangular cross section ("2D") geometries. Therefore, the fibroin was in contact with the top and bottom channel walls during flow, and adhered and built up in the channel, clogging the device.

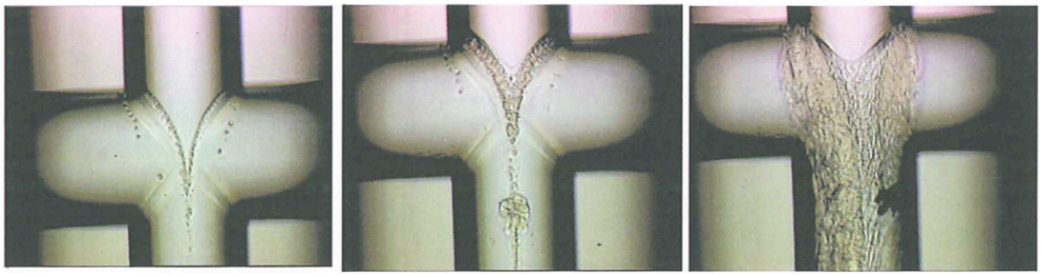

Figure 8. Microfluidic channel used to study the aggregation of silk fibroin. Flow is from top to bottom, channel width is 100 μm. The center stream is fibroin, and the side sheath streams are pH 2 buffer. Over time (left to right) the fibroin aggregates, sticks to the channel walls, and clogs the device. Reprinted from (Martel 2008) by permission from Dr. Anne Martel.

To minimize the clogging problem, the researchers shifted to a laminar flow platform built from concentric glass capillaries, thus eliminating any contact that the fibroin has with the walls of the channels (Martel, Burghammer et al. 2008; Martel, Burghammer et al. 2008) (Figure 9). Whereas this system does not benefit from the complex geometries capable of being built through microfabrication, it is cheap and simple to assemble, and its nearly axisymmetric flow focusing is more akin to the silk gland than a "2D" rectangular cross-section channel. This system was capable of creating fibers, but they were too brittle to mechanically test. It proved most beneficial for use with X-ray diffraction to study silk assembly and aggregation as a function of diffusive mixing. We discuss our use of a similar system in Chapter 3.

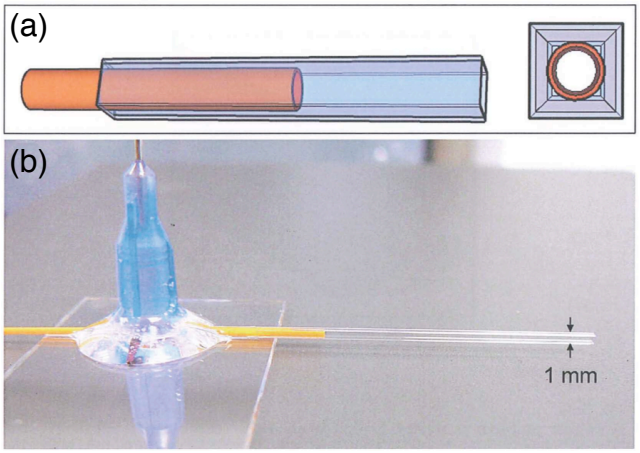

Figure 9. Capillary tubing device used for laminar flow focusing and to avoid fibroin contact with channel walls. (a) Schematic of the device, where a circular capillary is

inserted into a square capillary to ensure centered flow. (b) Picture of the assembled system. Reprinted from (Martel 2008) by permission from Dr. Anne Martel.

Rammensee et al. leveraged the ability to microfabricate various microfluidic geometries to test the effect of flow types on silk assembly (Rammensee, Slotta et al. 2008). The authors studied the assembly of their recombinant silk-mimetic protein at a concentration of 2% w/v. Initially, they used laminar flow streams to control the pH and diffusion of PO_4^{3-} into the silk stream and found that certain pH and salt conditions caused their protein to assembly into microspheres. They furthermore added a contraction geometry to induce an elongational flow on their protein, as found in the silk gland. With the addition of elongation flow, the microspheres were stretched in short (1 mm) fibers (Figure 10). Because of their use of recombinant silk mimetic proteins, rather than native silk, it is unclear how relevant these studies are to native silk fiber assembly, but they presented an interesting demonstration of the utility of microfluidics in studying the effects of flow on silk.

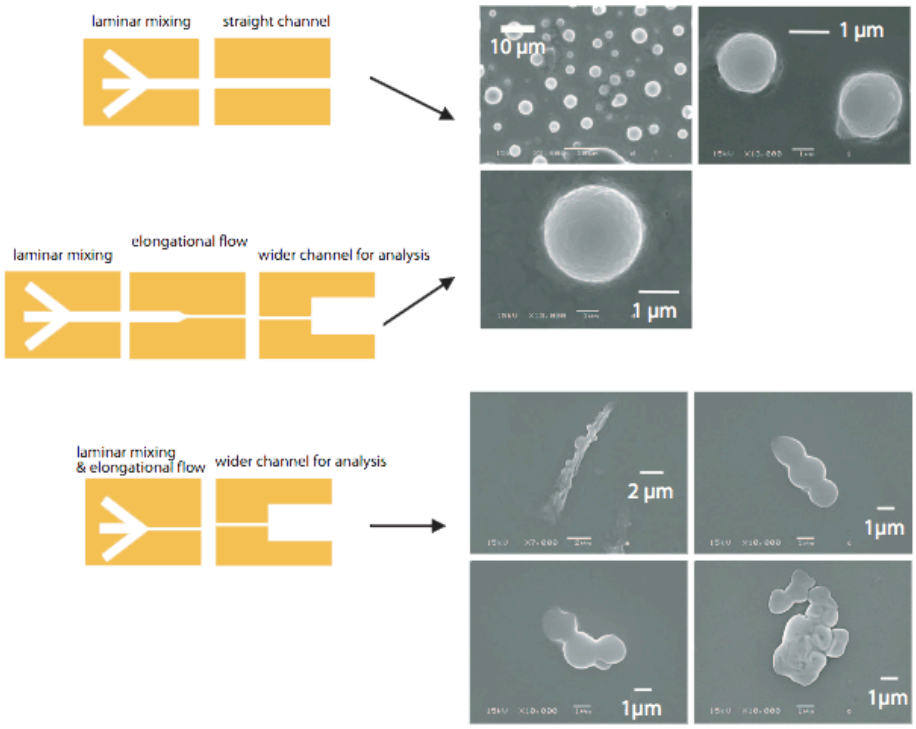

Figure 10. Microfluidic channels designed for the study of the assembly of a recombinant silk-like protein, and the resultant materials from the channels. Reproduced from (Rammensee, Slotta et al. 2008). Copyright 2008 National Academies of Sciences.

d. Future Potential

Whereas the use of microfabrication and microfluidics has proven useful in the study of silk assembly, it has yet to truly replicate the conditions by which silk is spun *in vivo*. Specifically problematic is the fact that microfabrication techniques readily create planar

channels, whereas the silk gland has a circular cross section. The challenge is even more difficult than this: a biomimetic channel must be axisymmetric, have a defined contraction geometry, and have the ability to transport ions into the channel, and water out of it. In Chapter 4, I discuss my advances toward this goal.

1.8 Other Microscale Uses of Silk

Because silkworm cocoons are available in such abundance, and can be dissolved into RSF fairly readily, several non-fiber based uses of RSF have emerged. Most notably, silkworm silk is non-immunogenic and biodegradeable, and has received an exceptional amount of investigation as a scaffold for tissue engineering and drug delivery (Altman, Diaz et al. 2003). These scaffolds have generally been hydrogels, films, sponges, and electrospun mats. The recent ability to create microfabricated structures with silk is now opening new and unique avenues for silk materials. Below, I overview several of these achievements, and in Chapters 5 and 6, I discuss my own work on creating alternative silk microstructures.

a. Micropatterning and Microfluidics

Micropatterned structures and microfluidic devices are most commonly built using soft lithography, whereby polydimethylsiloxane (PDMS) elastomer is molded over photoresist-defined features that are patterned onto a silicon wafer. If an enclosed microfluidic channel is desired, the molded PDMS is bonded to glass. PDMS provides a simple and rapid means of replicating microstructures, however, there is significant interest in creating implantable and biodegrable microfluidic systems for advanced medical devices. Consequently, RSF has been explored as a polymer to fill this niche.

Gupta et al. initially demonstrated that RSF dissolved in an ionic liquid could be molded on a micropatterned substrate to replicate its features (Gupta, Khokhar et al. 2007). The procedure involved mixing RSF with an ionic liquid, casting this solution onto a micropatterned surface, and then solidifying the silk in a methanol bath. Their goal was to mold unique microtopographies on a silk film for regulating cell growth. Bettinger et al. demonstrated that this procedure could be greatly simplified by allowing RSF (with no ionic liquid) to dry on top of a micropatterned substrate (Bettinger, Cyr et al. 2007). The resultant film was in a silk I conformation and thus water-soluble, but could subsequently be exposed to methanol to induce a silk II transition and become irreversibly solidified. The authors further demonstrated that these silk structures could then be molded onto flat silk films to make complete microfluidic devices (Figure 11).

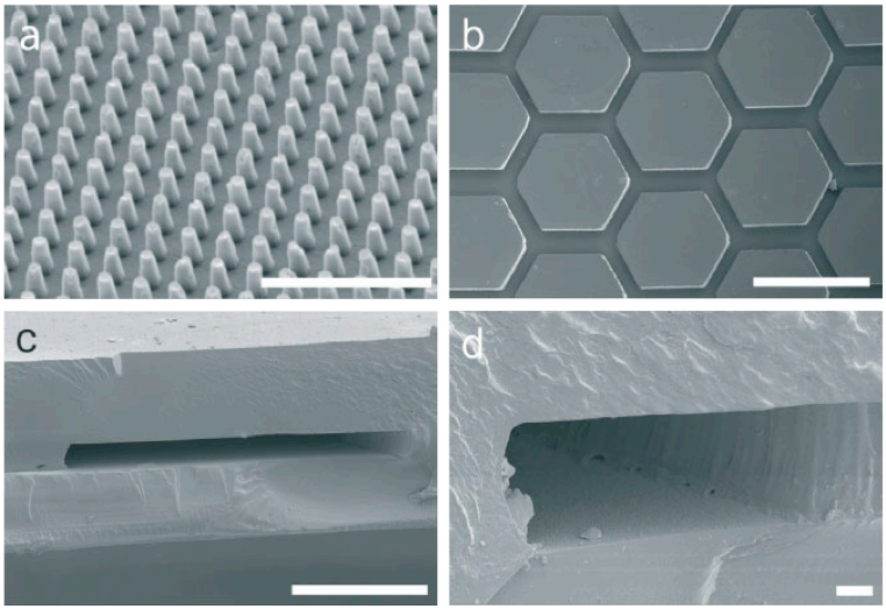

Figure 11. Silk fibroin (a) nano-patterns (scale bar is 5 μm) and (b) micropatterns (scale bar is 500 μm). (c) and (d) Enclosed silk fibroin microfluidic channels. Scale bars are 200 μm and 10 μm, respectively. Copyright Wiley-VCH Verlag GmbH & Co. KGaA. Reproduced with permission from (Bettinger, Cyr et al. 2007).

Gupta et al. later demonstrated a novel approach for micropatterning the protein structure of silk films (Gupta, Singamaneni et al. 2010). This enables the creation micropatterns with spatially varying silk I/silk II conformations (and thus mechanical properties), or even through dissolution of the water-soluble silk I features, stand-alone silk II microstructures. The strategy involves creating a negative mask out of micromolded polystyrene (PS) on top of a silk film (Figure 12). Subsequent exposure of the masked silk film to methanol vapors caused the unmasked area to undergo conversion from a silk I to silk II structure. This technique could greatly expand the utility of silk films, particularly due to the ability to selectively dissolve away silk I features.

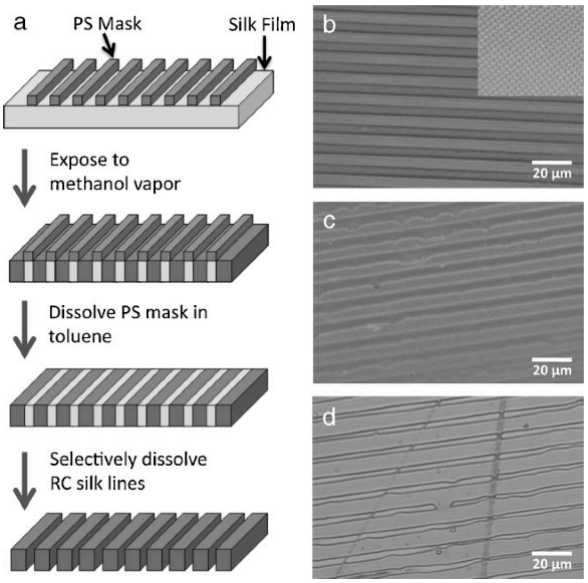

Figure 12. Micropatterning silk fibroin chain conformation. (a) Step-by-step patterning procedure, whereby a silk film is covered with a PS mask, exposed to methanol vapor, and subsequently the PS mask is removed. (b-c) Resultant silk micropatterns from each step. Copyright Wiley-VCH Verlag GmbH & Co. KGaA. Reproduced with permission from (Gupta, Singamaneni et al. 2010).

b. Optics and Biosensing

Omenetto and Kaplan discovered that RSF films are optically transparent in 92% of the visible spectrum, and have leveraged this fact to create a wide range of new silk-based biodegradable optical devices and biosensors (Omenetto and Kaplan 2008) (Figure 13). They have used micropatterned, optically transparent silk films as substrates for cornea tissue engineering (Lawrence, Marchant et al. 2009), but also by casting RSF on nanopatterned substates (Omenetto and Kaplan 2008) or embossing silk films using a nano-patterned master (Amsden, Domachuk et al. 2010), they have created silk films that exhibit a wide array of diffractive properties. They have additionally extruded silk filaments from a glass capillary and used them as optical fibers (they did not make mechanical property measurements) (Parker, Domachuk et al. 2009). Because the RSF molding process occurs under benign conditions, one can incorporate a variety of molecular components into the silk and retain their functionality after patterning. They demonstrated that phenol red could be incorporated within a silk diffraction grating, and upon exposure to acid or base, the film would change color as visible by eye (Lawrence, Cronin-Golomb et al. 2008). They further demonstrated the ability to incorporate horseradish peroxidase and also hemoglobin in silk diffraction gratings, and use the spectral changes for biosensing. These systems provide a new class of mechanically tough and biocompatible sensors that could have particular utility in environmental sensing where biodegradability is important.

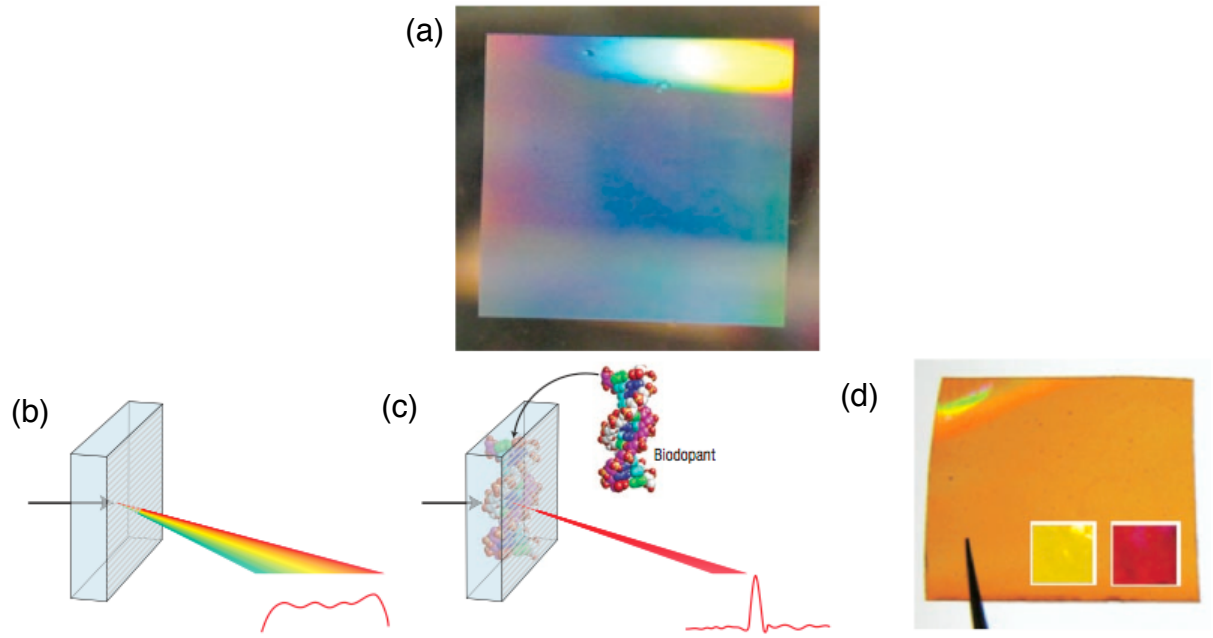

Figure 13. Silk fibroin optical elements. (a) A 600-groove-per-millimeter silk diffraction grating film. (b, c) Use of these silk diffraction gratings as optically-based sensors. The inclusion of a biodopant in the fibroin solution can vary the spectral response of the film. (d) A silk film doped with phenol red changes color when exposed to acid (left) or base (right). Reprinted from (Omenetto and Kaplan 2008) by permission from Macmillan Publishers Ltd: Nature Photonics, copyright 2008.

c. Microspheres

Polymeric microspheres have become strong candidates for use in drug delivery because of their ease of delivery and the ability to regulate their drug release kinetics. Silk microspheres have been demonstrated to have particularly beneficial characteristics for drug delivery and controlled release because of their mechanical stability, mild processing conditions, high drug encapsulation efficiency, long term sustained release, and slow degradability (Wang, Wenk et al. 2007; Wang, Wenk et al. 2007; Wenk, Wandrey et al. 2008). Methods used to produce RSF spheres have consisted of emulsification (Xie, Wu et al. 2008), spray drying (Yeo, Lee et al. 2003; Zhou, Peng et al. 2008), laminar jet breakup (Wenk, Wandrey et al. 2008), lipid templating (Wang, Wenk et al. 2007), and self-assembly (Cao, Chen et al. 2007). In addition, recombinant spider silk-mimetic peptides have been used to create microspheres (Lammel, Schwab et al. 2008) and microcapsules (Hermanson, Huemmerich et al. 2007). All of these techniques are effective at producing nano- to micro-scale silk particles, and in Chapter 5, I present a microfluidic method of generating monodisperse RSF microspheres, because uniform particle size has been shown to be advantageous for bioavailability and controlling drug release kinetics (Wang, Ma et al. 2005; Xu, Hashimoto et al. 2009).

1.9 Scope of the Dissertation

This dissertation describes the majority of my work with silk as a graduate student in the UC Berkeley/UCSF Bioengineering Graduate Group. In Chapter 2, I discuss the computational simulation of silk flow in models of both the spider and silkworm glands, as well as the biological relevance of these results. In Chapter 3, I present the use of micro-scale and laminar flow as a means of spinning silk fibers. In Chapter 4, I present my results in developing a biomimetic microfluidic silk gland that combines the geometric constraints of the native gland with the ability to regulate mass transport into and out of the silk during flow. The subsequent chapters switch focus to the processing of silk into materials other than fibers. In Chapter 5, I present a microfluidic system for the generation of monodisperse RSF microspheres. In Chapter 6, I discuss the use of RSF for high fidelity and high aspect ratio nano- and micro-molding. In Chapter 7, I discuss conclusions of my work and leave the reader with several remaining challenges in the silk field. Lastly, in the appendices, I provide detailed protocols I have developed for the very difficult processes of silkworm cocoon dissolution, raising and dissecting silkworms, and the building of a fiber testing apparatus. I hope these protocols will enable others to delve rapidly into the silk field.

Chapter 2. Simulation of Flow in the Silk Gland

2.1 Abstract

Spiders and silkworms employ the complex flow of highly concentrated silk solution as part of silk fiber spinning. To understand the role of fluidic forces in this process, the flow of silk solution in the spider major ampullate and silkworm silk glands was investigated using numerical simulation. Our simulations demonstrate significant differences between flow in the spider and silkworm silk glands. In particular, shear flow effects are shown to be much greater in the spider than the silkworm, the silkworm gland exhibits a much different flow extension profile than the spider gland, and the residence time within the spider gland is eight times greater than in the silkworm gland. Lastly, simulations on the effect of spinning speed on the flow of silk solution suggest that a critical extension rate is the initiating factor for fiber formation from silk solution. These results provide new insight into silk spinning processes and will guide the future development of novel fiber spinning technologies.

2.2 Introduction

Spiders and silkworms are able to produce silk fibers with minimal energy expense that outperform most other fibers in mechanical testing (Vollrath and Knight 2001). In order to understand how these exceptional fibers are produced so easily, the spinning mechanisms of silk glands have been under intense investigation (Vollrath and Knight 2001; Dicko, Kenney et al. 2006; Asakura, Umemura et al. 2007; Kluge, Rabotyagova et al. 2008). Despite fundamental differences in the composition and structure of spider major ampullate (MA) and silkworm fibroin proteins (Kaplan, Adams et al. 1994), the silk glands of both organisms have been shown to function similarly, by establishing an extremely complex regulatory environment for the conversion of the silk protein solution ("dope") into a solid fiber (Vollrath and Knight 2001). Simplistically, in both the spider MA gland and the silkworm, highly concentrated silk fibroin flows through the contracting geometry of the silk gland and is exposed to ionic gradients that regulate its crystallized state by inducing protein conformational changes and aggregation (Vollrath and Knight 2001; Asakura, Umemura et al. 2007). The silk dope eventually reaches a point of sufficient solidification that it detaches from the walls of the gland and is drawn out as a fiber. Whereas the molecular chemistry and structure of silk proteins and the effects of various ions on the folded state of silk fibroin have been thoroughly investigated (Kaplan, Adams et al. 1994; Knight and Vollrath 2001; Foo, Bini et al. 2006), the effects of flow on silk fiber formation have received relatively little attention.

It has long been known that silk fibroin exhibits unique responses to fluidic forces. These responses include varying liquid crystalline textures (Willcox, Gido et al. 1996; Knight and Vollrath 1999), non-Newtonian flow profiles (Yamaura, Okumura et al. 1985; Holland, Terry et al. 2006), and flow-induced crystallization (Iizuka 1966; Iizuka 1983; Yamaura, Okumura et al. 1985; Knight, Knight et al. 2000). In particular, both dilute and concentrated silk fibroin have been shown to exhibit shear-thinning behavior (Chen, Knight et al. 2002; Holland, Terry et al. 2006; Kojic, Bico et al. 2006), whereby the

viscosity of the solution decreases as a function of increasing imposed shear rate. Essentially, the shear field stretches the long, deformable molecules and distorts the molecular orientations and conformations; the viscosity decreases as increasingly higher shear rates result in increasingly disturbed distributions of conformations and orientations (Larson 1999). Furthermore, silk fibroin exhibits flow-induced crystallization (Iizuka 1966; Iizuka 1983; Yamaura, Okumura et al. 1985; Knight, Knight et al. 2000), during which the stretching of polymer molecules in flow creates a favorable state for crystal formation. It has been shown that silk fibroin begins crystallizing after exposure to a critical shear rate (Iizuka 1966; Holland, Terry et al. 2006). To this end, shear rate profiles along the silkworm gland have been mapped to determine how flow in the gland induces fiber formation (Iizuka 1966; Moriya, Ohgo et al. 2008).

The silk gland in the silkworm and the spider MA gland are both decreasing diameter funnels, whose shapes fit well to a two-stage exponential function (Knight and Vollrath 1999; Asakura, Umemura et al. 2007). It has been noted that similar hyperbolically shaped funnels are used in industry in order to spin commercial fibers (Vollrath and Knight 2001) and it has been proposed that this shape could cause a slow elongation of the silk fibroin molecules, stretching and aligning them along the final fiber axis, as well as inducing crystallization (Knight and Vollrath 1999). Considering the importance of fluidic forces on the flow and crystallization of silk fibroin, it is very likely that the geometry of the gland plays an important role in the fiber spinning process. Leveraging the recent viscosity measurements of Kojic et al. (Kojic, Bico et al. 2006) and previously published data on the geometry of the *Nephila Edulis* MA and *Bombyx Mori* silk glands (Knight and Vollrath 1999; Asakura, Umemura et al. 2007), we have performed finite element method simulations (FEMs) of the non-Newtonian flow in the silk gland of both organisms in order to further elucidate the role of the flow on the formation of silk fibers.

2.3 Methods Section

a. Data acquisition

The shape of the *Nephila Edulis* MA silk gland was obtained from Knight et al. (Knight and Vollrath 1999) and the shape of the *Bombyx Mori* silk gland from Asakura et al. (Asakura, Umemura et al. 2007). Data points were manually extracted from the figures using the GRABIT software (Doke 2005) in MATLAB 2007 (Mathworks, Inc). For each figure, data was extracted three times, and the values averaged. The radius (r, in μm) of each gland as a function of axial position (z, in μm) was fit to a two-stage exponential function ($r(z) = ae^{bz} + ce^{dz}$) using the MATLAB curve-fitting toolbox. For the spider, a = -0.004886 μm, b = 0.0003718 μm^{-1}, c = 53.52 μm, and d = -9.989 x 10^{-5} μm^{-1} (R^2 = 0.9735). For the silkworm, a = 139.8 μm, b = -0.00197 μm^{-1}, c = 58.45 μm, and d = -3.58 x 10^{-5} μm^{-1} (R^2 = 0.9824).

The resultant curves were calculated every 100 µm, and this data was imported into AutoCAD 2006 (Autodesk) and connected as a polyline. Curves were subsequently imported into COMSOL Multiphysics 3.4 (COMSOL AB) as axisymmetric structures.

b. Numerical Simulation

Finite element simulations were performed using the COMSOL Non-Newtonian Fluid Flow solver. All simulations were isothermal. Geometry meshes were automatically generated by COMSOL. Because of the high length-to-width aspect ratio of the structures, the radial axis was scaled up five times before meshing and subsequently rescaled to its original size. Typical meshes contained approximately 15 000 elements. Viscosity data for the native *Nephila Clavipes* (MA gland) and *Bombyx Mori* silk solutions were obtained from Kojic et al. (Kojic, Bico et al. 2006). It should be noted that the obtained geometry is from the *Nephila Edulis* spider and the obtained viscosity data from the *Nephila Clavipes* spider. However, the two different species are often studied interchangeably (Vollrath and Knight 2001). Kojic et al. fit their viscosity data to a Carreau-Yasuda viscosity model, which adequately captures the observed zero-shear rate plateau regime and shear-thinning behavior of silk solutions. However, the rheology of liquid crystalline solutions is quite complex, as it is usually coupled with the development of liquid-crystalline textures and requires multiple viscosity coefficients for an adequate description of flow behavior (Donald and Windle 1992; Larson 1999). Other models, such as the Leslie-Ericksen theory for the viscous stress of nematics, could be more relevant, by including the effects of molecular alignment on stress (Donald and Windle 1992; Larson 1999). Until studies are available that correlate the molecular alignment, structure, and rheological behavior (i.e., that specify the values of the multiple material constants in the Leslie-Ericksen theory), we are limited to simplified models of the flow of silk secretions.

The Carreau-Yasuda model describes non-Newtonian viscosity by,

$$\eta(\dot{\gamma}) = \eta_0[1 + (\dot{\gamma}\lambda)^a]^{(n-1)/a},$$

where η is viscosity as a function of shear rate $\dot{\gamma}$, η_0 is the zero-shear viscosity, λ is a relaxation time of the fluid, a represents the rate of transition from zero-shear viscosity to shear-thinning behavior, and n is the exponent characterizing the shear-thinning regime. For *Nephila Clavipes*, Kojic et al. found η_0 = 3 500 Pa·s, λ = 0.40 s, a = 0.68, and n = 0.18. For *Bombyx Mori*, they found η_0 = 5 200 Pa·s, λ = 0.57 s, a = 0.80, and n = 0.17. These values were measured from silk secretions gathered from the storage sac of a spider MA gland and a silkworm gland, restricting the rheological data to solutions from those areas, and not necessarily representing changes in micro-structure that develop along the length of the gland. Furthermore, Kojic et al. extracted silk secretions in distilled water for approximately 5 minutes, which could potentially alter the structure and rheology of the silk dope. We note that no data on fluid elasticity is available for either solution, so non-Newtonian effects are restricted to those associated with shear-

thinning of the viscosity. The density of natural silk secretion was assumed to be 1.15 g/cm^3 (Viney 1997).

The gland wall was specified to have a no slip boundary condition. Silkworms, however, are known to secrete another protein, sericin, around their silk secretions as it flows through the silk gland (Kataoka and Uematsu 1977; Kaplan, Adams et al. 1994). Whereas sericin acts as glue in the formation of the cocoon, it is also believed to act as a lubricating layer in the silk gland, reducing the pressure drop required for flow (Kataoka and Uematsu 1977; Kojic, Bico et al. 2006). Due to the technical challenges associated with modeling a two-phase flow, particularly in the absence of rheological characterization of the sericin layer, we are ignoring the presence of sericin and its effects on flow.

Gland entrance and exits were specified to have inlet pressure and outlet pressure boundary conditions, respectively. In order to achieve the desired outlet flow rate, the inlet pressure was iteratively adjusted until the outlet flow rate was approximately as desired. For all simulations, values for conservation of mass and mesh convergence were checked to be within 5%. Mesh convergence was checked for conservation of mass at the inlet and outlet, as well as at nodal values for velocity along the gland length.

2.4 Results and Discussion

a. Velocity Along the Silk Gland

Figure 1 shows the velocity profile along the *Nephila* MA and *Bombyx* silk glands, when a fiber is drawn at physiological spinning rates (10 mm/s – 20 mm/s)(Vollrath and Knight 2001; Shao and Vollrath 2002). For these rates, the Reynolds' Number (*Re*) in the gland is small ($Re << 1$) indicating that the flow is laminar (Table 1). The color map indicates the magnitude of the velocity vector; in the lower figure the cross-sectional average total velocity is shown as a function of axial position along the gland (of course, since we are averaging over a cross-sectional surface whose normal points in the axial direction, only the axial velocity component contributes to the average). Henceforth, total velocity refers to the magnitude of velocity vector (accounting for both axial and radial components).

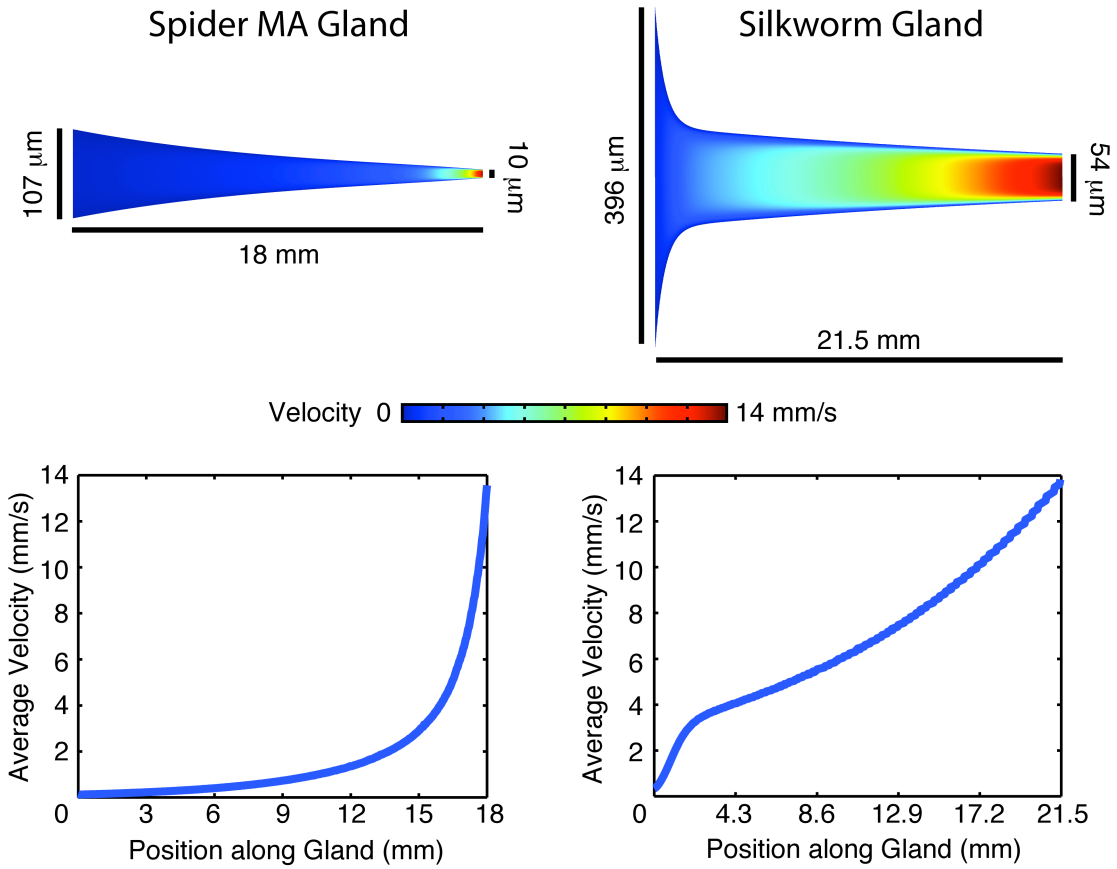

Figure 1. Magnitude of the velocity vector (top) and cross-sectionally averaged total velocity (bottom) along the MA silk gland of the spider (left) and silkworm silk gland (right). Note the difference in scale between the radial and axial axes.

Despite the glands of each organism fitting well to a two-stage exponential function, their shapes are quite different. The spider MA gland has a slow and steady decrease in radius, whereas the silkworm gland has a more sudden drop, and then a slow decrease in radius. This difference in shape induces quite different average velocity profiles along the glands (Figure 1). In the spider, the velocity increases at a low rate and then rises dramatically with axial distance along the gland. A similar velocity profile was obtained by Kojic et al. from a mass balance-based numerical simulation of a uniformly moving cross section of silk through the *Nephila Clavipes* MA gland(Kojic, Kojic et al. 2004). In the silkworm, however, there is an initial rapid increase in velocity followed by a much slower rate of increase along the gland. The pressure drops required to produce these physiological velocity profiles are on the same order as previously published results of 40 MPa and 50 MPa for the spider (Kojic, Bico et al. 2006) and silkworm (Moriya, Ohgo et al. 2008), respectively. The pressure values from previous reports were also obtained from simulations of silk fibroin flow in the gland. The values, however, are theoretical only, and are used to mimic the tension exerted on the dope during the drawing of a silk fiber. Accurate measurements of physiological spinning speeds and tensions have been performed for the vertical fall of a spider (Ortlepp and Gosline 2004). These measurements revealed that physiological spinning

speeds range from 0.05 to 1.30 m/s and physiological drawing tensions range from 10 to 20 MPa on the fiber. For a 3 μm diameter fiber, that is ~8 μm in diameter within the gland, these tensions correspond to a tension in the silk gland of ~1.1 to 2.2 MPa. Based on these considerations, we repeated our simulations on the spider MA gland with an applied pressure drop of 1.7 MPa to report more physiologically relevant results. The applied pressure drop corresponds to an outlet velocity of 3.65 μm/s, well below the measured range, as well as a highly unreasonable fluid particle residence time of 1.51 x 10^5 s. The latter value demonstrates the limitations of such simplified simulations. It is likely that additional lubrication layers in the silk glands (see Methods) lead to the low physiological drawing tension, and cause the same applied tension to be too low to produce realistic results.

Table 1. Simulation parameters and results. Inlet and outlet velocities are cross sectional averages of the total velocity along the boundary. The Reynolds' number here is defined as $Re = \rho V d/\eta_o$, where ρ is the fluid density, V is the average velocity at the inlet, d is the diameter at the inlet, and η_o is the zero-shear rate viscosity defined in the text.

	Re	inlet velocity (mm/s)	outlet velocity (mm/s)	pressure drop (Pa)	residence time (s)
Nephila	4.92×10^{-9}	0.140	13.7	5.40×10^{7}	38.6
Bombyx	2.92×10^{-8}	0.334	13.8	3.09×10^{7}	4.79

From the long and slender contraction geometry of both silk glands, one would expect to be able to approximate the flow behavior with a lubrication theory model of flow in a tapered channel. This problem has been previously solved for both Newtonian and Power Law fluids in linearly tapered tubes (Bird, Hassager et al. 1987). However, this analytical lubrication theory approximation (treating the gland as having a linear taper) of Newtonian flow in the spider MA gland underestimates the necessary pressure drop by over 25%, in comparison to a Newtonian simulation. The error increases further when additionally attempting to account for non-Newtonian flow behavior, or when analyzing the silkworm silk gland, which has a much sharper taper than that of the spider MA gland. Therefore, the published analytical lubrication model does not serve as an accurate approximation of flow behavior in the silk glands and should be applied with caution.

Figure 2 shows profiles of total velocity as a function of radial position at various positions along the gland length. Whereas the plots are of total velocity, axial velocity plots look identical because the relative magnitude of the radial velocity is much smaller than the axial velocity. Because the silk solution is highly shear thinning, the cross-sectional velocity profile forms a highly blunted flow profile, rather than the commonly seen parabolic velocity profile of Newtonian Poiseuille flow. Due to this thin high shear rate layer, the flow at any axial position in the gland is essentially a plug flow. This shear-thinning behavior has a significant beneficial effect on the pressure drop required to flow silk solution.

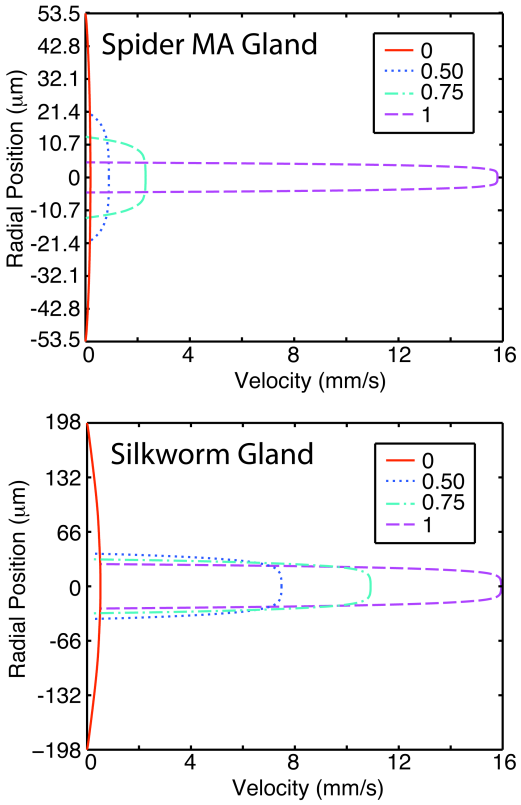

Figure 2. Radial cross-section velocity profiles at various positions along the gland lengths, indicated in the legend by axial position scaled by the total gland length. (top) Spider gland, (bottom) silkworm gland. The blunted shape of the velocity profiles is due to the shear-thinning behavior of the silk solution.

For example, if the silk solution were a Newtonian fluid, and not shear thinning, the pressure drop required to flow the solution at the same rate would be two orders of magnitude higher for both the spider and the silkworm (determined by simulation of the flow as a Newtonian fluid with the zero-shear viscosity as the Newtonian viscosity). Therefore the shear-thinning character of the silk solution—also a feature of most other liquid crystalline polymers (Donald and Windle 1992; Larson 1999) — greatly facilitates low energy fiber spinning.

b. Residence Time in the Gland

From the velocity profile along the length of the gland, we calculated the mean residence time of a fluid particle in the gland. Residence time (t_{res}) is the amount of time that a particle is exposed to the imposed flow field, and is herein defined by,

$$t_{res}(z) = \int_0^z \frac{dz}{V_{avg}(z)},$$

where V_{avg} is the cross-sectional average of the velocity at a position along the gland, z. It is known that although extendable molecules show a stochastic distribution of stretching in both shear and extensional flow fields, their residence time is positively correlated to the amount of stretching of the molecules (Perkins, Smith et al. 1997; Smith, Babcock et al. 1999). Consequently, the longer a fibroin molecule is in the gland, the more elongated and aligned it will be along the gland axis. Our calculations (Table 1) indicate that silk dope in the spider MA silk gland has a residence time eight times longer than silk dope in the silkworm gland. This is particularly noteworthy considering that both glands are of similar lengths, and with the same approximate inlet and outlet velocities. Reexamining the velocity profiles along the gland (Figure 1), the extended residence time in the spider is due to the much slower fluid acceleration along the gland.

Both the spider and silkworm maintain ionic gradients, as well as extract water from the silk solution, along the lengths of their glands (Foo, Bini et al. 2006). A rough calculation of diffusion distance ($x = \sqrt{4Dt}$, where t is time and D is the diffusion coefficient) using the diffusion coefficient of water through native spider silk dope(Kojic, Kojic et al. 2004) ($D = 2.15 \times 10^{-5}$ mm^2/s) suggests that the short residence time in the silkworm does not leave enough time for complete diffusion of water or ions from the gland edge to the center of the dope. The longer residence time of the spider MA gland potentially allows much more judicious regulation of the water and ionic content of the silk dope. These diffusion calculations are approximate and obviously do not account for the effects of advection or, potentially, stress-induced diffusion.

c. Shear and Extension

In order to further understand the role of flow fields and hydrodynamic forces within the silk gland, we have plotted the magnitude of the rate of strain tensor and a flow type parameter throughout the flow fields as well as calculated characteristic shear rates and characteristic extension rates along the gland lengths. Roughly speaking, shear forces are a result of “sliding” of the silk solution against the gland wall, and extensional forces are a result of stretching along the flow axis. In particular, since the silk glands have a funnel shape, their decreasing diameter causes a spatial acceleration along the flow direction, stretching fluid particles. Combined with the shear effects at the gland wall, the silk gland creates a mixed shear and elongational flow. The elongational component has recently been demonstrated, *in vitro*, to be necessary for silk fiber formation (Rammensee, Slotta et al. 2008). Due to the complexities associated with each, shear and elongational flow are commonly analyzed independently (Macosko and Larson 1993). However, their combined effect is of significant interest to the polymer rheology community because of its role in the dies used for polymer fiber spinning, extrusion, and other processing flows (Bird, Hassager et al. 1987; McKinley and Sridhar 2002).
A flow type parameter can be used to assess the relative proportion of the rotational and elongational components of a flow field. We plotted the dimensionless flow type parameter (ξ) for each gland, as previously defined (Lee, Dylla-Spears et al. 2007),

$$\xi = \frac{\left|\dot{\underline{\underline{\gamma}}}\right| - \left|\underline{\underline{\omega}}\right|}{\left|\dot{\underline{\underline{\gamma}}}\right| + \left|\underline{\underline{\omega}}\right|},$$

where $\left|\dot{\underline{\underline{\gamma}}}\right|$ is the magnitude of the rate of strain tensor, and $\left|\underline{\underline{\omega}}\right|$ is the magnitude of the vorticity tensor. The flow type parameter varies from -1 (pure rotation) to 0 (shear) to 1 (pure elongation).

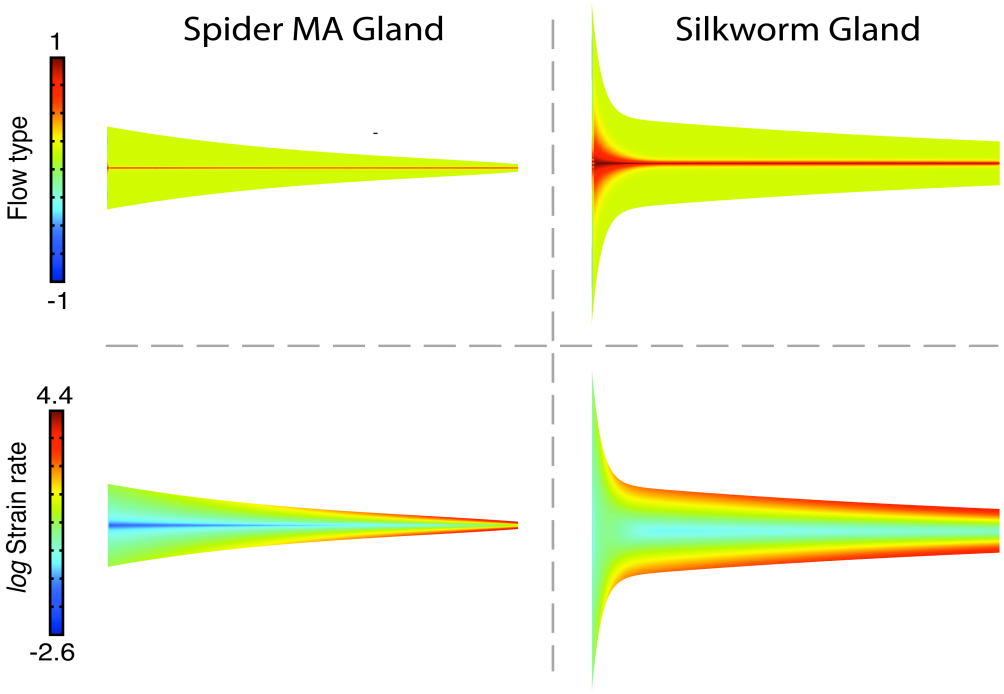

Figure 3. Flow type parameter (top) and magnitude of the rate of strain tensor (bottom) in the MA silk gland of the spider (left) and silkworm silk gland (right).

As seen in Figure 3 (top), the axial centerline of both silk glands contain purely elongational flow, as expected for a contraction geometry (Oliveira, Alves et al. 2007). It is in this location that polymer molecules likely experience the most stretching. Farther from the axial centerline of the gland, the flow is predominately shear ($\xi \sim 0.2$) due to the no slip boundary at the gland wall. This is highlighted in the plots of the magnitude of the rate of strain tensor ($\left|\dot{\underline{\underline{\gamma}}}\right|$) in Figure 3 (bottom). In both glands, $\left|\dot{\underline{\underline{\gamma}}}\right|$ ranges over several orders of magnitudes with the rate of strain highest at the walls and closer to the gland outlet. As mentioned above and discussed further below, we do not model the flow of any fluid layers around the silk secretions (e.g. sericin). However, if sericin does indeed act as a lubricant in the silkworm silk gland, the rate of strain induced by the wall would likely be significantly reduced.

To provide a global description of flow in the glands, we calculated the characteristic shear rate ($\dot{\gamma}$) along the gland length as,

$$\dot{\gamma}(z) = \frac{V_{avg}(z)}{r(z)},$$

and the accumulated shear strain (γ),

$$\gamma(z) = \int_0^{t(z)} \dot{\gamma}(z)dt = \int_0^z \dot{\gamma}(z)\frac{dz}{V_{avg}(z)},$$

where *t* is the total time of exposure to the flow field (i.e. residence time). Whereas shear rate describes the local rate of shear deformation, the accumulated shear strain is a function of both the magnitude of the shear field and the residence time within it (Bird, Hassager et al. 1987). As mentioned, both residence time and accumulated strain units have been shown to be positively correlated with the total amount of stretching of polymeric molecules (Perkins, Smith et al. 1997; Smith, Babcock et al. 1999), and it has been demonstrated that repeated exposure of silk fibroin to identical shear fields induces irreversible changes in its material properties (Holland, Terry et al. 2006). Finally, as suggested by Figure 2 and shown in Figure 3, we note that the local shear rate varies considerably with radial position, with the local shear rate going to zero at the centerline and reaching a maximum near the walls of the gland. Our characteristic shear rate, which neglects these radial variations, thus leads to an underprediction of the shear rate and shear strain experienced by near-wall fluid elements.

Like the velocity profiles for the two organisms, the characteristic shear rate profiles are distinctly shaped (Figure 4). However, the shear rate in the spider MA gland is an order of magnitude greater than that in the silkworm gland. Because the outlet velocities are approximately similar, this is primarily due to the small radius of the spider MA gland. Furthermore, the spider MA silk dope accumulates almost double the total average shear strain units of that of the silkworm before exiting the gland. In combination with the extremely long residence time of silk dope within the spider MA silk gland, the higher accumulated shear strain suggests that the slow stretching of the fibroin molecules over a long period of time could be a cause of different mechanical properties between spider MA silk fibers and silkworm silk fibers.

Our reported values of shear rates in the glands for both organisms are orders of magnitude higher than those generally discussed in the literature (the critical shear rate of fibroin crystallization is generally reported to be between 1 and 10 s^{-1} (Iizuka 1966; Iizuka 1983; Yamaura, Okumura et al. 1985; Holland, Terry et al. 2006; Xie, Zhang et al. 2006; Moriya, Ohgo et al. 2008).) This is largely due to our definition of shear rate, which is based on a radially-averaged velocity profile, rather than fully accounting for the radial variations of shear rate. The FEM of the *Nephila Clavipes* MA silk gland performed by Kojic et al. (Kojic, Kojic et al. 2004), which is based on mass balance and neglects any radial variations in flow, suggests shear rates up to ~1 500 s^{-1} at the outlet, on the same order as those reported here for the same gland. (Shear rates were not explicitly calculated in their report; rather, we performed the calculations based off their reported velocities and geometries.) Moriya et al. (Moriya, Ohgo et al. 2008) performed

an FEM simulation of flow in the silkworm gland based on their own viscosity and shear rate measurements. They reported shear rates of 0 to 2.5 s^{-1} along the centerline of the silkworm gland, but did not explicitly discuss details of differences between local and global flow kinematics. However, our simulations of the silkworm gland suggest similar local, centerline strain rates ranging from 0.5 to 3.5 s^{-1}.

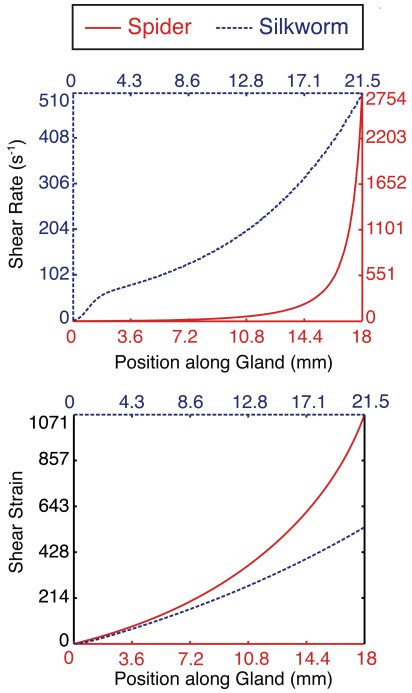

Figure 4. Characteristic shear rate (top) and characteristic accumulated shear strain (bottom) along the silk glands. Note the different scales for the the characteristic shear rate in spider MA and silkworm glands.

We define the characteristic extension rate ($\dot{\varepsilon}$) by,

$$\dot{\varepsilon}(z) = \frac{dV_{center}(z)}{dz},$$

where V_{center} is the centerline axial velocity of the fluid at a position, z. Although the cross-sectional average axial velocity is used in the definition of shear rate, the centerline axial velocity is conventionally used in characterizing extensional flows in converging channels (James, Chandler et al. 1990; James 1991; Oliveira, Alves et al. 2007) (further justified by the fact that the centerline is the location of pure elongational flow, Figure 3). We define accumulated extensional strain (ε),

$$\varepsilon(z) = \int_{t(z_0)}^{t(z)} \dot{\varepsilon}(z)dt = \int_{z_0}^{z} \dot{\varepsilon}(z)\frac{dz}{V_{avg}(z)}.$$

The onset of the polymer coil-to-stretch transition occurs above a critical extension rate ($\dot{\varepsilon}_{crit}$),

$$\dot{\varepsilon}_{crit} \approx \frac{0.5}{\lambda},$$

where λ is the polymer relaxation time (Bird, Hassager et al. 1987; Perkins, Smith et al. 1997). Herein, we use the relaxation time from the Carreau-Yasuda model, as described above. Because polymer stretching only occurs above this critical rate, we have considered "useful" accumulated extensional strain by integrating only those areas of the extension rate curves above $\dot{\varepsilon}_{crit}$. In the silkworm gland, the extension rate profile is not monotonic, and falls above and below the critical extension rate (Figure 5). Whereas polymer relaxation could occur during the period of below-critical extension rate, negating the earlier effects of stretching, Holland et al. demonstrated that repeated shearing of silkworm dope caused an irreversible increase in the storage modulus of the dope, despite allowing >10 minutes for relaxation (Holland, Terry et al. 2006; Holland 2008). Therefore, in our calculation of "useful" accumulated extensional strain (above the critical extension rate), we sum the integrals of all useful extension.

From the extension rate profile (Figure 5), it is immediately obvious that neither silk gland is shaped as a constant extension rate funnel, as has been previously suggested for the spider MA gland (Knight and Vollrath 1999; Vollrath and Knight 2001). Constant extension rate funnels have been under investigation in the fiber spinning community because they are believed to minimize the pressure drop required for flow as well as induce and maintain the highest degree of molecular alignment in a solution (LaNieve 1975; Crater and Cuculo 1983; Chen, Cuculo et al. 1992). The spider MA gland actually acts as an increasing extension rate funnel, perhaps in order to maintain extension despite the strain hardening character of highly strained silk dope (Kojic, Bico et al. 2006).

The maximum extension rate in the spider silk MA gland rises to an order of magnitude higher than that in the silkworm gland. However, the extension rate in the silkworm gland exhibits a unique behavior. There is an initial spike and subsequent drop in extension rate (a "pre-extension") along the gland. Whereas the accumulated extensional strain in the spider MA gland is nearly linear, the aforementioned spike of extension rate in the silkworm gland manifests as an initial sudden rise in accumulated extensional strain. The total accumulated extensional strain in both the spider and silkworm is similar, despite the maximum extension rate in the spider MA gland being an order of magnitude higher than in the silkworm gland. The "pre-extension" enables the silkworm to achieve the same total accumulated extensional strain as the spider, at lower extension rates. Pre-shearing in the direction of polymer extension has been shown to more rapidly induce the onset of strain hardening(Anna and McKinley 2007). Furthermore, the pre-extension could be a mechanism of achieving a higher total level of accumulated extensional strain despite the significantly shorter residence time of the silk dope in the silkworm gland. It is also noteworthy that both the spider MA and the silkworm glands accumulate similar magnitudes of total extensional strain, suggesting

that accumulated shear strain is more important than extensional strain in the formation of spider dragline silk fibers.

In the spider MA gland, useful accumulated extensional strain begins near the end of the gland, around where the silk dope generally detaches from the gland wall and draws down into a fiber. Also, after a steady plateau of useful extension in the silkworm gland, useful extension begins to increase again similarly near the gland outlet. This suggests that critical extension rate and extensional strain may play a role in initiating drawdown and fiber formation in the glands. Notably, this area around the drawdown taper is the location of an abrupt increase in molecular alignment along the fiber axis, as measured by polarized Raman spectroscopy (Lefevre, Boudreault et al. 2008).

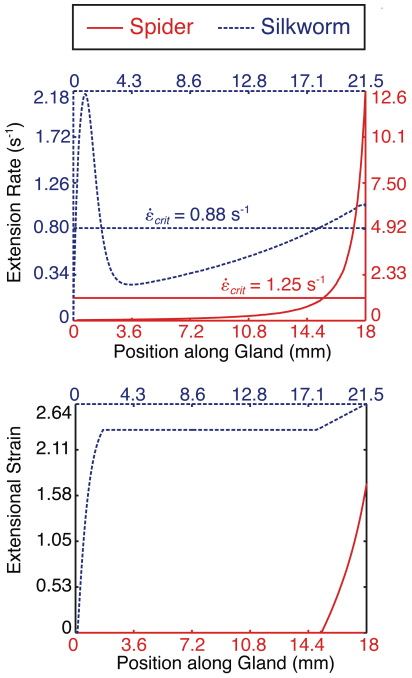

Figure 5. Characteristic extension rate (top) and useful accumulated extensional strain (bottom) along the silk glands. The horizontal lines indicate the critical extension rate for polymer stretching. Note the different scales for the characteristic extension rate in the spider MA and silkworm glands.

d. Effects of Spinning Speed

Whereas the spider and silkworm normally spin silk in the range of 10 mm/s to 20 mm/s, forced silking is generally performed at a variety of different rates. These different drawing conditions of silk fibers have a significant effect on the mechanical properties of the resultant fibers (Vollrath, Madsen et al. 2001). It is unknown, however, exactly why spinning speed alters fiber properties, but it is likely due to the increased degree of molecular alignment induced by the stretching of the fiber (either during flow or post-spin drawing) coupled, possibly, with decreased time for diffusion of water and ions. It has been observed that as draw rates are increased, the drawdown taper (the point at which the silk dope significantly solidifies and detaches from the gland wall) occurs at

an earlier position within the gland (Asakura, Umemura et al. 2007). Alongside this, similar shifts in the positions of maximum birefringence (and thus molecular alignment) within the gland at various draw rates have been observed (Magoshi, Magoshi et al. 1985; Asakura, Umemura et al. 2007). To investigate these effects, we performed simulations at spinning rates comparable to those used in forcible silking (0.1 mm/s, 15 mm/s, 50 mm/s, 100 mm/s). The results are shown in Table 2 and Figure 6.

It is believed that the drawdown taper begins when the silk dope is exposed to a critical shear rate, at which point a dramatic crystallization of the fibroin protein occurs (Asakura, Umemura et al. 2007; Moriya, Ohgo et al. 2008). *In vitro* experiments with native and regenerated silkworm fibroin suggest that this rate is within 1 to 10 s^{-1} (Iizuka 1966; Iizuka 1983; Yamaura, Okumura et al. 1985; Holland, Terry et al. 2006; Xie, Zhang et al. 2006; Moriya, Ohgo et al. 2008). Knight et al., from which we extracted the *Nephila* MA gland geometry, indicated that the drawdown taper occurred when the gland narrowed to 20 μm in diameter when drawing at 100 mm/s (Knight and Vollrath 1999). Our simulations of these conditions would thus suggest a critical shear rate of ~2 500 s^{-1} (and a critical extension rate of ~10 s^{-1}) for spider silk dope. As explained above, we believe this shear rate value to be considerably greater than measured critical shear rates due to the fact that our definition of characteristic shear rate incorporates the substantial radial variations in local shear rates. It is worth noting, however, that the centerline strain rate at this same axial location in the gland is 3 s^{-1}.

It is unclear to which flow characteristics the refolding and crystallization of silk fibroin is most responsive (e.g. deformation rate, accumulated strain, etc). Our simulations of different drawing rates show dramatically different residence times (Table 2) and shifts in magnitude of shear and extension rate profiles (Figure 6). On the other hand, accumulated shear strain is not significantly altered by drawing rate (data not shown). As draw rate increases in the spider MA gland, the location at which the extension rate reaches the critical value (and extensional strain becomes useful) moves farther back into the gland (Figures 6, 7), similar to the shift in position of the drawdown taper at different spinning speeds, suggesting that surpassing the critical extension rate of the polymer molecules is the initiating factor for the drawdown taper. The silkworm gland exhibits a different extensional strain profile, whereby at drawing speeds significantly above physiological rate, all the extensional strain becomes useful (Figures 6,7). Similar to accumulated shear strain, accumulated extensional strain (when the entirety of the extension rate profile is above the critical rate) is not significantly altered by drawing rate (Figure 7). The lack of significant variation in accumulated shear strain and the aforementioned accumulated extensional strain for different drawing rates is expected because, as we have defined them, they are determined primarily by the geometry (as the integral of dz/r). However, because of shear-thinning, slight variations at different drawing rates may arise due to changes in the local strains near the wall.

Lastly, at the lowest drawing speed (0.1 mm/s), neither organism achieves extension rates above their respective critical values. However, fibers can obviously be artificially reeled at these speeds, albeit resulting in different mechanical properties than normal (Vollrath, Madsen et al. 2001). It is possible that at this drawing rate, fiber

formation occurs due to shear and ionic effects alone, with little polymer extension and alignment.

Table 2. Silk dope residence time at various silking speeds. Drawing rates are approximate because pressure boundary conditions were applied in simulations. See Figure 6 legends for actual drawing rates.

approximate drawing rate (mm/s)	residence time (s)	
	spider	silkworm
0.1	4 790	548
15	38.6	4.72
50	10.2	1.29
100	5.16	0.643

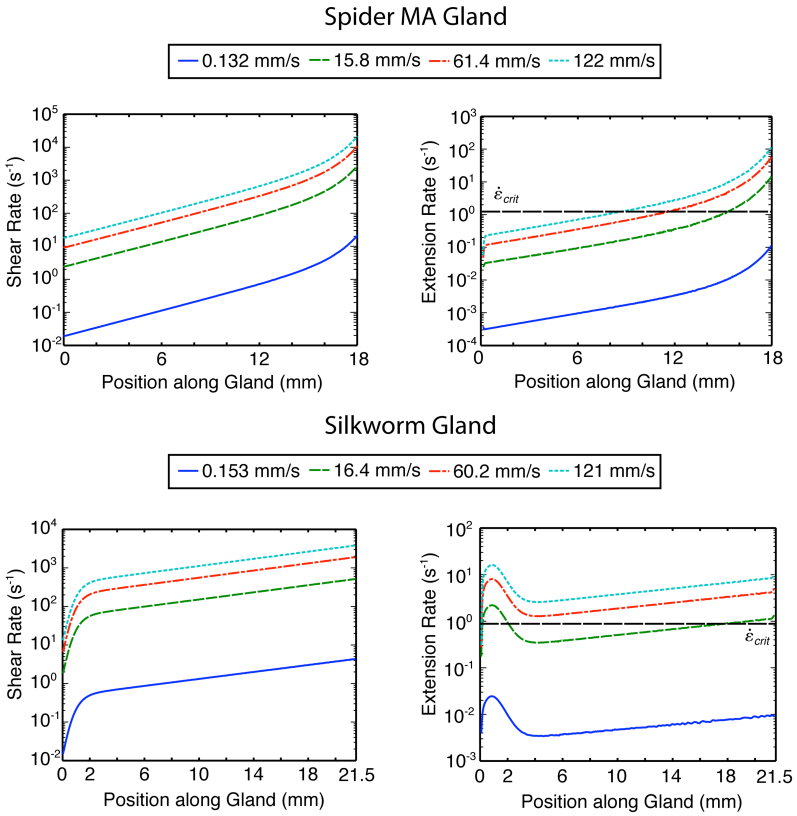

Figure 6. Effect of spinning speed on shear rate (left) and extension rate (right) profiles in the spider (top) and silkworm (bottom) glands. Legends indicate average exit velocities, representative of drawing rates. Note that the vertical axis is a logarithmic scale for visualization of the significant magnitude shifts.

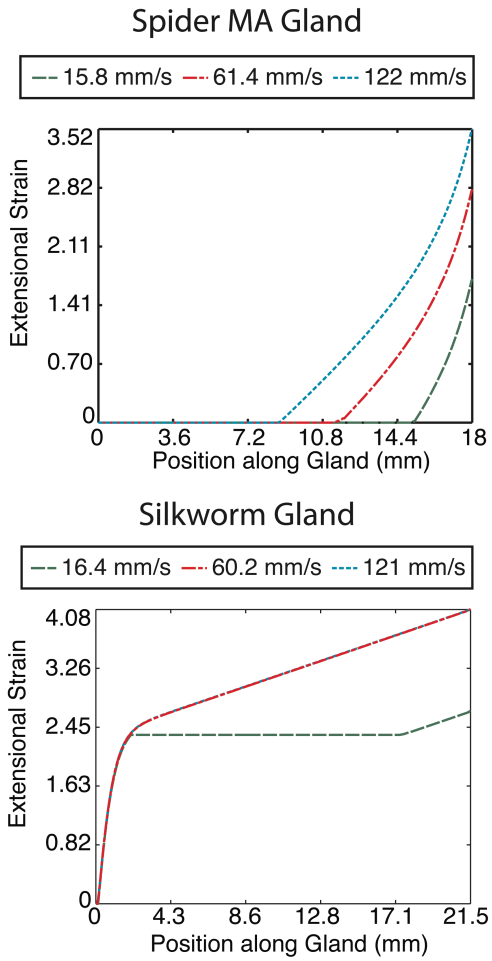

Figure 7. Useful accumulated extensional strain in the spider MA gland (top) and silkworm gland (bottom) for different draw rates. There is no useful accumulated extensional strain for drawing at 0.1 mm/s. Note that the curves for the two higher drawing rates in the silkworm gland are identical (discussed in text).

e. Limitations of Numerical Simulations

Many assumptions are inherent in performing these simulations on the spider MA and silkworm silk glands. Assumptions of considerable importance are:

(1) *The silk secretions are considered homogeneous*. Despite the macroscale similarity between the rheological properties of the spider MA and silkworm dopes (Holland, Terry et al. 2006), the two secretions have quite different molecular compositions that develop into different microstructures. *Nephila* MA silk secretions consist of two proteins, MaSp1 (~275 kDa) and MaSp2 (~740kDa) (Hinman, Dong et al. 1992; Hinman and Lewis 1992; Guerette, Ginzinger et al. 1996). MaSp1 is most abundant in the dragline fiber, with MaSp2 heterogeneously distributed (Sponner, Unger et al. 2005). Both MaSp1 and MaSp2 contain poly-alanine and glycine-alanine repeats, thought to form crystalline domains. MaSp2, however, contains significantly more proline than MaSp2, which is thought to confer much of the elasticity to the fiber.

Silkworm silk secretions are composed of two proteins in a 1:1 ratio: a heavy chain (~390 kDa) and a light chain fibroin (~26 kDa) that are held together by a disulfide bond (Kaplan, Adams et al. 1994). Silkworm fibroin amino acid sequences consist primarily of repeats of glycine alternating with alanine, serine, threonine, and valine. These differences in molecular composition between spider MA and silkworm silk secretions can manifest as distinct microstructures and supra-molecular architectures, which we ignore in these simulations by only considering the rheological properties of storage sac silk secretions. Future work would benefit from the coupling of models describing the various hierarchies of molecular ordering and structure such as liquid crystal alignment and the development of mesogen structural morphology (Viney 1997; Johnson and Martin 1999; Braun and Viney 2003; De Luca and Rey 2006).

(2) *Only the effects of shear-thinning of the viscosity are considered.* Neither elongational viscosity nor the effects of fiber solidification are taken into account. Whereas these factors are extremely important in polymer processing, they are difficult to both measure and model. Kojic et al. were able to use their specialized elongational rheometer to measure the elongational effects on native spider silk solution (Kojic, Bico et al. 2006). However, implementing their measurements into a numerical simulation remains a considerable challenge.

(3) *No slip boundary conditions are assumed at the gland wall*. Whereas we assume no-slip contact between the fluid and the gland wall, the exact interface boundary conditions are unclear (Vollrath and Knight 2001; Kojic, Bico et al. 2006). For example, as the silk solution progresses down the gland, water diffuses out of the solution, potentially creating a lubrication layer at the gland wall. Furthermore, both the spider and silkworm have been shown to secrete additional lipid and protein layers in the glands (Vollrath and Knight 2001), which could induce varying interface flow effects between the silk solution and the gland wall. This is particularly likely in the secretion of the sericin protein in the silkworm gland, as discussed in the Methods section.

(4) *Ionic effects on the viscosity of the silk solution are neglected*. The cells lining the walls of the silk gland regulate the ionic content of the silk solution, and vary the ionic content along the gland length. It has been shown that these ions play a significant role in regulating the folding of the silk protein, as well as affecting the viscosity of the silk solution (Chen, Knight et al. 2002; Dicko, Kenney et al. 2004; Terry, Knight et al. 2004; Foo, Bini et al. 2006).

(5) *Gland curvature is ignored*. The major and minor ampullate silk glands of the spiders are generally referred to as “S-shaped” because they wrap over themselves twice (Vollrath and Knight 2001). Silkworm glands also exhibit a similar shape. We neglect this curvature and consider the gland as a straight funnel to simplify axisymmetric simulations. It is possible, however, that the different radii of curvature at the inside and outside of these bends induce additional strain in the flow, or even secondary flows (Pathak, Ross et al. 2004; Schonfeld and Hardt 2004; Sudarsan and Ugaz 2006) Compared to the length scale of the entire gland, and the total

strain accumulated along its length, any additional extension induced by the bends is likely minimal.

(6) *The arbitrary nature of selecting the gland geometries*. Because the gland shapes were extracted from previously published data (Knight and Vollrath 1999; Asakura, Umemura et al. 2007), there is uncertainty as to whether the length-wise bounds of the simulated geometries are representative of the physiologically relevant gland boundaries. Particularly in the case of the silkworm, the entirety of the gland extends much farther back than the simulated geometry and actually consists of two ducts that converge into the one duct analyzed herein. This leaves open to question the role of flow in those additional areas and their upstream effects.

2.5 Conclusions

The flow fields in the spider MA and silkworm silk glands were investigated through FEM simulations. Our results demonstrate that the shear-thinning behavior of natural silk secretions considerably assists in the low-pressure silk fiber spinning process. Analysis of the velocity fields in both glands demonstrates that despite their similarly tapered geometry, the glands produce significantly different velocity fields during flow. These differences in velocity fields induce distinct shear and extensional flow fields. Analysis of the shear and extensional flow fields show that the shear rate and accumulated shear strain reach higher magnitudes in the spider MA gland than the silkworm gland. Additionally, despite a greater magnitude final extension rate in the spider MA gland, the accumulated extensional strain in both organisms is of similar magnitude, suggesting that shear may be the dominant force in inducing the improved mechanical properties of spider silk over silkworm silk. Our results also indicate that the residence time within the spider MA gland is eight-fold greater than in the silkworm gland, allowing greater exposure to shear and extensional fields as well as more time for the diffusion of ions and extraction of water. We furthermore simulated the effect of reeling speed on the flow of silk dope in the gland. Whereas the residence time, shear rate, and extension rate magnitudes are greatly altered by spinning speed, average accumulated shear strain is mostly unaffected. Rather, in the spider MA gland, there is a backward shift in the position where the accumulation of useful extensional strain begins with increasing drawing speed (due to a shift in the location of the critical extension rate threshold along the gland). The silkworm gland, however, generates the same amount of accumulated extensional strain at higher than physiological spinning speeds. These results support, at least in the spider, past suggestions that silk dope detaches from the gland walls into a fiber in response to a critical deformation rate, rather than an accumulated level of strain.

We have discussed the limitations of these simulations in representing *in vivo* flow characteristics. In particular, future work in measuring the highly extensional character of the silk dope will be critical to developing more realistic models of the *in vivo* flow of silk solution. Future work will also be required to account for the significant effect of ionic gradients within the gland in altering silk dope viscosity and inducing fiber solidification.

Our results, however, provide an initial step in understanding the role of flow in silk fiber formation, as well as provide insight into the differences between the mechanism of silkworm and spider silk fiber spinning. Studying flow in the 400 million year old (Shear, Palmer et al. 1989), naturally evolved spinnerets of the spider and silkworm glands will assist in the improvement of low energy commercial fiber spinning technologies and the development of new biomimetic systems for fiber spinning.

2.6 Acknowledgment

The authors would like to thank Dr. Robert Wootton for helpful discussions and the reviewers for extremely useful comments and suggestions. This research was partially supported by an NDSEG Graduate Fellowship to D.N.B., University of California Systemwide Biotechnology Research & Education Program GREAT Training Grant 2008-02, National Science Foundation Grant #EEC-0425914, and the Micro/Nano Fluidics Fundamentals Focus (MF3) Center under the DARPA N/MEMS Science & Technology Fundamentals Program.

Chapter 3. Laminar Flow Focusing of Silk

The X-ray diffraction work in this chapter was performed in part with Dr. Anne Martel at the Stanford Linear Accelerator Laboratory.

3.1 Abstract

Silk fibers were produced using the hydrodynamic focusing of reconstituted silk fibroin (RSF) solution in a glass capillary-based microfluidic device. Because of the high viscosity of concentrated reconstituted silk solutions, we determined a means of viscosifying the coagulating sheath flow solution to eliminate flow instabilities. Silk fibers could be produced simply through hydrodynamic focusing or by rapidly reeling fibers, causing a draw down of the silk solution. X-ray diffraction measurements show that the drawn down fibers exhibit *β*-sheet crystallites and a high degree of molecular orientation. Unfortunately, the flow behavior of RSF varied drastically from batch-to-batch and these results were not readily reproducible.

3.2 Introduction

Due to their exceptional mechanical properties, spider silk fibers and the artificial production thereof has been under heavy investigation (Vollrath and Knight 2001). Currently, the only commercial scale source of silk fiber is from the cocoon of the *Bombyx mori* silkworm. However, silkworm silk is much weaker than spider silk, and naturally produced fibers suffer from a large degree of biological variability in size and mechanical properties (Vollrath, Madsen et al. 2001; Shao and Vollrath 2002). To understand how silk fibers are formed, as well as develop processes for artificially producing fibers on an industrial scale, many efforts have been put forth to spin fibers from dissolved silkworm cocoons, most notably efforts in traditional wet spinning (Zhou, Shao et al. 2009). As microfabrication and microfluidics technologies have advanced, researchers have attempted to leverage them to spin microfibers under benign processing conditions. Microfluidic flow is laminar and thus predictable, with mixing of adjacent flow streams occurring primarily by diffusion. By hydrodynamically focusing a polymer solution with a coagulant/gelation agent in the sheath flow, several groups have produced microfibers from UV curable polymers (Jeong, Kim et al. 2004), calcium alginate (Shin, Park et al. 2007), and poly(lactic-co-glycolic) acid (Hwang, Khademhosseini et al. 2008). Herein, we demonstrate a glass capillary-based microfluidic hydrodynamic focusing system for the continuous spinning of silk fibers from concentrated RSF, using methanol as a sheath flow/coagulant (Figure 1).

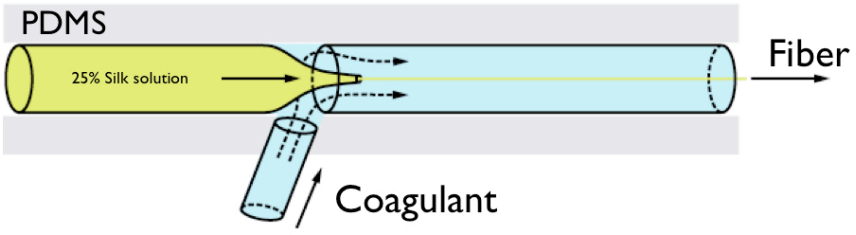

Figure 1. Glass capillary-based microfluidic device for the hydrodynamic focussing of silk fibers.

3.3 Experimental

a. Device Fabrication and Operation

Whereas many groups use planar microfluidic devices for hydrodynamic focusing, these systems confine the core fluid into a rectangular cross-sectional shape. Therefore, almost all efforts to make fibers using microfluidics have involved devices made of concentric glass capillaries. These systems are axisymmetric, focusing the core stream with a circular cross-section and eliminating any contact the fiber forming stream could have with the channel walls. Microfluidic devices were fabricated as shown in Figure 1. A 1 mm diameter wire was inserted into 1.5 mm OD glass capillary silanized with tridecafluoro-1,1,2,2-tetrahydrooctyl-1-trichloro-silane (a). This assembly was covered with PDMS and allowed to cure (b), creating a manifold to hold glass capillaries and allow sheath flow (c). The PDMS manifold was lubricated with IPA and a 750 µm/1.5 mm ID/OD capillary, pulled to a 30 µm ID tip, was inserted into the thinner end of the device. An 840 µm/1.5 mm ID/OD glass capillary was inserted into the other end, just far enough to have the capillaries overlap (d). The RSF flow rate was fixed at 1 mL/hr and sheath flow rates were held fixed at 3 mL/hr for fiber spinning, or varied from 2 to 9 mL/hr for device characterization.

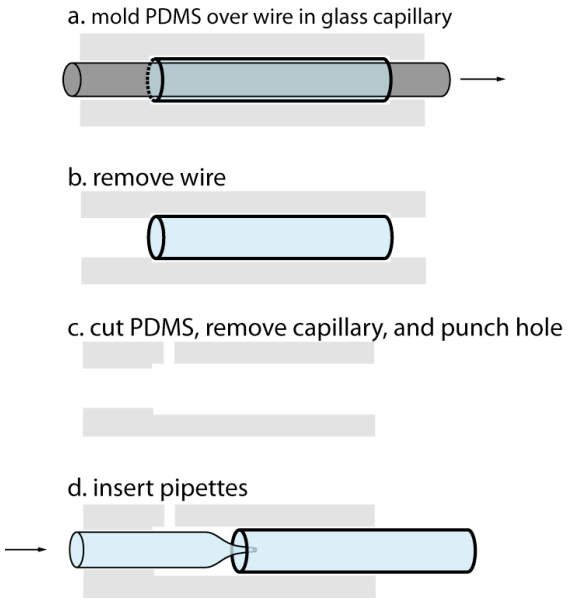

Figure 2. Schematic for device construction. The PDMS scaffold is designed to keep the pipettes centered in one another and allow a sheath flow around the core solution.

b. Preparation of Silk Solution

Reconstituted silk fibroin was prepared as previously described.(Nazarov, Jin et al. 2004) Briefly, *B. mori* silkworm cocoons (Tajima Shoji Co., Ltd., Yokohama, Japan)

were boiled twice in 0.02 M Na_2CO_3 for 20 min and rinsed in deionized water to remove sericin glue. The degummed silk was allowed to dry overnight and was dissolved in 9.3 M LiBr for 4 h. The dissolved silk solution was then dialyzed with 3,500 MWCO cassettes (Pierce Biotechnology, Inc., Rockford, IL) against 2 L of Milli-Q water for 48 h, changing the water regularly at least six times. The resultant 8 wt.-% silk solution (as measured by dry weight) was filtered through a 100 µm mesh to remove large debris and stored at 4°C for no more than 2 months. Silk solution was passed through a 0.22 µm pore syringe filter immediately before use. 10 mL of 8 wt.-% silk solution was concentrated to ~25-30 wt.-% by dialyzing against 400 mL 10% w/v PEG solution (10 kDa) for 22-26 h.

c. Preparation of Coagulant

Methanol is a well-established and strong coagulant for RSF, and was thus used as a sheath fluid. Methanol was viscosified with 80 kDa hydroxypropyl cellulose (HPC, Sigma). From shear-rate dependent viscosity measurements (below), ~15 wt.-% HPC-MeOH was found to be within the appropriate viscosity range for stable flow focusing of concentrated RSF.

d. Rheology

Shear viscosity measurements were performed on a capillary viscometer (Schott-Geräte GmbH). Shear-rate dependent viscosity measurements were performed on a Bohlin Gemini stress-controlled rheometer (Malvern Instruments) using a 4° cone-and-plate geometry for the concentrated silk solution, and a cup-and-bob geometry for coagulant solutions. All measurements were performed at room temperature.

e. X-ray Diffraction

The fiber diffraction patterns were recorded on BL4-2, the BioSAXS beamline of the Stanford Synchrotron Radiation lightsource, using a MarCCD detector. The distance between the sample and the detector was ~30 cm and the wavelength ~1 Å. Background images (with no sample) were subtracted from all sample images.

3.4 Results and Discussion

a. Viscosity Matching

Laminar co-flow of miscible solutions with large viscosity differences can lead to hydrodynamic instabilities and viscous folding (Cubaud and Mason 2006). To minimize these effects, we viscosified our coagulant solutions to that of concentrated RSF. Without sufficient viscosification of the coagulant solution, we observed viscous folding and complete mixing of the silk and coagulant, leading to the formation of a gel and

clogging of devices. Non-viscosified 100% MeOH caused instantaneous solidification of the core silk solution, eliminating flow instabilities, but causing rapid aggregation of silk on the inner pipette tip and almost immediate device clogging. Before clogging, we observed rope-coiling of the fiber in the device, as seen with other microfluidic fiber forming systems (Shin, Park et al. 2007). We also observed that HPC-MeOH solutions took significantly longer to induce fiber formation than 100% MeOH solutions alone.

We used HPC as a viscosifier for the methanol coagulant solution. Viscosity measurements of up to 7% w/v HPC-MeOH were performed with a capillary rheometer, above which the rheometer was unable to measure. These measurements were fit to an exponential curve (Figure 3), from which a concentration of HPC was extrapolated that would create an HPC-MeOH solution with similar viscosity to that of concentrated RSF.

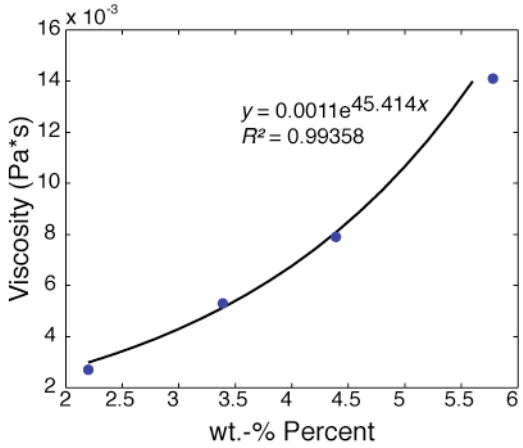

Figure 3. Viscosity of various HPC-MeOH solutions measured with a capillary viscometer, and an exponential fit of the data.

The shear-rate dependent viscosity of ~25% RSF and that of 15 wt.-% HPC-MeOH is shown in Figure 4. Both solutions exhibit shear-thinning behavior, which is expected for liquid crystalline solutions (Donald and Windle 1992; Kojic, Bico et al. 2006). HPC is a well-known liquid crystal, and silk has been shown to exhibit liquid crystalline phases (Kerkam, Viney et al. 1991; Vollrath and Knight 2001). Because the solutions are non-Newtonian, it is not straightforward to match their viscosities. The wall shear rate in a tube ($\dot{\gamma}_{wall}$) can be calculated by,

$$\dot{\gamma}_{wall} = \frac{32Q}{\pi D^3}.$$

For the exit capillary in this system (D = 840 μm) and a flow rate (Q) of 3 mL/hr, the wall shear is ~14 /s. For a flow rate of 9 mL/hr, the wall shear rate is 43 /s. Therefore, we focused our matching attempts on viscosities within $O(10)$, which led to the use of 15 wt.-% HPC-MeOH. However, Cubaud and Mason showed that viscosities of miscible solutions need only be matched within a ratio of 15 to eliminate viscous folding (Cubaud and Mason 2006), which sufficiently covers the range of viscosities likely exhibited in the device.

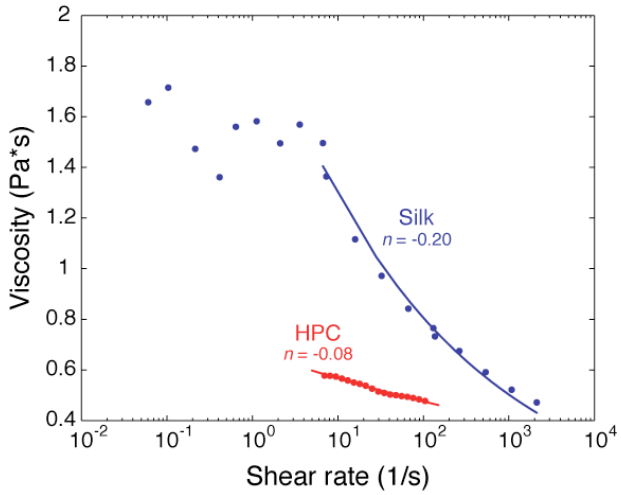

Figure 4. Shear-rate dependent measurements of ~25% concentrated RSF solution and 15 wt.-% HPC-MeOH solution. The shear thinning behavior of both curves is fit to a power-law model for viscosity (η) whereby $\eta = K(\dot{\gamma})^n$. K is the flow consistency index and n is the flow behavior index, indicative of the type of fluid. Both silk and HPC solutions are shear thinning fluids, with silk being much more strongly shear thinning. (K_{silk} = 2.07 Pa*s, K_{HPC} = 0.675 Pa*s).

b. Device Operation

We observed two regimes of our system: (1) flow focusing, wherein the formed silk fiber was reeled at a speed equal to or less than the velocity at which it was extruded (Figure 5a), and (2) drawing, wherein the reeling speed was greater than the silk extrusion velocity and the silk solution underwent extension during the spinning process (Figure 5b).

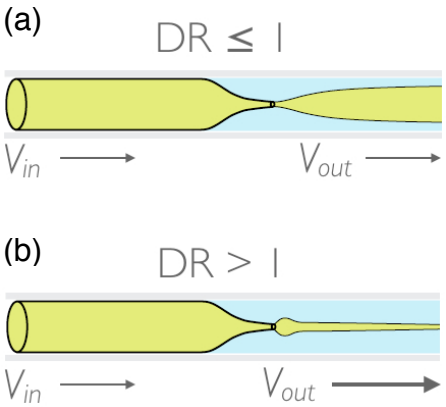

Figure 5. Two spinning regimes observed in the device. The draw ratio (*DR*) is defined by the ratio of the linear velocity of the fiber reeling (V_{out}) to the linear velocity of flow stream (V_{in}). (a) Flow focusing, $DR \leq 1$, the silk co-flows with the coagulant solution. (b)

Drawing, $DR > 1$, coagulant flows adjacently to the silk but the silk flow is dominated by the reeling speed of the fiber.

Figure 6a shows an image of the system flow focusing silk. In this regime, and with hydrodynamic focusing in general, the width of the central stream can be controlled by the relative flow rates of the outer and inner solutions (Q_{outer}/Q_{inner}, Figure 6b). This is expected based on a balance of volumetric flow rates, for which the laminar flow of concentric streams results in,

$$D_{inner} = D_{outer}\left[1 - \left(\frac{Q_{outer}}{Q_{inner} + Q_{outer}}\right)^{1/2}\right]^{1/2}$$

where D_{inner} and D_{outer} are the diameters of the inner and outer streams, respectively. Our data follows this curve qualitatively, but the values do not match quantitatively. This is a result of the significant amount of die swell at the inner capillary exit, as can be seen in Figure 6a, which causes the final volumetric flow rate of the silk stream to be unknown. Die swell is a common phenomena in polymer processing, whereby an extruded polymer solution undergoes swelling at the exit of an extrusion die due to polymer molecules partially recovering their relaxed conformation when suddenly being exposed to ambient pressures. This behavior has not been seen in other comparable microfluidic systems used to form fibers, likely because of their use of extremely dilute and low molecular weight polymers (Shin, Park et al. 2007).

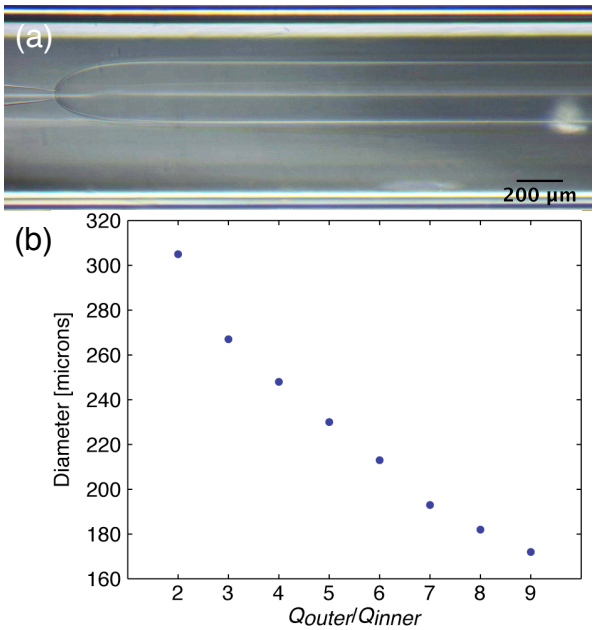

Figure 6. Device operation in the "flow focusing" regime. (a) Image of the device operating at $Q_{outer}/Q_{inner} = 3$. Silk is coming out of the pipette tip visible on the left, and flowing to the right. Note the die swell of the silk stream. (b) Change in diameter of the silk stream as a function of flow rate ratio.

In the drawing regime, a motorized spool was used to rapidly reel up the fibers at rates upward of ~5 cm/s. In this regime, stream diameter was only affected by reeling rate, but the system was too unstable (requiring constant speed adjustments) to collect quantitative data. As schematized in Figure 5, when drawing, the silk stream exhibits a small amount of die swell before being rapidly drawn down into a fiber. This is a standard occurrence when extruding and drawing highly extensible polymer solutions (Denn 1980). A draw down taper is also seen in the spider and silkworm silk gland, but because it occurs within the gland, the solution does not exhibit any die well (Knight and Vollrath 1999).

c. Resultant Fibers

Non-concentrated silk solution did not produce a fiber in our device, but rather led to the formation of large, opaque silk aggregates that simply dispersed into the coagulant. Unfortunately, the silk fibers produced in our device were too brittle to measure their mechanical properties, as has been the case for reconstituted silk fibers spun from other devices (Martel, Burghammer et al. 2008). Although secondary drawing of silk fibers has been shown to improve their mechanical properties (Zhou, Shao et al. 2009), fibers spun in the extensional regime of our device were still too brittle for testing. We largely attribute the extremely poor mechanical properties of our fibers to the unnatural properties of the silk spinning solution. The rheological properties of reconstituted silkworm silk solution have been shown to be dramatically different from that of native silk solution (Holland, Terry et al. 2007), and degradation of the molecular structure of reconstituted silk has been attributed to the extensive boiling performed to remove the sericin coat (discussed below) (Yamada, Nakao et al. 2001; Jiang, Liu et al. 2006).

We were able to collect and manipulate some fibers spun from the drawing regime of our device (Figure 7). These fibers were initially quite elastic, but dried within 10 min and became too brittle to handle. This suggests that proper hydration of the fibers is essential for their extensibility and that the sericin coating on native fibers (thought to assist in water retention) could be an essential component to maintaining the fiber mechanical properties.

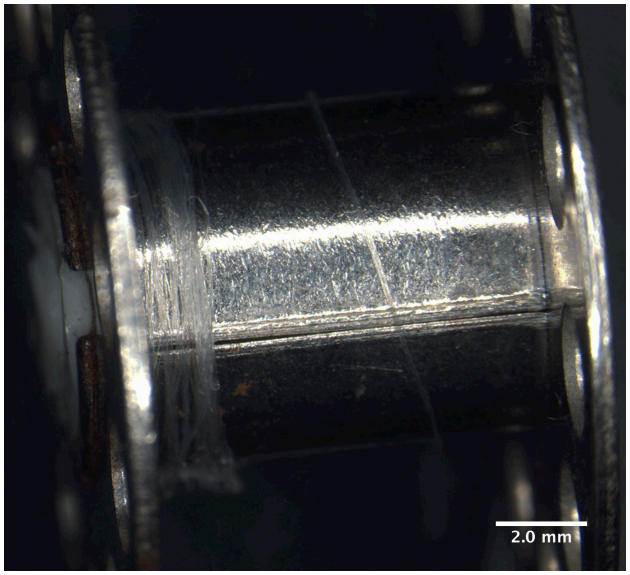

Figure 7. A spool of silk fiber reeled from the device in the drawing regime. The fibers dry rapidly and become too brittle to remove from the spool without shattering.

A single fiber is shown in Figure 8. The fiber is optically transparent, and exhibits an unexpected and subtle banding pattern perpendicularly to the fiber axis. It is unclear what causes this pattern, as the primary forces in the spinning process are tensile.

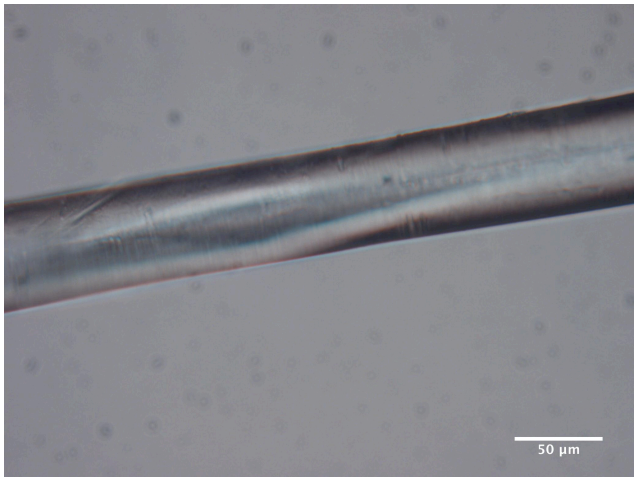

Figure 8. A single silk fiber spun from the device in the drawing regime.

X-ray diffraction data of these fibers indicate that they have significant molecular alignment and are composed of *β*-sheet crystallites. The drawn fibers exhibit molecular alignment along the fiber axis, although not as much alignment as native cocoon fibers (Figure 9a). Interestingly, other work using hydrodynamic focusing of RSF in a similar glass-capillary device that did not involve any drawing of the fibers showed no molecular orientation in the resultant fibers (Martel, Burghammer et al. 2008; Martel, Burghammer et al. 2008). This suggests that the drawdown process is a contributor to molecular orientation in silk fibers, as has also been suggested from studies of the *in vivo* spinning

system (Lefevre, Boudreault et al. 2008). The β-sheet crystallite content of the drawn fiber is significantly larger than that of the native fiber (Figure 9b), likely due to the use of methanol as a coagulant, which strongly induces β-sheet formation.

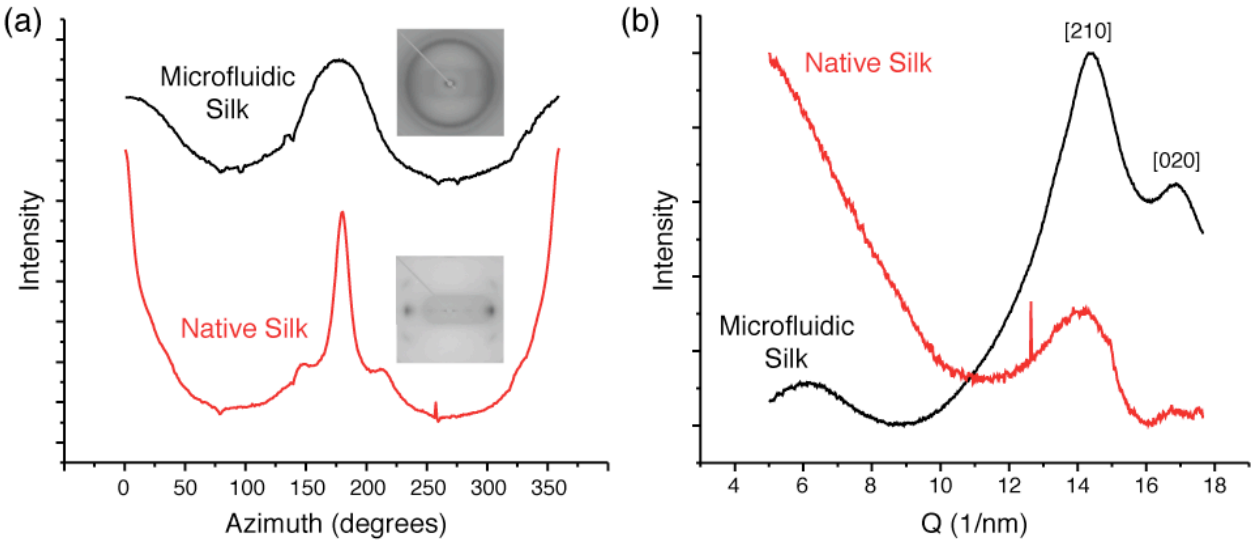

Figure 9. Fiber diffraction results for an artificial fiber and a natural cocoon fiber. (a) Azimuthal profiles of the diffraction patterns. The widths of the center peaks represent molecular alignment, with skinnier peaks indicating a higher degree of molecular alignment. (b) Radial profiles of the diffraction patterns. The [210] peak indicates that the fiber has a high β-sheet content, with the [020] peak indicating that the β-sheets have folded into crystallites. The data for native silk is not as smooth because fewer fibers were used in the experiment.

d. Irreproducibility of Results

It has recently become apparent that the dissolution process for making RSF significantly degrades the protein (Yamada, Nakao et al. 2001; Holland, Terry et al. 2007). Particularly, degumming (boiling) time can diminish fiber mechanical properties (Perez-Rigueiro, Elices et al. 2002) and decrease the molecular weight of the final protein in solution (Yamada, Nakao et al. 2001). In addition, any residual sericin due to incomplete degumming can have a strong effect on RSF, including decreasing solubility and increasing crystallization rates (Ki, Um et al. 2009). Therefore, making RSF involves a difficult attempt to straddle the threshold between under- and over-degumming the silk. We found the batch-to-batch variability of RSF to be so large that it was impossible to consistently reproduce results. Most notably, the extensional behavior of the solution varied greatly and it was often not possible to draw down and reel fibers.

3.5 Summary

We have demonstrated a microfluidic system for the axisymmetric hydrodynamic focusing of concentrated silk protein for the spinning of silk fibers. This required the

viscosification of coagulant solutions to minimize flow instabilities. We demonstrated two regimes of the system, wherein fibers could be formed from flow focusing or drawing. Due to the highly unstable and irreproducible nature of the source silk solution, it was difficult to consistently reel fibers. Of the fibers that were produced, drying had a significant effect on their mechanical properties, suggesting that a moisture retaining coating layer could be important for maintaining fiber hydration. These fibers, from the drawing regime of the system, also exhibited a high degree of molecular alignment, suggesting that the draw down of the spinning solution is important for orienting molecules along the fiber axis. However, when drawing fibers from the system, the effect of hydrodynamic focusing becomes negligible and the system acts primarily like a wet spinning extrusion die. Thus the utility of such a system is questionable for highly elastic solutions. For lower concentration RSF solutions, which would likely be much more stable, consistent, and have significantly less extensional behavior than high concentration RSF, the system could prove to be useful for making fibers and using flow rates as a simple means of adjusting fiber diameter.

3.6 Acknowledgement

We thank Dr. Anne Martel at Stanford Linear Accelerator Laboratory for assistance with X-ray diffraction measurements. This research was partially supported by an NDSEG Graduate Fellowship to D.N.B. and University of California Systemwide Biotechnology Research & Education Program GREAT Training Grant 2008-02.

Chapter 4. A Biomimetic Microfluidic Silk Gland

4.1 Abstract

We have developed a biomimetic microfluidic silk gland with the goal of spinning native quality spider and silkworm silk fibers. Whereas there have been a number of attempts to spin silk fibers, none of them have resulted in fibers with mechanical properties comparable to those produced naturally. Most of these spinning methodologies require high temperatures and pressures, and harsh solvents. In contrast, silk spinning in the spider and silkworm is a benign process. In fact, within the spider and silkworm, fiber formation is a carefully and dynamically controlled process involving complex fluid dynamics and biochemistry. We believe that by replicating the complexity of the *in vivo* silk gland, we will be able to spin silk fibers that have comparable mechanical properties to those that are naturally spun. To this end, we have developed a method of making a microfluidic system that captures the geometrical features of the silk gland, and out of porous material-- allowing mass transport into and out of the silk solution during flow, as in the actual silk gland. We furthermore demonstrate that this system can be constructed with different hydrophobicities and that is can be used to alter the pH of a solution flowed through it.

4.2 Introduction

Due to their exceptional mechanical properties and the fact that they are produced under ambient conditions, there has been a significant amount of research effort toward understanding how spiders and silkworms spin silk fibers (Vollrath and Knight 2001). Most industrial fiber spinning efforts involve extremely high temperatures and pressures, as well as hazardous solvents. Spider and silkworm silk, on the other hand, is spun at room temperature, low pressures, and uses only water as a solvent. Despite years of research, it is still poorly understood how the *in vivo* silk spinning process works so efficiently to produce such impressive fibers, yet the mechanisms of action that produce the fibers are fairly well characterized (Vollrath and Knight 2001). Briefly and simplistically, high concentrations of silk protein in an aqueous bath are exposed to shear and elongational flow fields as they move down the silk duct-- stretching and aligning the protein molecules-- while they are simultaneously exposed to ionic gradients that regulate the liquid-solid phase transition of the protein. Eventually the silk solution solidifies sufficiently to detach from the gland walls into a fiber, and excess solvent is further driven out of the fiber for the organism to reabsorb (Figure 1a). Whereas the effects of stress, concentration, and ionic content of silk solutions have been studied, this knowledge has not been collectively leveraged for use in spinning silk fibers in a “biomimetic” fashion (Vollrath 2000). Rather, most spinning attempts have relied on industrial techniques whereby silk solution is forced through a small hole (“extruded”) and none of these attempts have been able to form native-quality fibers (Liivak, Blye et al. 1998; Vollrath 2000; Lazaris, Arcidiacono et al. 2002; Teule, Cooper et al. 2009). A major roadblock toward the creation of a biomimetic spinning system has

been the inability to fabricate fluidic structures on the same size scale as the silk gland (10-100 μm in a large spider). Capitalizing on the latest advances in microfabrication and microfluidics, we have developed a biomimetic microfluidic silk gland. The system described herein captures the geometrical features of the native silk gland, and is capable of mass transport into and out of the silk solution during flow (for mimicking ionic gradients, Figure 1b). We demonstrate our initial attempts to fabricate this system, and an improved fabrication scheme that minimizes structural defects. We show that this system can be fabricated with different polymers to alter the surface properties of the channel if needed (the surface chemistry inside the silk gland is unknown). Lastly, we demonstrate that the system can be used to alter the pH of a solution flowing through it, just as the silk gland alters the pH of silk solution during flow.

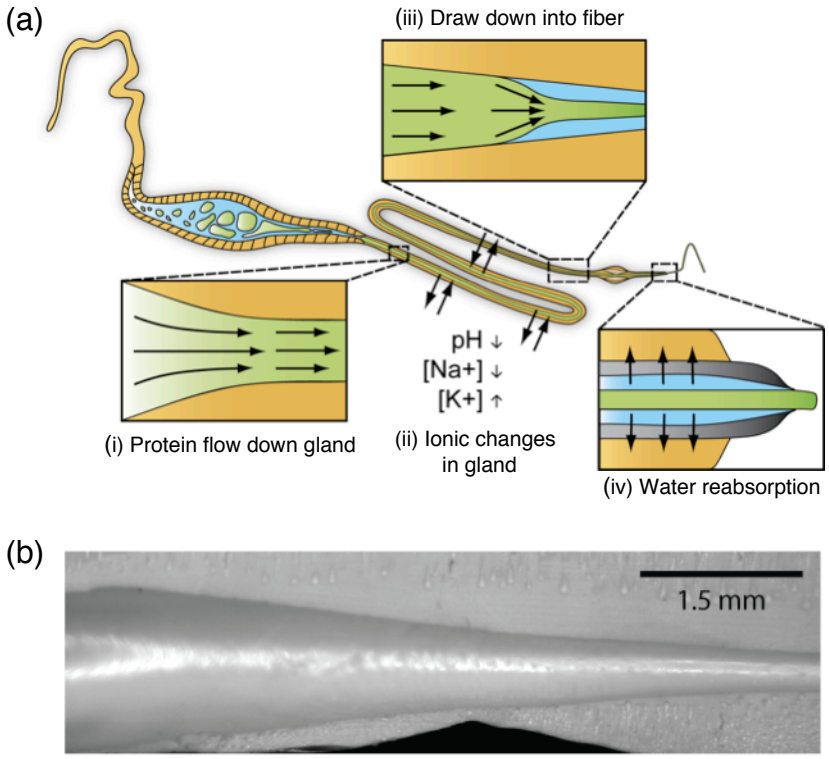

Figure 1. Schematic of fiber formation in the silk gland and a biomimetic microfluidic device. (a) Protein flow and ionic changes in the silk gland. Silk dope moves through a long and contracting funnel geometry (i) while simultaneously being exposed to ionic gradients that regulate crystallization (ii). Upon sufficient solidification, the fiber draws down from the wall (iii) and the aqueous solvent is reabsorbed by the organism (iv). (b) Lengthwise cross section of a porous channel designed to emulate the functionality of the silk gland (discussed in detail below).

4.3 Experimental

a. Device Fabrication

Devices were fabricated using Phase Separation Micromolding (Vogelaar, Barsema et al. 2003; Vogelaar, Lammertink et al. 2005), whereby a polymer/solvent solution is cast on a microstructured surface and submerged in a non-solvent bath to induce phase separation and polymer solidification. The resultant polymer film is porous, and retains the molded microstructure features. Herein, we primarily employed two polymer/solvent systems: 19 wt.-% polyetherimide/n-methyl-2-pyrrolidone (PEI/NMP) and 23 wt.-% poly(methyl methacrylate)/n-methyl-2-pyrrolidone (PMMA/NMP). Non-solvents were either tap water or 100% methanol.

Briefly, glass capillaries were pulled using a Sutter P30T pipette puller customized to have a maximized pulling distance. A pulled glass capillary was mounted in a U-shaped holder which was then filled with the chosen polymer solution and subsequently left in a non-solvent bath for at least 24 hr. The pulled glass capillary was then removed from the solidified polymer mold, and the mold was left to dry (Figure 2).

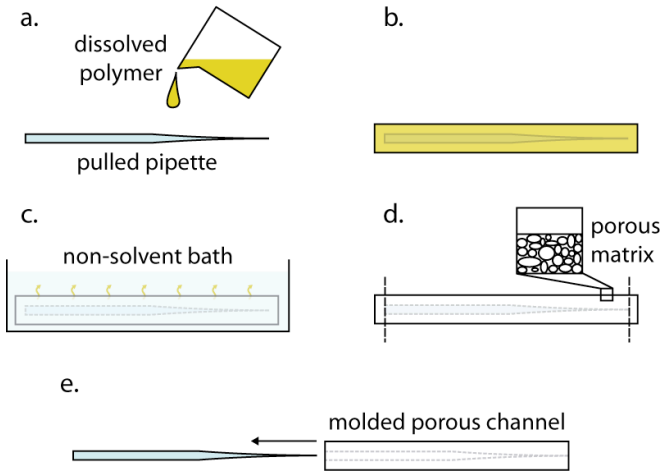

Figure 2. Process for making porous channels. (a) A pulled pipette is covered in a polymer solution. (b) The capillary-polymer system is in a U-shape container in order to hold the solution. (c) The system is then inserted in a non-solvent bath, driving out the polymer solvent and solidifying the polymer. (d) The resultant solid structure is porous. The ends are cut so that the glass capillary can be removed as in (e).

b. Device Imaging and Mass Transport Characterization

Samples were cut with fresh razor blades. All micrographs were taken on a Hitachi TM-1000 Scanning Electron Microscope (SEM). This SEM does not require any metal coating on samples.

To characterize mass transport in the porous channel, a device of ~2 cm in length with a 1.5/2.25 mm ID/OD was chosen as a model system. Tubing was fit to the ends of the porous channel such that the exposed length was 2 cm. A polydimethylsiloxane (PDMS) mount was made to hold the device and allow for separate control of core and sheath flow (Figure 3). PDMS (Sylgard 184, Dow Corning) structures were made by mixing 10:1 base to curing agent, casting the mixture over a

square metal rod, and curing at 60°C. The rod was chosen in size such that the tubing connected to the porous channel fit tightly inside the PDMS mold, keeping the porous channel axially centered. After the PDMS had cured, the metal rod was removed and access holes for the sheath flow were punched. The porous channel/tubing was slid into the PDMS mount, and the edges of the PDMS were sealed with silicon sealant.

For mass transport experiments, 10 mM phosphate buffer at pH 5.2 and pH 10.6 were prepared. pH 10.6 buffer was used as the core solution (inside the porous device) and pH 5.2 buffer as the sheath solution (outside the porous device). All pH measurements were performed using a Denver Instrument UB-5 pH meter.

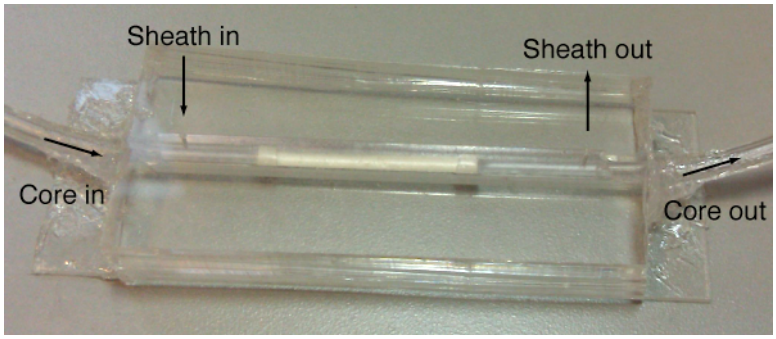

Figure 3. Mounting scheme for a piece of porous device. The porous device is connected to tubing at each end, and then slid into a larger PDMS channel. The ends of the PDMS channel are sealed, and holes are punched to allow input and output of a sheath flow.

c. Contact Angle Measurements

Polymer solutions were cast as thin films on glass slides, and allowed to undergo phase separation as described above. A Kruss Contact Angle Measurement System was used to measure the static contact angle of water on the films. Contact angles were calculated by the system software using the Tangent 1 algorithm. Four measurements were performed per film. Statistical significance was determined from an unpaired Student's *t*-test.

4.4 Results

a. Fabricating a Biomimetic Microfluidic Channel

Most microfluidic systems have a rectangular cross-section, due to the nature of microfabrication processes. There have been a few efforts to fabricate circular cross section channels mainly to make microfluidic devices that mimic vasculature (Borenstein, Tupper et al. 2010). These efforts have largely utilized surface tension to create channel curvature, though thermal reflow (Seo, Bae et al. 2004; Wong, Agarwal et al. 2007) or filling the channels with additional coatings (Abate, Lee et al. 2008; Fiddes, Raz et al. 2010). None of the these methods can easily make a circular cross

section with smoothly varying cross sectional area along their length. To create a straight and circular cross section channel with controlled shape, one possibility is molding over an etched glass rod. The rod can be initially etched the desired profile by drawing it out of a hydrofluoric acid (HFA) bath with varying rates. This etching procedure has been performed to create custom shape fiber optic tips (Haber, Schaller et al. 2004). We briefly explored this methodology, but abandoned it due to the difficulties of working with HFA. Rather, we found that pulled glass capillaries would create a contraction shape similar to that of the silk gland. However, to pull the capillary to a length comparable to that of the silk gland (~2 cm), we had a pipette puller custom designed to maximize its pulling length. The resultant capillaries are shown in Figure 4. Molding over these capillaries creates a circular cross section and contracting microfluidic channel geometry.

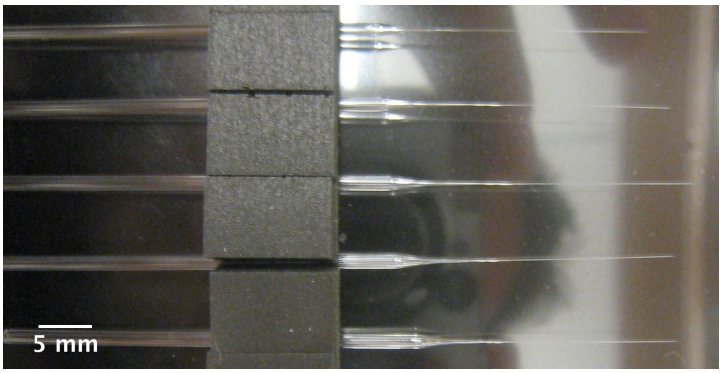

Figure 4. Glass capillaries pulled with a pipette puller modified to allow for longer pulling lengths.

To enable the mass transport into and out of our fluidic channel as in the silk gland, the molding material of choice must have a large enough porosity to allow the diffusion of water and ions. “Phase separation” is a common process for producing porous membranes of all types, whereby a polymer/solvent combination is cast into a film and then placed in a non-solvent bath (Vogelaar, Barsema et al. 2003). The solvent is driven out of the polymer/solvent system because the thermodynamic equilibrium of the system is disturbed, and the polymer phase solidifies. Depending on the polymer/solvent/non-solvent combination and other parameters therein (e.g. concentration), characteristics of the membrane, such as pore size, can be controlled. Recently, it has been shown that membranes fabricated with phase separation can be initially cast on microfabricated masters to replicate the microstructures (Vogelaar, Barsema et al. 2003). We leveraged this process by casting polymer solution over our pulled glass capillaries to fabricate porous, circular cross section, and contracting microfluidic channels out of different polymers (Figure 5). These channels form the basis for a biomimetic microfluidic silk gland.

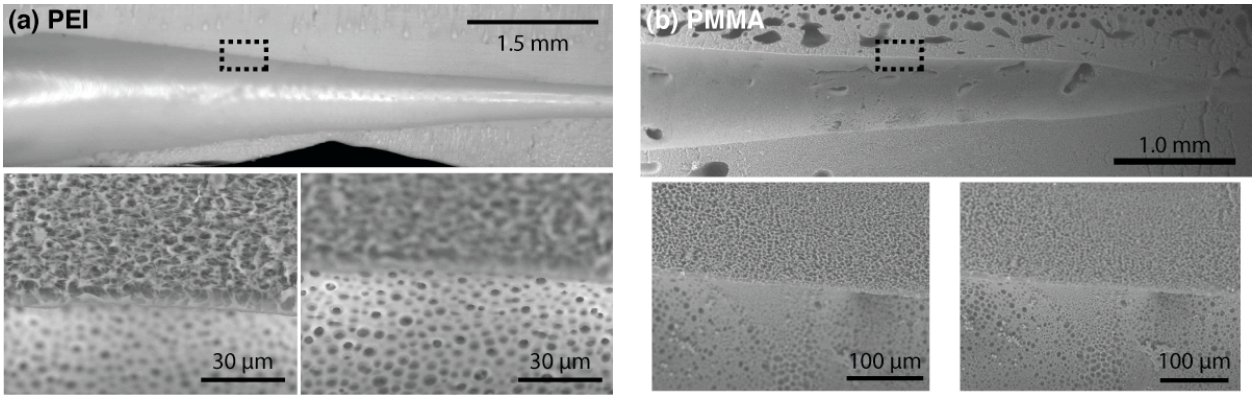

Figure 5. Two different biomimetic silk gland devices fabricated with different polymers. Bottom panels are magnified views of the porous network focused on the plane of the cross section (left) and the wall of the channel (right). (a) Device made from 19 wt.-% PEI/NMP, coagulated in a water bath. (b) Device made from 23 wt.-% PMMA/NMP, coagulated in a water bath.

b. Choice of Polymer System

Because the phase separation process is compatible with almost any polymer that has a suitable solvent/non-solvent pair, there is a wide parameter space to explore for the creation of this device. Particularly, it is unknown if there is an effect of surface properties within the silk gland (e.g. hydrophobicity) on silk spinning. Therefore, we tested polymers with different hydrophobicities for the creation of these devices. Figure 5a shows a device made of PEI, and Figure 5b shows a device made of PMMA. We furthermore measured the contact angles of membranes of each of these polymers (Figure 6) and found PEI to be more hydrophobic than PMMA (water contact angles of 92° ± 4° and 77° ± 5°, respectively. $P<0.01$). We chose to continue using PEI for device fabrication because of its wider range of chemical compatibility, specifically with alcohol solvents that are well-established coagulants of silk.

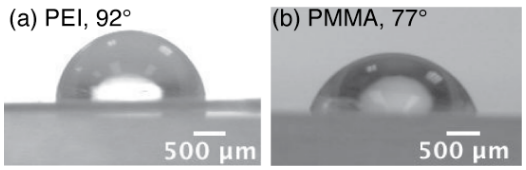

Figure 6. Contact angles of water on porous (a) PEI and (b) PMMA films.

c. Improvement of Fabrication

As can be seen in Figure 5, there are significant structural irregularities in the porous device. Mainly, there are a significant number of “macrovoids”-- large empty pockets in the porous network. The formation of macrovoids is known to be dependent on polymer concentration, additives in the polymer, film thickness, and the strength of the solvent/non-solvent combination (Boom, Wienk et al. 1992; Smolders, Reuvers et al. 1992; Vogrin, Stropnik et al. 2002; Li, Chung et al. 2004; Peng, Chung et al. 2008).

They can cause structural weakness as well as irregular local diffusion profiles in a porous network. We attempted to eliminate macrovoids by increased the PEI/NMP concentration to 30 wt.-%, without success. Utilizing the fact that PDMS swells in methanol and absorbs it, we created a PDMS holder for the capillary-polymer solution system that both minimizes the polymer film thickness and allows for axisymmetric phase separation (Figure 7). Furthermore, having a circular cross section, rod-like device should create an axisymmetric diffusion profile into the channel.

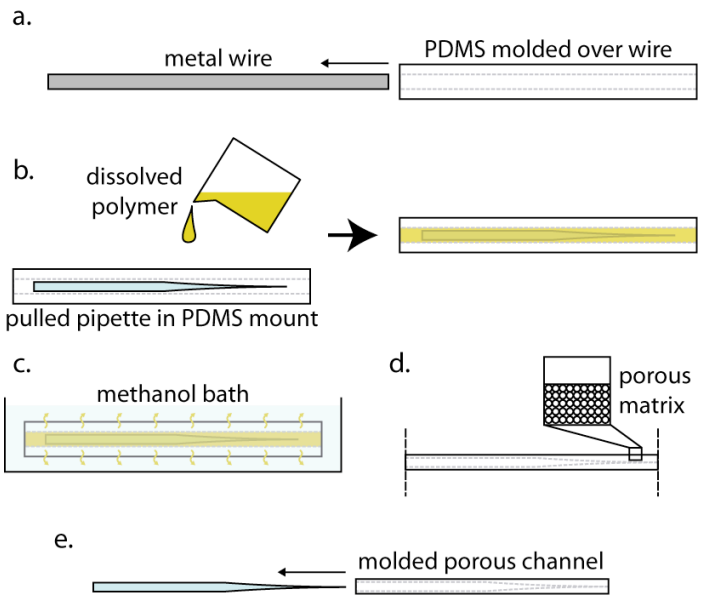

Figure 7. Schematic for fabrication method for making a thin-walled, circular device. (a) PDMS is molded over a metal wire that has a slightly larger outer diameter than the glass capillary. (b) The pulled capillary is inserted into the PDMS mount and the PDMS is then filled with polymer solution. (c) The system is allowed to undergo phase separation for a week in a methanol bath. (d) The resultant porous solid is removed from the PDMS and cut at the ends to allow removal of the pipette, as in (e).

We found that with this system, complete phase separation could take upward of one week. The resultant devices showed almost no macrovoids, and a largely uniform pore structure (Figure 8). The device shown has a maximum wall thickness of ~0.75 mm. Making devices with thicker walls caused several macrovoids to appear.

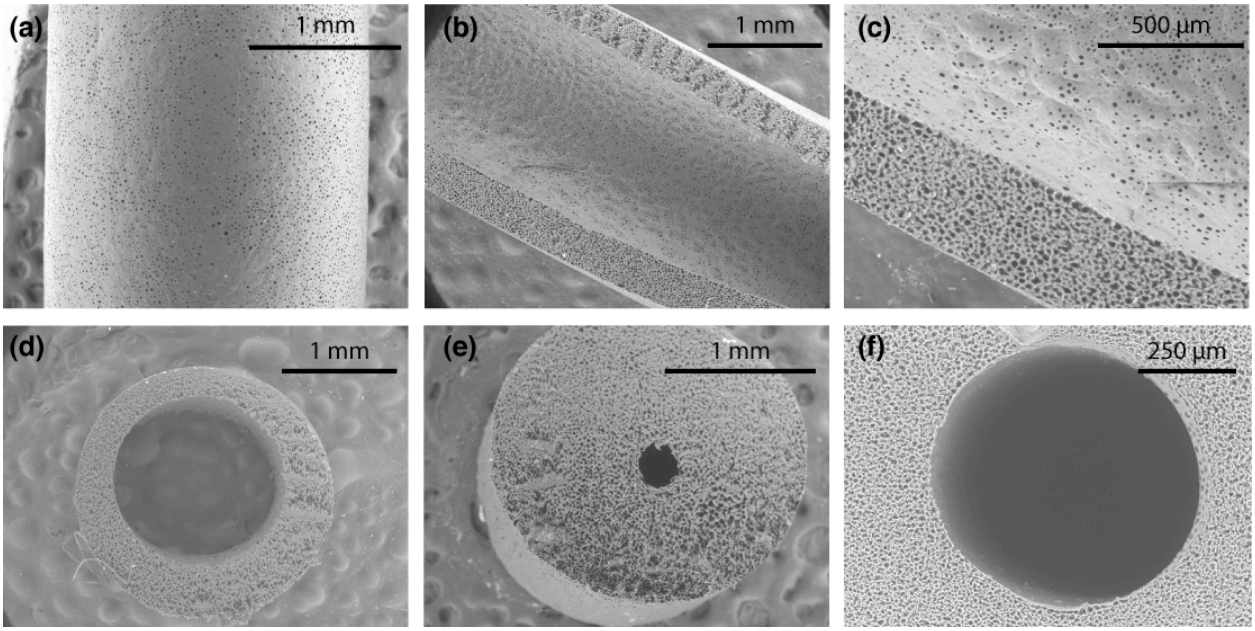

Figure 8. Circular device made with the new fabrication scheme (19 wt.-% PEI/NMP, MeOH coagulant). (a) Top view of outside of device. (b) Longitudinal cross section. Striations are due the use of a blade to cut the device. Apparent variations in wall thickness are due to difficulties in cutting the device exactly through its middle. (c) Higher magnification of longitudinal cross section. Surface roughness on the inside of the device is due to roughness on the glass capillary from silanization. (d) Axial cross section of the device. Note that it is difficult to perfectly center the glass capillary. (e) Axial cross section further down the length of the device, showing the decrease in the channel diameter. (f) Higher magnification image of an axial cross section.

d. Mass Transport in the Device

One of the most critical chemical changes in both the spider and silkworm glands is the drop in pH along the gland length, which induces crystallization in the silk protein. We therefore tested the ability to alter the pH of a solution flowing through our porous channel. pH 10.6 and pH 5.2 solutions were used for the core and sheath flows, respectively. Figure 9a shows that the change in pH of the core solution is almost entirely dependent on the core flow rate, suggesting it is a function of residence time in the porous channel. We note that there was no difference in expected output volume for either the core or sheath flows for any of the flow rate combinations tested, indicating that there was minimal or no water transport across the device walls.

Assuming the differences in pH across sheath flow rates are within experimental error, we averaged these values and plotted the effect of residence time on $[H^+]$ in the core solution (Figure 9b). pH is converted to a linear scale and normalized to the initial core pH (10.6). Whereas the relationship between concentration and residence time can be almost equally well fit to a linear (R^2 = 0.9955) or exponential curve (R^2 = 0.9895), an analytical mathematical approximation to this problem (discussed below) indicates the

relationship should be exponential. Therefore we fit an exponential curve to the data in Figure 9b.

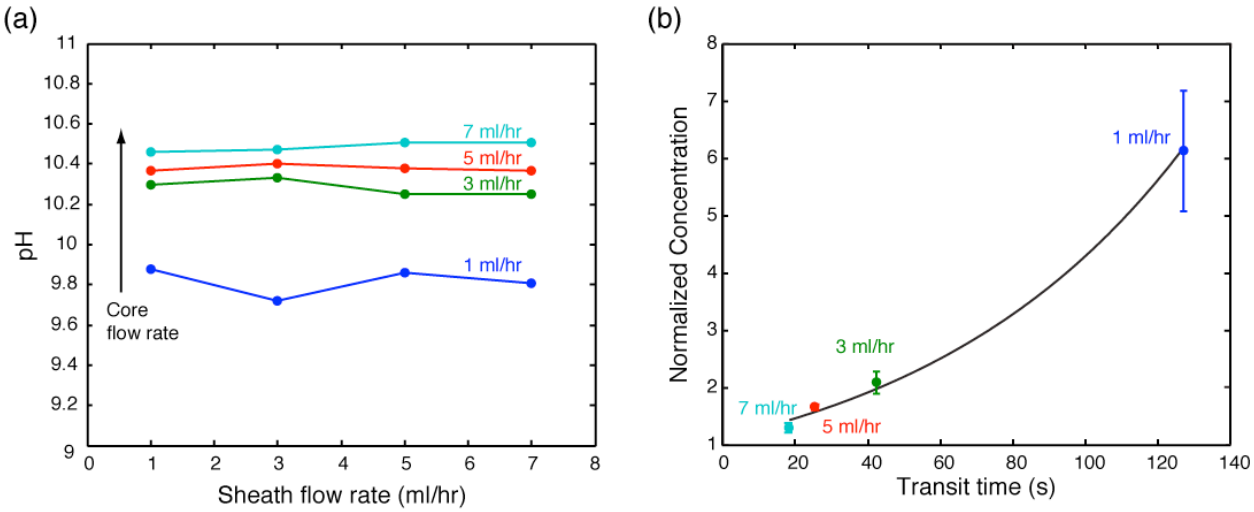

Figure 9. Effect of sheath and core flow rate on the pH of the core solution out of the device. (a) The sheath flow reduces the pH of the core solution, but the effect is independent of sheath flow rate. (b) Effect of residence time in the device on H^+ concentration in the core solution, normalized to initial concentration. Color-coding corresponds to that in (a). Error bars indicate standard deviations (n=4). Black line is an exponential fit of the data (R^2 = 0.9895, y=1.1137*exp[0.0135*x]).

This system can be analyzed with more mathematical rigor as a Graetz-type problem with prescribed wall flux. The Graetz problem specifically models the transport of energy (or mass, in this case) in fully developed, laminar pipe flow. Deen provides the solution to this problem for a tube made of a porous membrane, with a constant concentration sheath flow around it (Deen 1998). Assuming that the core flow is fully developed, the membrane permeability does not vary with position, and neglecting axial diffusion, the solution to the problem is,

$$\frac{C_{core}(z) - C_{sheath}}{C_{core,i} - C_{sheath}} = \exp\left[-k\frac{2z}{RU}\right]$$

where $C_{core}(z)$ is the velocity-averaged core concentration as a function of longitudinal position (z), $C_{core,i}$ is the initial core concentration, C_{sheath} is the sheath concentration, k is the bulk mass transfer coefficient for the system, R is the tube radius, and U is the average velocity. Given that we are sampling the pH of the core solution at the outlet of the device, z = 2 cm for all experimental data points. Furthermore, the average velocity can be expressed in terms of residence time ($U = z/t_r$, where t_r is residence time), leading to the expression,

$$\frac{C_{core}(t_r) - C_{sheath}}{C_{core,i} - C_{sheath}} = \exp\left[-k\frac{2t_r}{R}\right].$$

We fit this expression to the data in Figure 9b, with core flow concentration expressed in absolute terms (Figure 10), allowing for the determination of the mass transfer coefficient for the system (k = 5.625e-11 m/s, R^2 = 0.96). The primary caveat is that the derivation here assumes that the sheath flow rate is sufficiently large that C_{sheath} and k are essentially constant along the length of the device. Even at the highest flow rate tested (7 ml/hr), we measured an increase in pH (a decrease in H^+ concentration) in the sheath solution. However, knowing the mass transfer coefficient and knowing that the analytical solution fits well to the experimental system will allow for use of this approximate solution in understanding system behavior and designing it for specific parameters (such as gradient shape).

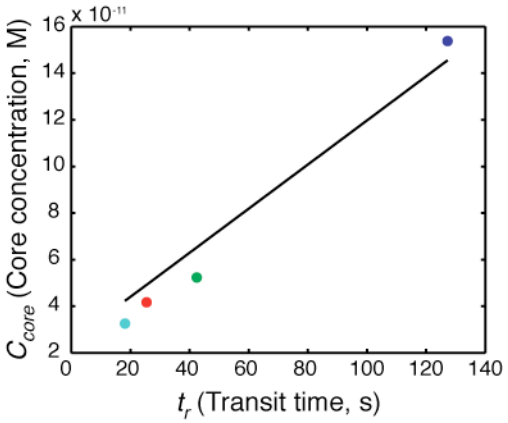

Figure 10. Effect of residence time in the device on H^+ concentration in the core solution and a fit of the solution to the Graetz problem for this device. Color-coding corresponds to that in Figure 9. The black line is a fit of the expression $C_{core} = (C_{core,i} - C_{sheath})*\exp(-k*2t_r/R) + C_{sheath}$, where k is the unknown coefficient.

4.5 Discussion and Future Work

We have developed a microfluidic channel that can mimic the functionality of the silk gland by having similar geometrical characteristics as the silk gland (circular cross section, contracting shape) and by allowing mass transport into and out of the flow channel to mimic the ionic gradients in the gland. We have demonstrated that this biomimetic microfluidic silk gland can be made with different surface properties, and can successfully be used to alter the pH of solutions flowed through it. Future work will entail the characterization of ion transport through the device at various flow rates, and the ability to extract water from the core solution.

We unsuccessfully attempted to use this device to spin silk fibers from reconstituted silkworm fibroin (RSF), with methanol as a coagulant. We believe the lack of success was largely due to the use of RSF, which is a significantly degraded protein and acts very differently from native silk (in particular, it has to be extruded and cannot be drawn). Future testing of the device will use native dope excised from silk glands (see Appendix C) or, depending on the progress of genetic engineering technologies, a

recombinant source of native quality spider silk protein. When the problem of finding a source of silk protein is solved, this device will provide a unique platform for testing a wide variety of biomimetic spinning conditions and also assist in the artificial production of spider silk fibers with native-like mechanical properties.

4.6 Acknowledgement

Contact angle measurements were performed by Frank Myers in the UC Berkeley Microfabrication Laboratory. This research was partially supported by an NDSEG Graduate Fellowship to D.N.B. and University of California Systemwide Biotechnology Research & Education Program GREAT Training Grant 2008-02.

Chapter 5. Generation of Monodisperse Silk Microspheres Prepared with Microfluidics

5.1 Abstract

Monodisperse microspheres of reconstituted silkworm cocoon silk were produced using a glass capillary-based microfluidic system and by identifying an appropriate solvent/non-solvent fluid system. The microspheres can be produced to a range of different diameters depending on the system flow rates, and have a nearly homogeneous size distribution. The silk microspheres exhibit a unique core-shell architecture, and have a largely *β*-sheet structure as measured by infrared spectroscopy. Mechanical characterization was performed with AFM nanoindentation and indicates that the microspheres are unexpectedly soft for a silk material. Because silk is well established as biocompatible and biodegradable, we anticipate that these silk microspheres could have particular utility in drug delivery and controlled release.

5.2 Introduction

Silk fibroin is a protein that is naturally produced in insects and spiders that assembles into *β*-sheet structures when spun into fibers. These fibers display exceptional mechanical properties, and have been long used in textiles and even medical sutures because of their biocompatibility and biodegradability. The cocoons of the *Bombyx Mori* silkworm provide an abundant source of fibroin protein, which has seen a surge of research as a structural scaffold in tissue engineering and a platform for drug delivery (Altman, Diaz et al. 2003). Specifically, silk microspheres have been demonstrated to have beneficial characteristics for drug delivery and controlled release because of their mechanical stability, mild processing conditions, high drug encapsulation efficiency, long term sustained release, and slow degradability (Wang, Wenk et al. 2007; Wang, Wenk et al. 2007; Wenk, Wandrey et al. 2008). In general, polymeric microspheres have become strong candidates for use in drug delivery because of their ease of delivery and the ability to regulate their drug release kinetics (Sinha and Trehan 2003; Freiberg and Zhu 2004). Common microparticle production techniques, however, create particles with a large size distribution because of the inhomogeneous forces involved (Xu, Hashimoto et al. 2009). For example, methods used to produce silkworm silk spheres have consisted of emulsification (Xie, Wu et al. 2008), spray drying (Yeo, Lee et al. 2003; Zhou, Peng et al. 2008), laminar jet breakup (Wenk, Wandrey et al. 2008), lipid templating (Wang, Wenk et al. 2007), and self-assembly (Cao, Chen et al. 2007). In addition, recombinant spider silk-mimetic peptides have been used to create microspheres (Lammel, Schwab et al. 2008) and microcapsules (Hermanson, Huemmerich et al. 2007). Whereas all of these techniques are effective at producing nano- to micro-scale particles, the particle size distribution is generally very broad.

Narrowing this particle size distribution has been shown to be important in controlling drug release kinetics, reproducibility, and bio-availability (different size particles accumulate differentially in the body) (Wang, Ma et al. 2005; Xu, Hashimoto et al. 2009). Recently, microfluidic methods have proven useful in the generation of monodisperse droplet suspensions (Thorsen, Roberts et al. 2001; Utada, Lorenceau et al. 2005). Taking advantage of the periodic and predictable breakup of immiscible co-

flowing streams, discrete and consistently sized droplets can be formed in a variety of microfluidic geometries. By using a polymer solution as the dispersed (droplet) phase, several groups have leveraged this technology to produce monodisperse polymeric microspheres (Utada, Chu et al. 2007; Zhang, Tumarkin et al. 2007; Shah, Kim et al. 2008). Herein, we demonstrate the first production of monodisperse reconstituted silkworm silk microspheres by leveraging microfluidics and identifying an appropriate solvent/non-solvent fluid system.

5.3 Experimental

a. Preparation of Silk Solution

Reconstituted silk solution was prepared as previously described (Nazarov, Jin et al. 2004). Briefly, *Bombyx Mori* silkworm cocoons (Tajima Shoji Co., Ltd., Yokohama, Japan) were boiled twice in 0.02 M Na_2CO_3 for 20 mins and rinsed in deionized water to remove sericin glue. The degummed silk was allowed to dry overnight, and was dissolved in 9.3 M LiBr for 4 h. The dissolved silk solution was then dialyzed with 3,500 MWCO cassettes (Pierce Biotechnology, Inc., Rockford, IL) against 2 L Milli-Q water for 48 h, changing the water regularly at least 6 times. The resultant ~8 wt.-% silk solution was filtered through a 100 µm mesh to remove large debris, and stored at 4 °C for no more than two months. Silk solution was passed through a 0.22 µm pore syringe filter immediately before use.

b. Microfluidic Device and Operation

Microfluidic devices were prepared by coupling glass capillaries (Utada, Lorenceau et al. 2005). A 0.58/1 mm ID/OD glass capillary (1B100, World Precision Instruments, Inc., Sarasota, FL) was pulled (P-97 micropipette puller, Sutter Instrument Company, Novato, CA) and broken to a ~60 µm ID tip. A second glass capillary of the same dimensions was heated against a bunsen burner flame to decrease the ID at the entrance to ~300 µm. Both capillaries were inserted into a 1 mm ID square glass capillary (8100, VitroCom, Inc., Mountain Lakes, NJ) to ensure axial alignment.

The dispersed phase consisted of reconstituted silk solution. The continuous phase was a mixture of 75 wt.-% oleic acid and 25 wt.-% methanol. 2 wt.-% Span-80 surfactant was added to the oleic acid to stabilize and inhibit coalescance of the droplets. The flow rate of the dispersed phase was fixed at 1 mL/hr, and the flow rate of the continous phase was varied from 6 mL/hr to 14 mL/hr. The outlet tubing was suspended in a round bottom flask containing at least 100 mL of methanol. Silk microspheres were left in this bath for at least 24 h to ensure complete crystallization. After 24 h, this bath was decanted and replaced with fresh methanol. Using ethanol or isopropanol in the outlet bath had no effect on microsphere morphology or FTIR spectra (data not shown).

c. Imaging

A high speed camera (Troubleshooter 1000MS, Fastec Imaging, San Diego, CA) was used to capture images of the forming drops. To measure microsphere polydispersity, suspensions of microspheres were pipetting onto a glass slide and the spheres were allowed to settle. Optical micrographs were captured with brightfield imaging. Diameters were measured for 50 microspheres. The polydispersity index was defined as the coefficient of variation of these measurements. Student's t-tests were used to compare the mean diameters from different suspensions. For SEM sample preparation, an aliquot of microsphere suspension was dropped onto a piece of silicon wafer that was pre-heated to 300˚C, "flash" evaporating the solvent. The sample was sputtered with gold and imaged on an environmental SEM (Philips XL30) operating at an accelerating voltage of 15 kV.

d. FTIR Spectroscopy

Attenuated total reflectance (ATR) FTIR spectra were recorded on a Nicolet 360 Avatar ESP spectrometer equipped with a DTGS KBr detector and the ATR accessory (Madison, WI). Spectra were recorded at 4 cm^{-1} resolution, and integrated over 256 scans. A silk film was prepared by dessicating silk solution in a Petri dish. For silk microspheres (Q_{outer}/Q_{inner} = 8, ~180 µm diameter), the sample was pipetted directly on to the ATR Germanium crystal and allowed to dry.

e. AFM Indentation

Indentation was performed with a Bioscope AFM (Veeco Metrology, Santa Barbara, CA). Cantilevers (10 pN/nm, 35° half angle, Veeco Metrology) were initially silanized with tridecafluoro-1,1,2,2-tetrahydrooctyl-1-trichloro-silane to minimize cantilever adhesion to the microspheres. Microspheres (Q_{outer}/Q_{inner} = 8, ~180 µm diameter) were allowed to settle on a glass slide, and the cantilever was positioned over a single sphere. The stage with the glass slide was raised at a constant rate, and the deflection of the cantilever was measured as a function of stage height. Indentation was performed for at least 3 µm in stage height. Deflection curves were fit to a Hertzian model, with the assumption of a Poisson ratio of 0.5, using a custom Matlab (Mathworks, Natick, MA) script (Rosenbluth, Lam et al. 2006).

5.4 Results and Discussion

Using a glass capillary-based microfluidic hydrodynamic focusing device (Utada, Lorenceau et al. 2005) and careful selection of solvents, non-solvents, and continuous phase solutions, we have produced monodisperse silk microspheres (Figure 1). The two immiscible streams, in this case, are aqueous regenerated silk fibroin solution and oleic acid as the dispersed and continuous phases, respectively (i.e. silk droplets break off in

oleic acid). Within two-phase laminar flow focusing, two droplet-forming regimes are known to exist: dripping and jetting (Utada, Fernandez-Nieves et al. 2007). In the dripping regime, droplet breakup is based on a competition between viscous drag forces on the growing drop and the surface tension forces holding the drop to the bulk fluid, whereas in the jetting regime breakup is initiated by the Rayleigh-Plateau instability within the focused stream. In practice, switching between dripping and jetting is controlled by varying the continuous and dispersed phase flow rates (Q_{outer} and Q_{inner}, respectively) or their ratio (Q_{outer}/Q_{inner}). We maintained device operation in the dripping regime, as the jetting regime has been shown to produce more polydisperse droplets.(Utada, Lorenceau et al. 2005)

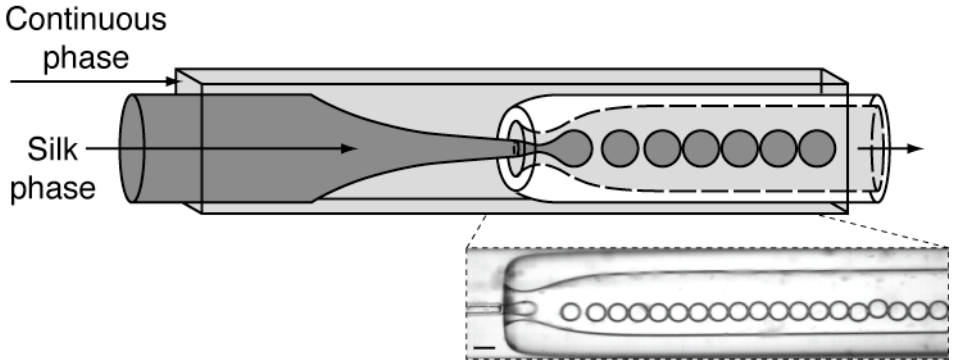

Figure 1. (Top) Schematic of microfluidic device used for the generation of monodisperse silk microspheres, adapted from reference (Utada, Lorenceau et al. 2005). (Bottom) High speed image of the device in operation. Scale bar is 200 μm. The inner diameter of the upstream capillary is 580 μm and is drawn down to ~60 μm. The inner diameter of the downstream capillary is 580 μm, but is decreased to ~300 μm at its inlet.

To produce microspheres that solidify in the device, a suitable non-solvent for silk must be found that is soluble in both phases. Methanol is an established non-solvent for silk protein, causing rapid aggregation and a transition to a β-sheets rich structure (Nam and Park 2001), and is soluble in both oleic acid and water. As the aqueous silk droplets travel through the continous phase, methanol diffuses from the continous phase into the droplets and causes solidification of the silk protein. Although other non-solvents could be used (e.g. ethanol and isopropanol), we chose methanol because of its ability to coagulate silk rapidly. However, we found that increasing the methanol content in the continuous phase above 25 wt.-% caused overly rapid coagulation of the silk, which led to device clogging. There is thus a competition that must be carefully balanced between advection of the silk solution droplets down the device and the solidification and crystallization of the silk as the methanol diffuses into the spheres.

An optical micrograph of two different sized samples of silk microspheres in solution is shown in Figures 2a and 2b. The spheres have a core-shell architecture, with a film surrounding packed crystallites (Figure 2c). The distinct outer shell is likely due to the rapid solidification of the outer edge of the microspheres upon initial exposure to the

methanol-containing continuous phase. The silk fibroin inside of the microspheres is likely crystallized at a much slower rate, due to longer diffusion times because of both radial distance and the diffusive resistance created by the shell. We found that this outer shell could be removed through mechanical shearing, and a “ghost” shell can be seen in Figure 2a. Crushing the spheres between glass slides broke the shell and caused the dispersion of some of the inner crystallites, suggesting they are loosely adhered. SEMs show a roughed surface morphology of dried microspheres with nanoscale wrinkles (Figure 2d), a side effect of the sample drying, and suggesting that the spheres are highly hydrated in solution. Furthermore, the microspheres shrink dramatically in size upon drying, as evidenced by the size of hydrated sphere in Figure 2c and dehydrated sphere in Figure 2d.

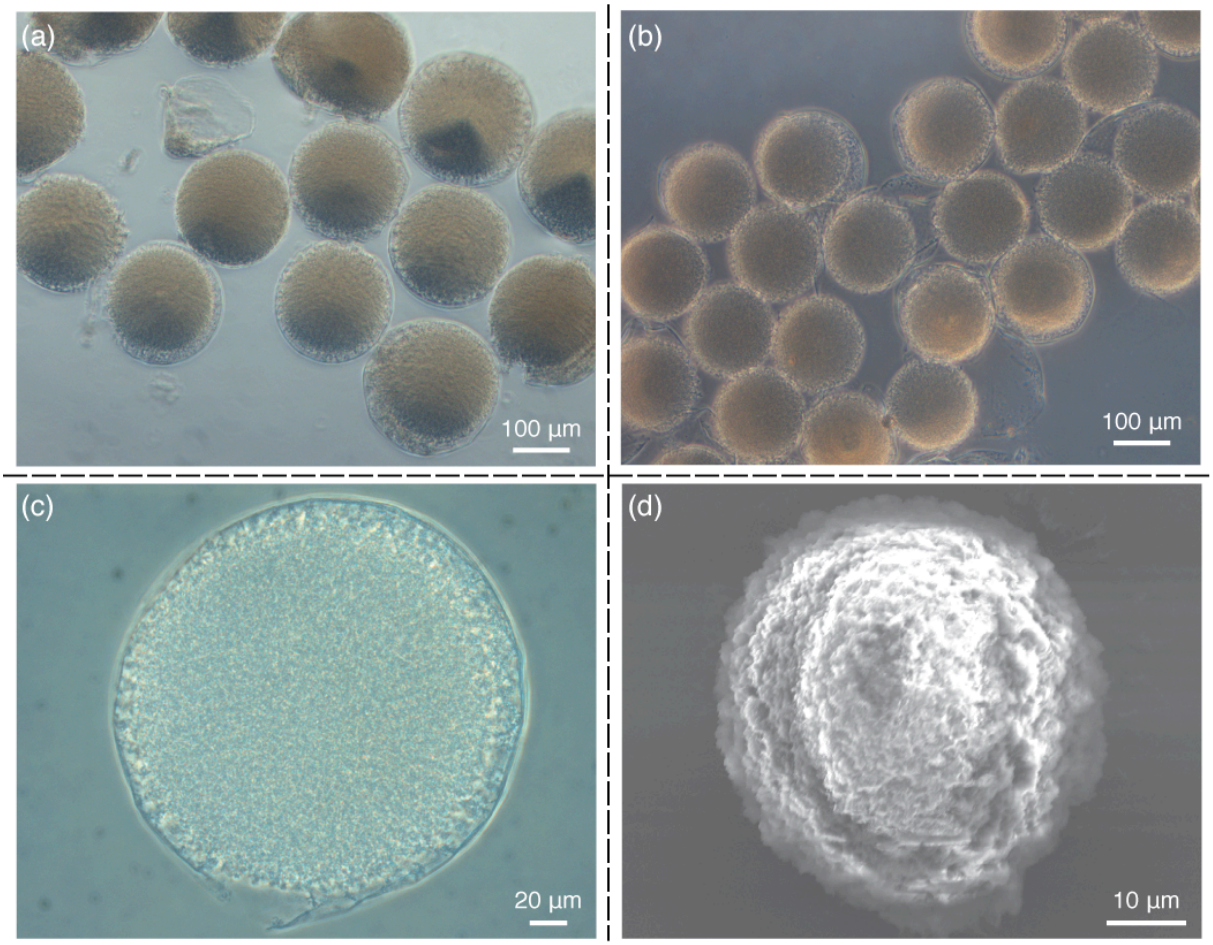

Figure 2. Images of silk microspheres. (a) Silk microspheres produced using a $Q_{outer}/Q_{inner} = 8$. (b) Silk microspheres produced using a $Q_{outer}/Q_{inner} = 14$. (c) High magnification image of a single microsphere ($Q_{outer}/Q_{inner} = 8$). (d) SEM of a dehydrated microsphere ($Q_{outer}/Q_{inner} = 8$).

It has been well established that in microfluidic droplet generating devices, droplet size and production frequency are dependent on the flow rate ratio between the continuous and dispersed flows. We observed that microsphere size decreases

monotonically with increasing flow rate ratio (Figure 3), as expected from a mass balance-based approximation of droplet size in the dripping regime (Utada, Lorenceau et al. 2005). In the present device (dimensions shown in Figure 1) droplet radius was varied from approximately 145-200 µm; we anticipate this range could be easily extended through device design and flow rate ratio to spheres of order 1-10 µm.

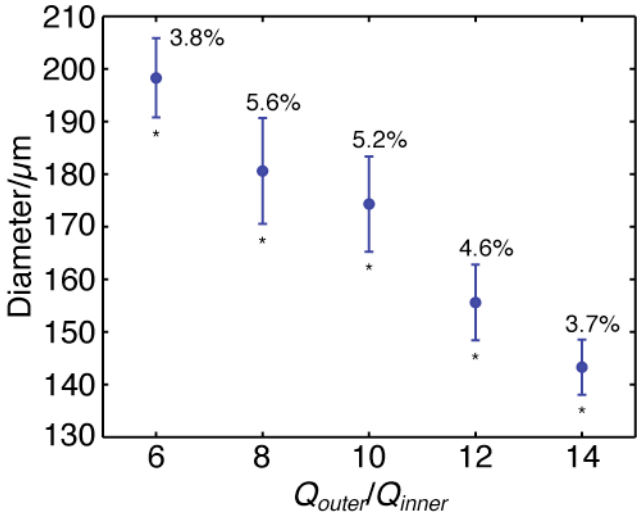

Figure 3. Diameter of silk microspheres produced at increasing flow rate ratios. Error bars represent standard deviation. The percentage value by each data point is the PDI. * indicates statistical significance between adjacent sample means ($p < 0.01$, n=50).

The polydispersity index (PDI) is a measure of the distribution of particle sizes in a suspension and is defined as the coefficient of variation of particle diameters (standard deviation of measured diameters divided by the mean.) In similar microfluidic systems, the PDI of the resulting microspheres generally ranges from <2% to 6% (Kim, Utada et al. 2007; Zhang, Tumarkin et al. 2007; Huang, Lu et al. 2009; Xu, Hashimoto et al. 2009; Zhang, Ju et al. 2009). We produced several individual batches of microspheres, and measured PDIs varying from 3.7% to 5.6%, demonstrating consistent monodispersity (Figure 3).

Fourier transform infrared (FTIR) spectroscopy was used to show the structural transition undergone by the silk droplets after exposure to methanol (Figure 4a). The spectrum of an untreated silk film is shown for comparison. The untreated silk film has peaks at 1651 cm^{-1}, 1541 cm^{-1}, and 1240 cm^{-1}, which are characteristic of random coil conformation, and correspond to the amide I, amide II, and amide III bands, respectively. The methanol-treated spheres show peak shifts to 1623 cm^{-1}, 1520 cm^{-1}, and 1232 cm^{-1}, confirming the expected transition from random coil to β-sheet structure (Chirgadze, Shestopalov et al. 1973; Magoshi, Mizuide et al. 1979), as has been well established for reconstituted silkworm silk upon exposure to methanol (Nam and Park 2001).

The mechanical properties of the ~180 µm diameter silk microspheres were measured with atomic force microscopy (AFM) indentation. An example deflection curve is shown in Figure 4b. The curves do not show an ideally smooth deflection upon

indentation, suggesting that the spheres have a microstructure that rearranges upon the application of force. It is likely that this measured microstructure is a combination of the observed shell around the microspheres and the rearrangement of the β-sheet crystallites that constitute the interior of the sphere. To estimate the stiffness of the spheres, the curves were fit to the common Hertzian mechanics model, which describes the indentation of a sphere with a pyramid punch (the AFM tip). We indented three distinct positions on three different microspheres of the same size (with at least three different measurements per position). Fits of these curves resulted in Young's Moduli for the three spheres of 1.17 ± 0.45 kPa (*n*=11), 1.82 ± 0.92 kPa (*n*=10), and 1.42 ± 0.73 kPa (*n*=10) and an overall average Young's Modulus of 1.46 ± 0.75 kPa (*n*=31). This value is unexpectedly soft, considering the AFM-measured stiffness of methanol-extruded reconstituted silkworm silk fibers was reported to be 5.64 ± 1.36 GPa (Ghosh, Parker et al. 2008), and the stiffness of recombinant spider silk-like mimetic microcapsules was reported to be 0.7-3.6 GPa (Hermanson, Huemmerich et al. 2007). We note, however, that the extruded silkworm silk fibers were prepared from a highly concentrated silk solution (~28-30 wt.-%), dramatically increasing the density of the coagulated silk and more directly mimicking the *in vivo* concentration of native silk solution. We attribute the softness of our spheres to their macrostructure, which consists of loosely adhered, hydrated, crystallites. Dehydrated microspheres were too stiff to be measured with even the stiffest AFM cantilever at our disposal (500 pN/nm), suggesting that the dehydrated and packed crystallites themselves are extremely stiff (data not shown).

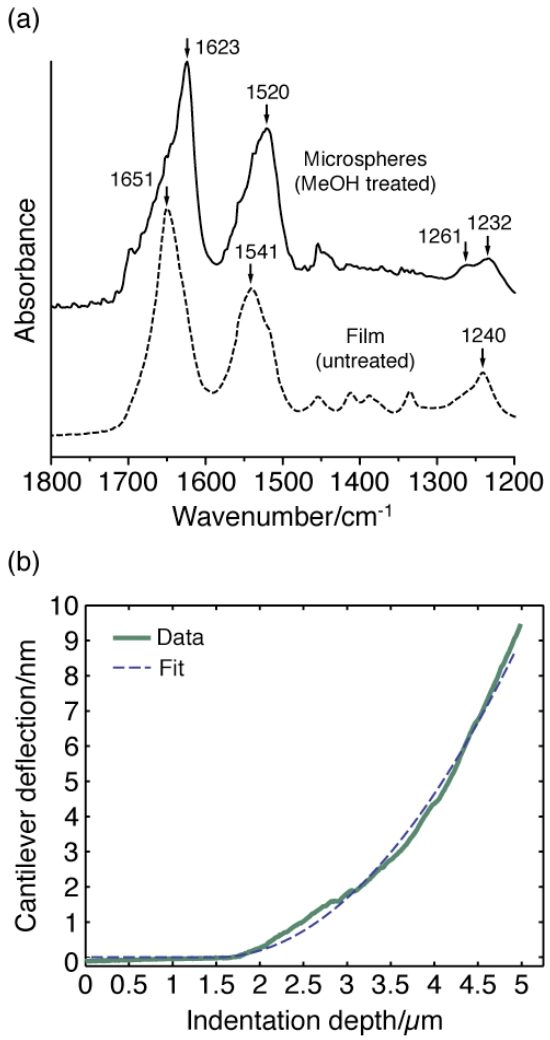

Figure 4. (a) FTIR spectra for an untreated silk film, and methanol-treated silk microspheres. The relevant peaks are marked. (b) An example AFM indentation curve of a microsphere, with its Hertzian fit. All microspheres characterized were produced with Q_{outer}/Q_{inner} = 8 and ~180 μm diameter.

5.5 Conclusions

Herein, we have demonstrated the production of silk microspheres using a two-phase microfluidic flow-focusing device. Leveraging the discrete and periodic breakup of droplets in these systems, we have created silk microspheres with a nearly homogeneous size distribution. Microsphere size could be controlled by the flow rate ratio in the device and the resultant microspheres had the characteristic β-sheet structure of methanol-treated silk. AFM measurements show that the microspheres were surprisingly soft. Of future interest could be cascading laminar flow streams for the production of silk microcapsules (Liu, Yang et al. 2009), and varying coagulants and silk concentration to alter crystallinity (which would affect drug release kinetics) and mechanical properties (Um, Kweon et al. 2004; Wang, Wenk et al. 2007). We anticipate

that these silk microspheres could find use in emulsions and cosmetics. However, given the appropriate biological characterization, their particular utility will likely be found in drug delivery and controlled released, where the benefits of silk protein have been shown, and monodispersity has been proven to be advantageous.

5.6 Acknowledgment

The authors thank Ailey Crow of the Fletcher Lab for assistance with AFM and the Pruitt Lab for use of the FTIR spectrometer. This research was partially supported by University of California Systemwide Biotechnology Research & Education Program GREAT Training Grant 2008-02, and an NDSEG Graduate Fellowship to DNB.

Chapter 6. High Fidelity and High Aspect Ratio Silk Nano- and Micro-molding

The experiments in this chapter were performed in part with Frank B. Myers, Dr. Eric P. Lee, and Brendan W. Turner.

6.1 Abstract

Although silk is commonly known as a fiber, dissolved silk protein has recently received significant attention for its use in creating biocompatible, biodegradable, and mechanically tough materials. These materials have been applied to tissue engineering, biosensors, and microfluidics. Here we show that reconstituted silk fibroin (RSF) is an excellent material for molding of nano- and micro-scale patterned features. RSF alleviates several problems seen with current polymers used for micromolding, such as device collapse and feature rounding. We show feature replication down to 25 nm, and the ability to support high aspect ratio structures up to 3.75 (height to diameter). Theoretical calculations suggest that silk films could support aspect ratios up to 10. We furthermore show that the RSF films are in an α-helical/random coil water soluble state, but can also be crystallized into a β-sheet and water insoluble conformation.

6.2 Introduction

Micropatterning and soft lithography have become extremely popular means of creating nano- and micro-scale scaffolds for applications ranging from protein patterning to tissue engineering to biosensing (Qin, Xia et al. 2010). The most commonly used material in soft lithography is the elastomer polydimethylsiloxane (PDMS) (Qin, Xia et al. 2010). PDMS is simple to prepare and has a large number of characteristics useful for biomedical applications (e.g. gas permeability). However, as the user base and application space of soft lithography has grown, several limitations of PDMS have become apparent. Particularly, PDMS has difficulty replicating nano-scale features, and it does not support high aspect ratio structures (rather, they collapse) (Delamarche, Schmid et al. 1997; Schmid and Michel 2000). Consequently, there has been an avid search for material alternatives to PDMS that can rectify these problems. Most notably, Schmid and Michel have demonstrated the use of so-called “hPDMS,” which is a two-layer system of PDMS on top of a stiffer material (Schmid and Michel 2000; Odom, Love et al. 2002).

It has recently been shown that reconstituted silk solutions can be used to replicate nano- and micro- topographies. These replicate films are particularly advantageous for biomedical uses because of their biocompatibility, biodegradability, and mechanical toughness. Initially Gupta et al. demonstrated that silk dissolved in an ionic liquid could be cast onto a micropatterned surface and phase separated to induce solidification and feature replication (Gupta, Khokhar et al. 2007). Bettinger et al. subsequently demonstrated that aqueous silk solutions could simply be dried on top of micropatterned substrates and that the films replicated the patterned features (Bettinger, Cyr et al. 2007). Kaplan and Omenneto have now demonstrated that silk films can be nanopatterned either by casting and drying, or by embossing, and have been using these nanopatterned silk films for biosensing applications (Omenetto and Kaplan 2008; Amsden, Domachuk et al. 2010). Herein, we demonstrate that in addition to their ability

to be patterned, nano- and micro-patterned silk substrates actually overcome two main structural disadvantages of PDMS for replica molding. In particular, we demonstrate that silk replicates nano-scale features with extremely high fidelity (beyond that of hPDMS) and that silk can be used for molding high aspect ratio structures (for which PDMS collapses).

6.3 Experimental

a. Preparation of Silk Solution

Reconstituted silk fibroin (RSF) was prepared as previously described (Nazarov, Jin et al. 2004). Briefly, *B. mori* silkworm cocoons (Tajima Shoji Co., Ltd., Yokohama, Japan) were boiled twice in 0.02 M Na_2CO_3 for 20 min and rinsed in deionized water to remove sericin glue. The degummed silk was allowed to dry overnight and was dissolved in 9.3 M LiBr for 4 h. The dissolved silk solution was then dialyzed with 3,500 MWCO cassettes (Pierce Biotechnology, Inc., Rockford, IL) against 2 L of Milli-Q water for 48 h, changing the water regularly at least six times. The resultant 4 wt.-% silk solution (as measured by dry weight) was filtered through a 100 μm mesh to remove large debris and stored at 4°C for no more than 2 months.

b. Film Thickness Characterization

RSF was diluted with ultra-pure water to the desired concentration (1.5, 2, 3, 3.5 wt.-%). 200 μL of RSF was pipetted onto a disk 11 mm in diameter and allowed to dry. The resultant film was broken in half, mounted on its edge for imaging its cross section, and sputtered with gold. Scanning electron microscopy was performed on a Hitachi S5000 SEM, and the resultant images were analyzed with ImageJ (Bethesda, Maryland) to measure film thickness. All experiments were performed in triplicate. Student *t*-tests were used to determine statistical significance between sample groups.

c. Master and Mold Fabrication

Nano-structured glass masters (fabricated by interference lithography) were graciously provided by Dr. Tiziana Bond, Lawrence Livermore National Labs. This master was molded with hPDMS (as described below). The hPDMS substrate was subsequently used as a master for further molding of hPDMS and RSF.

Silicon masters were prepared by a deep-reactive ion etching (DRIE) process. Briefly, Si wafers were spin-coated with positive photoresist, exposed to UV light beneath a chrome mask (used to define the desired features), and developed. The patterned resist serves as a mask itself to etch only exposed Si during DRIE. DRIE was performed with an inductively coupled plasma system (STS ASE) using SF_6 plasma for etching and C_4H_8 for passivation. After DRIE, remaining photoresist was stripped with

oxygen plasma, and the wafer was silanized with tridecafluoro-1,1,2,2-tetrahydrooctyl-1-trichloro-silane.

hPDMS was prepared as previously described (Odom, Love et al. 2002). 3.4 g of vinyl PDMS prepolymer (VDT-731, Gelest Corp.), 18 µL of Pt catalyst (SIP6831.1, Gelest Corp.), and a drop of 2,4,6,8-tetramethyl-tetravinylcyclotetrasiloxane (87927, Sigma-Aldrich) were mixed and degassed. 1 g of hydrosilane prepolymer (HMS-301, Gelest Corp.) was subsequently mixed in, and the solution was spin-coated (1000 rpm, 40 s) onto a master. The sample was then cured at 60ºC for 30 min. The hPDMS layer was then coated with ~3 mm of PDMS prepolymer (Sylgard 184, Dow Corning) and cured at 60ºC until fully hardened.

To create RSF molds, RSF solution was pipetted over the master using enough solution to coat the whole master. The sample was then left to dry overnight, and the film was peeled from the master.

d. Imaging

All samples were sputtered with ~2-4 nm of gold and imaged in a Hitachi S5000 scanning electron microscope.

e. FTIR Spectroscopy

Attenuated total reflectance (ATR) Fourier transform infrared (FTIR) spectra were recorded on a Nicolet 360 Avatar ESP spectrometer equipped with a DTGS KBr detector and the ATR accessory (Madison, WI). Spectra were recorded at 4 cm^{-1} resolution, and integrated over 32 scans. A silk film was prepared by allowing a silk solution to dry in a Petri dish. The MeOH treated film was soaked in 100% MeOH overnight and then washed with DI water and allowed to dry.

6.4 Results and Discussion

a. High Fidelity Molding

Figure 1 shows an original master with nano-scale features, and the hPDMS and silk structures molded from an hPDMS replica of the master. We also attempted to mold PDMS, however it produced only slight bumps at the base of the features as if the polymer were unable to completely penetrate the mold features. The base of these features is 200 nm, and PDMS is reported to have a lower replication limit of 500 nm (Odom, Love et al. 2002). hPDMS has a lower replication limit of 50 nm (Odom, Love et al. 2002), and was able to generally mold the nano-scale pillars (Figure 1b). The hPDMS features are very smoothed, likely due to the surface tension of the material. Because these replicas are made from hPDMS molds of the original glass master, it is likely that there is additional feature smoothing due to this replication step. However, examination of the silk features shows extremely high fidelity replication of the glass

original, despite the hPDMS intermediary mold. We measured feature replication down to ~25 nm, which is of similar size scale as previously reported data on silk films (Lawrence, Omenetto et al. 2008).

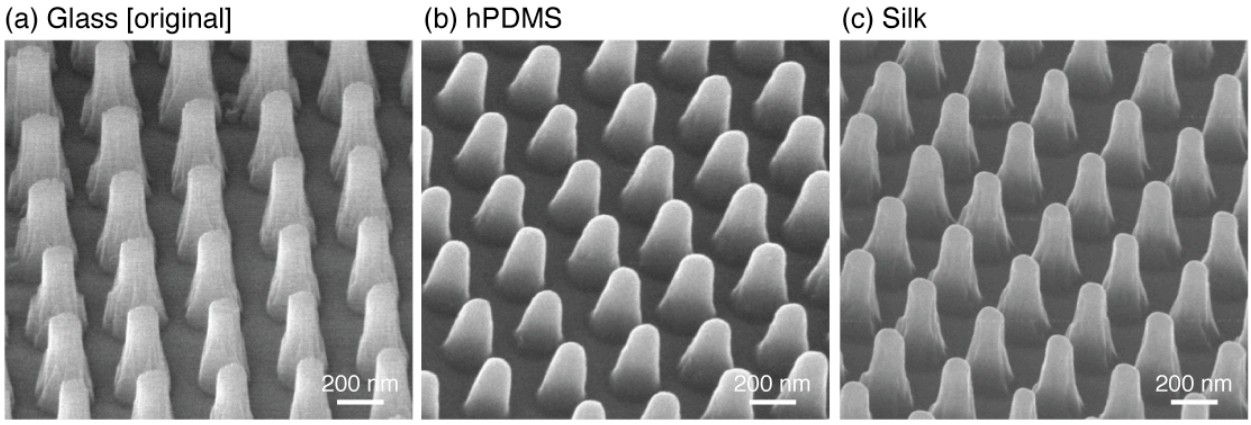

Figure 1. Nanoscale structures and their replicas. (a) Initial master as fabricated in glass by interference lithography. A mold of these features was made in hPDMS, which was subsequently used as a master for (b) and (c). (b,c) hPDMS and silk replicas of the nano-structures.

b. High Aspect Ratio Molding

There are several modes of collapse seen in nano- and micro-scale structures. The ability of a material to support various structures is largely a function of its elastic modulus and its surface energy. Depending on the material and geometry of the structures, failure can occur by (1) ground collapse, whereby structures collapse under their own weight, (2) ground collapse due to adhesion, whereby the surface energy of the material causes the structure to adhere to the substrate floor, and (3) lateral collapse, whereby structures close to each other adhere together by the surface energy of the material. All of these failure modes have been problematic for applications of soft lithography (Odom, Love et al. 2002).

Figure 2a shows PDMS posts molded from a silicon substrate prepared with DRIE. The posts have a diameter (*d*) of 4 µm, edge-to-edge spacing (*w*) of 2 µm, and a height (*h*) of 12 µm. The vast majority of posts immediately collapsed to the ground upon removal of PDMS from the substrate, and were unable to be restored upright despite a variety of attempts (N_2 blowing, isopropanol washing, mechanical shearing, etc). Figure 2b shows silk replicas of the same mold. The silk posts are completely free standing, exhibiting no failure. This is likely due to the 100-fold higher Young's Modulus of silk over PDMS.

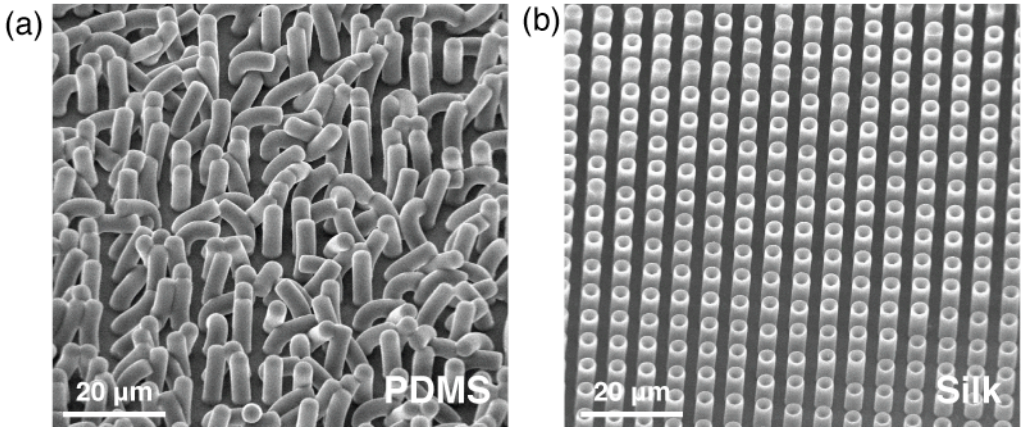

Figure 2. High aspect ratio microposts molded in (a) PDMS and (b) silk. Note that the PDMS posts collapse onto each other, and some are adhered at the tips.

c. Theory

Several studies have pursued a theoretical understanding of the mechanisms of collapse of nano- and micro-scale features, particularly pillars (Zhang, Lo et al. 2006). The analyses developed allow the prediction of critical aspect ratios and geometries at which micropatterned structures will collapse. As mentioned previously, the ability of a material to support high aspect ratio features is largely dependent on its Young's Modulus (E) and it free surface energy (γ_s). The latter property becomes a particularly dominant force at the micro-scale. Table 1 shows various material properties of PDMS and silk films. Notably, silk films have a Young's Modulus two orders of magnitude higher than PDMS.

Table 1. Material properties of PDMS and RSF silk films. Values for PDMS from (Zhang, Lo et al. 2006). Silk data from (Bettinger, Cyr et al. 2007) and (Park, Ha et al. 2001). Work of adhesion (W) for silk is calculated as twice the surface free energy (γ_s) according to (Glassmaker, Jagota et al. 2004).

	E (MPa)	γ_s (mN/m)	W (mN/m)	ρ (kg/m^3)
PDMS	1.7	19.8	44	920
Silk film	108	41	82	1300

Hui et al. calculated that the critical elastic modulus for ground collapse for a nano- or micro-pillar under its own weight is,

$$E_g^* = \frac{qh^3}{7.837I}$$

where $I = \pi d^4/64$ for a circular cylinder and $q = \rho g \pi d^2/4$ is the weight per unit length of the cylinder, ρ is density, and g is gravitational acceleration (Hui, Jagota et al. 2002).

For the pillar array shown in Figure 2, E_g^* = 2.0 Pa for PDMS and E_g^* = 2.8 Pa for silk, suggesting that both materials can support the weight of their pillars.

If adhesive forces are large enough, they can dominate the mechanism of pillar collapse. In this case, the critical elastic modulus for ground collapse due to adhesion is,

$$E_{g,a}^* = \frac{2^{11/2} 3^{3/4} (1-\nu^2)^{1/4} h^{3/2} W}{(\pi d)^{5/2}}$$

where ν is the Poisson ratio (assumed to be 0.5) and W is the work of adhesion (Roca-Cusachs, Rico et al. 2005). For PDMS, $E_{g,a}^*$ = 0.31 MPa and for silk, $E_{g,a}^*$ = 0.58 MPa. In both cases, for the prescribed geometry, PDMS and silk can support the pillars from ground collapse due to adhesive forces.

Most microfabricated pillars are made in dense arrays. In this case, the adhesive forces between the pillars themselves can dominate and cause them to stick together. The critical elastic modulus for lateral collapse due to adhesion is (Hui, Jagota et al. 2002),

$$E_L^* = \frac{5.32 \times h^3 \gamma_s (1-\nu^2)^{1/4}}{d^{5/2} w^{3/2}}.$$

where γ_s is the surface energy of the material. For PDMS, E_L^* = 1.9 MPa and for silk E_L^* = 3.9 MPa. Therefore, it is likely that the mode of failure for the PDMS pillars is due to the lateral interactions between pillars. Increasing the distance between the posts could solve this problem, or alternatively, using a stiffer material such as silk.

We can furthermore calculate the critical aspect ratio that these materials can support before lateral collapse (Glassmaker, Jagota et al. 2004). For circular cylinders, the critical aspect ratio is,

$$\left(\frac{h}{d}\right)_C = \frac{0.57 \times E^{1/3} w^{1/2}}{\gamma_s^{1/3} d^{1/6} (1-\nu^2)^{1/12}}.$$

Therefore, PDMS can support up to h/d = 3 for the prescribed pillar diameter and spacing, and silk can support h/d = 10. Theoretically, the posts arrays shown in Figure 2b could have been fabricated up to 40 μm tall in silk before collapsing.

d. Film Thickness vs. Concentration

Because RSF is molded by evaporating solvent (i.e. water), the resultant film thickness is determined by the remaining solid upon complete drying. We measured film thickness as a function of RSF concentration for a consistent choice of volume and surface area (Figure 3). As expected, film thickness increases with increasing RSF concentration. The relationship is linear, as shown previously (Lawrence, Omenetto et al. 2008).

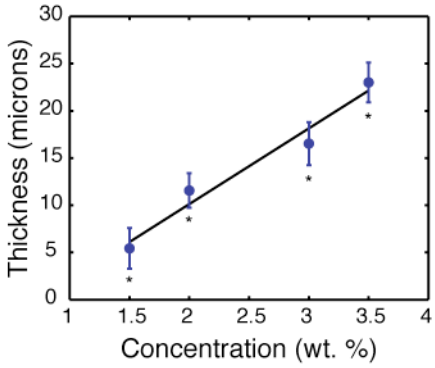

Figure 3. RSF film thickness versus concentration of RSF solution. Error bars represent standard deviation from the mean (n=3). * indicates statistically significant differences between adjacent sample groups (P<0.05). The black line is a linear regression of the data that follows y=8.0235*x-5.9246 (R^2 = 0.96).

e. FTIR Spectroscopy

FTIR spectroscopy was used to study the structure of silk in film form (Figure 4). The spectrum of a methanol-treated silk film is shown for comparison, because methanol is well known to induce a β-sheet structural transition in silk protein (Nam and Park 2001). The untreated silk film has peaks at 1650 cm^{-1}, 1539 cm^{-1}, and 1244 cm^{-1}, which are characteristic of random coil conformation, and correspond to the amide I, amide II, and amide III bands, respectively. The methanol-treated films show peak shifts to 1625 cm^{-1}, 1522 cm^{-1}, and 1238 cm^{-1}, showing the expected transition from random coil to β-sheet structure (Chirgadze, Shestopalov et al. 1973; Magoshi, Mizuide et al. 1979).

Methanol-treated silk films have higher Young's Moduli than untreated films (Jin, Park et al. 2005), suggesting that they could support higher aspect ratio structures as well. However, the β-sheet crystallites in silk are close in size to our smallest measured features (10-20 nm) (Drummy, Farmer et al. 2007). Furthermore, it has been shown that nano-scale topographies in silk films can effect the secondary structure transitions in those areas (Lawrence, Omenetto et al. 2008). Therefore, future efforts will be required to determine how the methanol treatment of silk films affects the fidelity of replication.

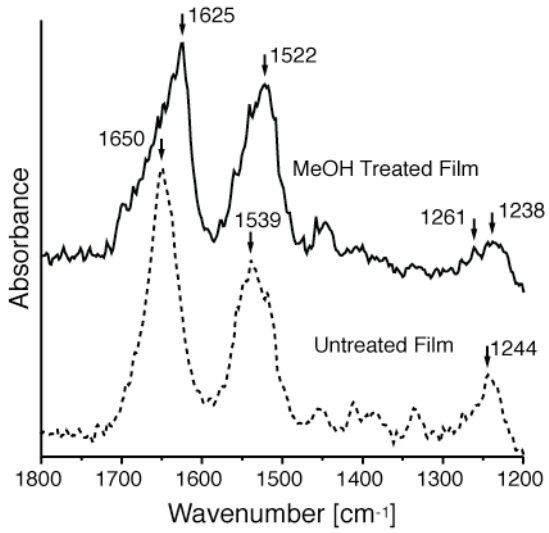

Figure 4. FTIR spectra for an untreated silk film, and a methanol-treated silk film for comparison. The relevant peaks are marked.

6.8 Conclusions

We have demonstrated that RSF solution can be used for high fidelity and high aspect ratio nano- and micro-molding. The resolution of feature fidelity of RSF films is higher than that of conventional polymers used for advanced nano-molding, and the high Young's Modulus of silk allows it to support structures with larger aspect ratios than PDMS (>3x larger, as theoretically predicted). Whereas there are several epoxies with Young's Moduli on the order of 1-3 GPa that have been used for high aspect ratio micromolding, these generally require high temperatures, high pressures, and harsh solvents to mold (Kuo, Zhao et al. 2009). With a simple methanol treatment, silk films have been shown to undergo a structural transition that gives them a Young's Modulus on that same order (Jin, Park et al. 2005). These methanol-treated films could theoretically support much higher aspect ratio structures, however their *β*-crystallite structure could limit their nano-scale replication fidelity.

Nano- and micro-patterned silk films have already seen significant use in tissue engineering and biosensing (Omenetto and Kaplan 2008; Lawrence, Marchant et al. 2009). We anticipate that with their replication fidelity and ability to support unusually tall structures, silk films will be particularly advantageous in areas of research such as biomimetic gecko feet and microneedles for drug delivery where extremely high aspect ratios combined with nano-scale features are critical for performance (Glassmaker, Jagota et al. 2004; Donnelly, Raj Singh et al. 2010).

6.9 Acknowledgement

This work was performed in part with Frank B. Myers, Dr. Eric P. Lee, and Brendan W. Turner. Microfabrication was performed in the UC Berkeley Microfabrication Laboratory. The authors thank Matt Wasilik for assistance with DRIE and the Pruitt Lab for use of

the FTIR spectrometer. This research was partially supported by an NDSEG Graduate Fellowship to D.N.B. and University of California Systemwide Biotechnology Research & Education Program GREAT Training Grant 2008-02.

Chapter 7. Concluding Remarks

In this dissertation I have described my work in the processing of silk protein, both theoretical and experimental. Particularly, my efforts have been focused on silk fiber formation processes, however, as shown, there are numerous non-fiber based applications for silk protein such as microspheres for drug delivery and the molding of nano- and micro-structures.

The majority of my initial efforts with silk protein were based on RSF, which although difficult to dissolve, is fairly simple to handle once prepared. Over time, I realized that RSF does not (and will not) form fibers in the same manner as native dope and will likely never be useful for truly biomimetic fiber spinning. I began efforts to excise dope from spiders and silkworm, which presented its own set of challenges. Now that I have spent a substantial amount of time handling native dope, my understanding of how the silk spinning system works has drastically changed. In fact, I now believe that the role of extensional viscosity in the silk dope is such a critical aspect to the spinning and fiber formation process that it should be the primary focus of any future rheology and simulation work. My hypothesis is that the spinning process is largely based on drawing the fiber due to its extensional viscosity, with no forced extrusion and large pressure drop as often suggested. The gland geometry likely serves as a means of pre-orienting fibroin molecules before they are drawn down into a fiber. Furthermore, the active transport mechanisms in the gland wall dehydrate the fiber as it is being drawn, and slowly induce crystallization through ionic changes to assist the liquid-solid phase transition. The critical role of phase separation and crystallization might be explored through the laminar flow device presented in Chapter 3 or the droplet generation device presented in Chapter 5.

Some additional challenges remain in fully understanding the spinning process. Obviously, understanding the extensional behavior of silk solution is critical, but additionally how this behavior changes as a function of concentration and ionic content. A question that remains in the literature is whether or not sericin acts as a lubrication layer to assist in silk flow. Given how readily native dope can form long fibers at the appropriate pH levels, I do not imagine a lubrication layer being necessary. A question I am often asked is whether or not the bends in the gland are a significant part of the spinning process. I am of the opinion that the gland bends over itself simply as a means of packing. There are only two bends, and in opposing direction, so one could argue that in reversible laminar flow any effects induced by the first bend would be symmetry reversed by the second. It seems more likely that the gland acts analogously to a kidney nephron, using its length and folds as a means of enabling mass transport into and out of the silk solution. A final, curiously unaddressed, question that arises is how does a baby spider or silkworm start its first thread? I have found nothing in the literature on this topic. I imagine that the gland “overflows” with silk, and upon attaching some of it to a substrate, a drawing process can begin and the gland musculature can grip the formed fiber. This remains as a topic for future investigation.

As for non-fiber silk materials, it will be interesting to see the results of new recombinant protein technologies. Current recombinant silk expression systems have such low yields that the utility of the material is limited. When native silk protein can be produced recombinantly in significant quantities, and the protein sequences themselves

can be tailored as desired (e.g. incorporation of additional amino acids with chemically functional side chains), there will likely be a surge in the creation and use of protein-based materials and devices. It will be particularly interesting to see how the mechanical properties of these materials correlate with their primary sequence, and if a means can be established to design a protein sequence for a specific mechanical property.

I hope to have left you, the reader, significantly intrigued by the opportunities available for studying and using silk. It is a non-trivial protein to work with, but can be quite engrossing once you start. I look forward to being part of and witnessing the future advances in the silk field, as they are sure to be exciting and widely beneficial.

References

Abate, A. R., D. Lee, et al. (2008). "Glass coating for PDMS microfluidic channels by sol-gel methods." Lab Chip **8**(4): 516-518.

Agnarsson, I., C. Boutry, et al. (2009). "Supercontraction forces in spider dragline silk depend on hydration rate." Zoology (Jena) **112**(5): 325-331.

Altman, G. H., F. Diaz, et al. (2003). "Silk-based biomaterials." Biomaterials **24**(3): 401-416.

Amsden, J. J., P. Domachuk, et al. (2010). "Biocompatible Films: Rapid Nanoimprinting of Silk Fibroin Films for Biophotonic Applications." Advanced Materials **22**(15).

Anna, S. L. and G. H. McKinley (2007). "Effect of a controlled pre-deformation history on extensional viscosity of dilute polymer solutions." Rheologica Acta **47**(8): 841-859.

Asakura, T., R. Sakaguchi, et al. (1993). "In vitro production of Bombyx mori silk fibroin by organ culture of the posterior silk glands; isotope labeling and fluorination of the silk fibroin." Biotechnology and Bioengineering **41**(2): 245-252.

Asakura, T., K. Umemura, et al. (2007). "Some observations on the structure and function of the spinning apparatus in the silkworm Bombyx mori." Biomacromolecules **8**(1): 175-181.

Atencia, J. and D. J. Beebe (2005). "Controlled microfluidic interfaces." Nature **437**(7059): 648-655.

Ayoub, N. A., J. E. Garb, et al. (2007). "Blueprint for a high-performance biomaterial: full-length spider dragline silk genes." PLoS One **2**(6): e514.

Bell, F. I., I. J. McEwen, et al. (2002). "Fibre science: supercontraction stress in wet spider dragline." Nature **416**(6876): 37.

Bettinger, C. J., K. M. Cyr, et al. (2007). "Silk Fibroin Microfluidic Devices." Advanced Materials **19**(5): 2847-2850.

Bird, B., O. Hassager, et al. (1987). Dynamics of Polymeric Liquids. New York, NY, John Wiley & Sons, Inc.

Boom, R. M., I. M. Wienk, et al. (1992). "Microstructures in Phase Inversion Membranes .2. The Role of a Polymeric Additive." Journal of Membrane Science **73**(2-3): 277-292.

Borenstein, J. T., M. M. Tupper, et al. (2010). "Functional endothelialized microvascular networks with circular cross-sections in a tissue culture substrate." Biomedical Microdevices **12**(1): 71-79.

Boutry, C. and T. A. Blackledge (2009). "Biomechanical variation of silk links spinning plasticity to spider web function." Zoology (Jena) **112**(6): 451-460.

Braun, F. N. and C. Viney (2003). "Modelling self assembly of natural silk solutions." International Journal of Biological Macromolecules **32**(3-5): 59-65.

Cao, Z. B., X. Chen, et al. (2007). "The preparation of regenerated silk fibroin microspheres." Soft Matter **3**(7): 910-915.

Chen, G. Y., J. A. Cuculo, et al. (1992). "Characteristics and Design Procedure of Hyperbolic Dies." Journal of Polymer Science Part B-Polymer Physics **30**(6): 557-561.

Chen, X., D. P. Knight, et al. (2002). "Rheological characterization of nephila spidroin solution." Biomacromolecules **3**(4): 644-648.

Chew, S. Y., Y. Wen, et al. (2006). "The role of electrospinning in the emerging field of nanomedicine." Current Pharmaceutical Design **12**(36): 4751-4770.

Chinali, A., W. Vater, et al. (2010). "Containment of Extended Length Polymorphisms in Silk Proteins." Journal of Molecular Evolution.

Chirgadze, Y. N., B. V. Shestopalov, et al. (1973). "Intensities and other spectral parameters of infrared amide bands of polypeptides in the beta- and random forms." Biopolymers **12**(6): 1337-1351.

Crater, D. H. and J. A. Cuculo (1983). "A Visualization Study of Poly(Ethylene-Terephthalate) Flow Using Potential Chain-Ordering Die Geometries." Journal of Polymer Science Part B-Polymer Physics **21**(11): 2219-2242.

Cubaud, T. and T. G. Mason (2006). "Folding of viscous threads in diverging microchannels." Physical Review Letters **96**(11): 114501.

De Luca, G. and A. D. Rey (2006). "Dynamic interactions between nematic point defects in the spinning extrusion duct of spiders." Journal of Chemical Physics **124**(14): 144904.

Deen, W. M. (1998). Analysis of Transport Phenomena. New York, NY, Oxford University Press.
Delamarche, E., H. Schmid, et al. (1997). "Stability of molded polydimethylsiloxane microstructures." Advanced Materials **9**(9): 741-746.
Denn, M. M. (1980). "Continuous Drawing of Liquids to Form Fibers." Annual Review of Fluid Mechanics **12**: 365-387.
Dicko, C., J. M. Kenney, et al. (2004). "Transition to a beta-sheet-rich structure in spidroin in vitro: the effects of pH and cations." Biochemistry **43**(44): 14080-14087.
Dicko, C., J. M. Kenney, et al. (2006). "Beta-silks: enhancing and controlling aggregation." Advances in Protein Chemistry **73**: 17-53.
Dicko, C., F. Vollrath, et al. (2004). "Spider silk protein refolding is controlled by changing pH." Biomacromolecules **5**(3): 704-710.
Doke, J. (2005). GRABIT.m. Mathworks Matlab Central File Exchange.
Donald, A. M. and A. H. Windle (1992). Liquid crystalline polymers. Cambridge England ; New York, Cambridge University Press.
Donnelly, R. F., T. R. Raj Singh, et al. (2010). "Microneedle-based drug delivery systems: Microfabrication, drug delivery, and safety." Drug Deliv **17**(4): 187-207.
Drummy, L. F., B. L. Farmer, et al. (2007). "Correlation of the beta-sheet crystal size in silk fibers with the protein amino acid sequence." Soft Matter **3**(7): 877-882.
Fiddes, L. K., N. Raz, et al. (2010). "A circular cross-section PDMS microfluidics system for replication of cardiovascular flow conditions." Biomaterials **31**(13): 3459-3464.
Foo, C. W. P., E. Bini, et al. (2006). "Role of pH and charge on silk protein assembly in insects and spiders." Applied Physics A-Materials Science & Processing **82**(2): 223-233.
Freiberg, S. and X. X. Zhu (2004). "Polymer microspheres for controlled drug release." International Journal of Pharmaceutics **282**(1-2): 1-18.
Ghosh, S., S. T. Parker, et al. (2008). "Direct-write assembly of microperiodic silk fibroin scaffolds for tissue engineering applications." Advanced Functional Materials **18**(13): 1883-1889.
Glassmaker, N. J., A. Jagota, et al. (2004). "Design of biomimetic fibrillar interfaces: 1. Making contact." Journal of the Royal Society Interface **1**(1): 23-33.
Gosline, J. M., P. A. Guerette, et al. (1999). "The mechanical design of spider silks: from fibroin sequence to mechanical function." Journal of Experimental Biology **202**(Pt 23): 3295-3303.
Guerette, P. A., D. G. Ginzinger, et al. (1996). "Silk properties determined by gland-specific expression of a spider fibroin gene family." Science **272**(5258): 112-115.
Gupta, M. K., S. K. Khokhar, et al. (2007). "Patterned silk films cast from ionic liquid solubilized fibroin as scaffolds for cell growth." Langmuir **23**(3): 1315-1319.
Gupta, M. K., S. Singamaneni, et al. (2010). "A facile fabrication strategy for patterning protein chain conformation in silk materials." Advanced Materials **22**(1): 115-119.
Haber, L. H., R. D. Schaller, et al. (2004). "Shape control of near-field probes using dynamic meniscus etching." Journal of Microscopy-Oxford **214**: 27-35.
Hardy, J. G., L. M. Roemer, et al. (2008). "Polymeric materials based on silk proteins." Polymer **49**(20): 4309-4327.
Hermanson, K. D., D. Huemmerich, et al. (2007). "Engineered microcapsules fabricated from reconstituted spider silk." Advanced Materials **19**(14): 1810.
Hinman, M., Z. Dong, et al. (1992). "Spider silk: a mystery starting to unravel." Results Probl Cell Differ **19**: 227-254.
Hinman, M. B. and R. V. Lewis (1992). "Isolation of a clone encoding a second dragline silk fibroin. Nephila clavipes dragline silk is a two-protein fiber." J Biol Chem **267**(27): 19320-19324.
Holland, C. (2008). Personal Communication.
Holland, C. (2010). Personal Communication.
Holland, C., A. E. Terry, et al. (2006). "Comparing the rheology of native spider and silkworm spinning dope." Nature Materials **5**(11): 870-874.
Holland, C., A. E. Terry, et al. (2007). "Natural and unnatural silks." Polymer **48**(12): 3388-3392.
Huang, K. S., K. Lu, et al. (2009). "Microfluidic controlling monodisperse microdroplet for 5-fluorouracil loaded genipin-gelatin microcapsules." Journal of Controlled Release **137**(1): 15-19.

Hui, C. Y., A. Jagota, et al. (2002). "Constraints on microcontact printing imposed by stamp deformation." Langmuir **18**(4): 1394-1407.
Hwang, C. M., A. Khademhosseini, et al. (2008). "Microfluidic chip-based fabrication of PLGA microfiber scaffolds for tissue engineering." Langmuir **24**(13): 6845-6851.
Iizuka, E. (1966). "Mechanism of fiber formation by the silkworm, Bombyx mori L." Biorheology **3**(3): 141-152.
Iizuka, E. (1983). "The Physicochemical Properties of Silk Fibers and the Fiber Spinning Process." Experientia **39**(5): 449-454.
Inoue, S., K. Tanaka, et al. (2000). "Silk fibroin of Bombyx mori is secreted, assembling a high molecular mass elementary unit consisting of H-chain, L-chain, and P25, with a 6:6:1 molar ratio." Journal of Biological Chemistry **275**(51): 40517-40528.
James, D. F. (1991). "Flow in a Converging Channel at Moderate Reynolds-Numbers." AIChE Journal **37**(1): 59-64.
James, D. F., G. M. Chandler, et al. (1990). "A Converging Channel Rheometer for the Measurement of Extensional Viscosity." Journal of Non-Newtonian Fluid Mechanics **35**(2-3): 421-443.
Jeong, W., J. Kim, et al. (2004). "Hydrodynamic microfabrication via"on the fly" photopolymerization of microscale fibers and tubes." Lab on a Chip **4**(6): 576-580.
Jiang, P., H. F. Liu, et al. (2006). "Tensile behavior and morphology of differently degummed silkworm (Bombyx mori) cocoon silk fibres." Materials Letters **60**(7): 919-925.
Jin, H. J. and D. L. Kaplan (2003). "Mechanism of silk processing in insects and spiders." Nature **424**(6952): 1057-1061.
Jin, H. J., J. Park, et al. (2005). "Water-stable silk films with reduced beta-sheet content." Advanced Functional Materials **15**(8): 1241-1247.
Johnson, M. A. and D. C. Martin (1999). "Finite element modeling of banded structures in Bombyx mori silk fibres." International Journal of Biological Macromolecules **24**(2-3): 139-144.
Kaplan, D., W. W. Adams, et al. (1994). "Silk - Biology, Structure, Properties, and Genetics." Silk Polymers **544**: 2-16.
Kataoka, K. and I. Uematsu (1977). "Fiber Formation of Silk Fibroin by Silkworm." Kobunshi Ronbunshu **34**(1): 37-41.
Kerkam, K., C. Viney, et al. (1991). "Liquid Crystallinity of Natural Silk Secretions." Nature **349**(6310): 596-598.
Ki, C. S., I. C. Um, et al. (2009). "Acceleration effect of sericin on shear-induced beta-transition of silk fibroin." Polymer **50**(19): 4618-4625.
Kim, J. W., A. S. Utada, et al. (2007). "Fabrication of monodisperse gel shells and functional microgels in microfluidic devices." Angewandte Chemie International Edition **46**(11): 1819-1822.
Kluge, J. A., O. Rabotyagova, et al. (2008). "Spider silks and their applications." Trends in Biotechnology **26**(5): 244-251.
Knight, D. P., M. M. Knight, et al. (2000). "Beta transition and stress-induced phase separation in the spinning of spider dragline silk." International Journal of Biological Macromolecules **27**(3): 205-210.
Knight, D. P. and F. Vollrath (1999). "Liquid crystals and flow elongation in a spider's silk production line." Proceedings of the Royal Society of London Series B-Biological Sciences **266**(1418): 519-523.
Knight, D. P. and F. Vollrath (2001). "Changes in element composition along the spinning duct in a Nephila spider." Naturwissenschaften **88**(4): 179-182.
Kojic, N., J. Bico, et al. (2006). "Ex vivo rheology of spider silk." Journal of Experimental Biology **209**(Pt 21): 4355-4362.
Kojic, N., M. Kojic, et al. (2004). "Solvent removal during synthetic and Nephila fiber spinning." Biomacromolecules **5**(5): 1698-1707.
Kuo, J. S., Y. Zhao, et al. (2009). "Microfabricating high-aspect-ratio structures in polyurethane-methacrylate (PUMA) disposable microfluidic devices." Lab Chip **9**(13): 1951-1956.
Lammel, A., M. Schwab, et al. (2008). "Processing conditions for the formation of spider silk microspheres." ChemSusChem **1**(5): 413-416.
LaNieve, H. (1975). Spinning Method. U.S. Patent Office. United States. **U.S. Patent #3,925,525**.

Larson, R. G. (1999). The structure and rheology of complex fluids. New York, Oxford University Press.
Lawrence, B. A., C. A. Vierra, et al. (2004). "Molecular and mechanical properties of major ampullate silk of the black widow spider, Latrodectus hesperus." Biomacromolecules **5**(3): 689-695.
Lawrence, B. D., M. Cronin-Golomb, et al. (2008). "Bioactive silk protein biomaterial systems for optical devices." Biomacromolecules **9**(4): 1214-1220.
Lawrence, B. D., J. K. Marchant, et al. (2009). "Silk film biomaterials for cornea tissue engineering." Biomaterials **30**(7): 1299-1308.
Lawrence, B. D., F. Omenetto, et al. (2008). "Processing methods to control silk fibroin film biomaterial features." Journal of Materials Science **43**(21): 6967-6985.
Lazaris, A., S. Arcidiacono, et al. (2002). "Spider silk fibers spun from soluble recombinant silk produced in mammalian cells." Science **295**(5554): 472-476.
Lee, J. S., R. Dylla-Spears, et al. (2007). "Microfluidic four-roll mill for all flow types." Applied Physics Letters **90**(7): 074103.
Lefevre, T., S. Boudreault, et al. (2008). "Conformational and Orientational Transformation of Silk Proteins in the Major Ampullate Gland of Nephila clavipes Spiders." Biomacromolecules **9**(9): 2399-2407.
Lesuer, D. R., C. K. Syn, et al. (1999). "Microstructure-property relations in As-extruded ultrahigh-carbon steels." Metallurgical and Materials Transactions A-Physical Metallurgy and Materials Science **30**(6): 1559-1568.
Li, D. F., T. S. Chung, et al. (2004). "Thickness dependence of macrovoid evolution in wet phase-inversion asymmetric membranes." Industrial & Engineering Chemistry Research **43**(6): 1553-1556.
Liivak, O., A. Blye, et al. (1998). "A microfabricated wet-spinning apparatus to spin fibers of silk proteins. Structure-property correlations." Macromolecules **31**(9): 2947-2951.
Liu, L., J. P. Yang, et al. (2009). "Microfluidic preparation of monodisperse ethyl cellulose hollow microcapsules with non-toxic solvent." Journal of Colloid and Interface Science **336**(1): 100-106.
Liu, Y., Z. Shao, et al. (2008). "Elasticity of spider silks." Biomacromolecules **9**(7): 1782-1786.
Liu, Y., Z. Z. Shao, et al. (2005). "Extended wet-spinning can modify spider silk properties." Chemical Communications(19): 2489-2491.
Macosko, C. W. and R. G. Larson (1993). Rheology: principles, measurements, and applications. New York, NY, VCH.
Magoshi, J., Y. Magoshi, et al. (1985). "Crystallization, Liquid-Crystal, and Fiber Formation of Silk Fibroin." Applied Polymer Symposia(41): 187-204.
Magoshi, J., M. Mizuide, et al. (1979). "Physical-Properties and Structure of Silk .6. Conformational-Changes in Silk Fibroin Induced by Immersion in Water at 2-Degrees-C to 130-Degrees-C." Journal of Polymer Science Part B-Polymer Physics **17**(3): 515-520.
Martel, A. (2008). Silk Protein Aggregation in a Microfluidic Environment, Universite Joseph Fourier - Grenoble I. **Ph.D. Dissertation**.
Martel, A., M. Burghammer, et al. (2008). "A microfluidic cell for studying the formation of regenerated silk by synchrotron radiation small- and wide-angle X-ray scattering." Biomicrofluidics **2**(2): 24104.
Martel, A., M. Burghammer, et al. (2008). "Silk fiber assembly studied by synchrotron radiation SAXS/WAXS and Raman spectroscopy." Journal of the American Chemical Society **130**(50): 17070-17074.
McKinley, G. H. and T. Sridhar (2002). "Filament-stretching rheometry of complex fluids." Annual Review of Fluid Mechanics **34**: 375-415.
Ming-Liang, S., S. V. Nair, et al. (1994). "Deformation mechanism and fibre toughening of nylon 6,6." Polymer **35**(2): 306-314.
Moriya, M., K. Ohgo, et al. (2008). "Flow analysis of aqueous solution of silk fibroin in the spinneret of Bombyx mori silkworm by combination of viscosity measurement and finite element method calculation." Polymer **49**(4): 952-956.
Nam, J. and Y. H. Park (2001). "Morphology of regenerated silk fibroin: Effects of freezing temperature, alcohol addition, and molecular weight." Journal of Applied Polymer Science **81**(12): 3008-3021.
Nazarov, R., H. J. Jin, et al. (2004). "Porous 3-D scaffolds from regenerated silk fibroin." Biomacromolecules **5**(3): 718-726.

Odom, T. W., J. C. Love, et al. (2002). "Improved pattern transfer in soft lithography using composite stamps." Langmuir **18**(13): 5314-5320.
Oliveira, M. S. N., M. A. Alves, et al. (2007). "Viscous flow through microfabricated hyperbolic contractions." Experiments in Fluids **43**(2-3): 437-451.
Omenetto, F. G. and D. L. Kaplan (2008). "A new route for silk." Nature Photonics **2**(11): 641-643.
Ortlepp, C. S. and J. M. Gosline (2004). "Consequences of forced silking." Biomacromolecules **5**(3): 727-731.
Park, W. H., W. S. Ha, et al. (2001). "Relationships between Antithrombogenicity and Surface Free Energy of Regenerated Silk Fibroin Films." Fibers and Polymers **2**(2): 58-63.
Parker, S. T., P. Domachuk, et al. (2009). "Biocompatible Silk Printed Optical Waveguides." Advanced Materials **21**(23): 2411.
Pathak, J. A., D. Ross, et al. (2004). "Elastic flow instability, curved streamlines, and mixing in microfluidic flows." Physics of Fluids **16**(11): 4028-4034.
Peng, N., T. S. Chung, et al. (2008). "Macrovoid evolution and critical factors to form macrovoid-free hollow fiber membranes." Journal of Membrane Science **318**(1-2): 363-372.
Perez-Rigueiro, J., M. Elices, et al. (2002). "Effect of degumming on the tensile properties of silkworm (Bombyx mori) silk fiber." Journal of Applied Polymer Science **84**(7): 1431-1437.
Perez-Rigueiro, J., C. Viney, et al. (2000). "Mechanical properties of single-brin silkworm silk." Journal of Applied Polymer Science **75**(10): 1270-1277.
Perkins, T. T., D. E. Smith, et al. (1997). "Single polymer dynamics in an elongational flow." Science **276**(5321): 2016-2021.
Qin, D., Y. Xia, et al. (2010). "Soft lithography for micro- and nanoscale patterning." Nature Protocols **5**(3): 491-502.
Rammensee, S., U. Slotta, et al. (2008). "Assembly mechanism of recombinant spider silk proteins." Proceedings of the National Academy of Sciences of the United States of America **105**(18): 6590-6595.
Roca-Cusachs, P., F. Rico, et al. (2005). "Stability of microfabricated high aspect ratio structures in poly(dimethylsiloxane)." Langmuir **21**(12): 5542-5548.
Rosenbluth, M. J., W. A. Lam, et al. (2006). "Force microscopy of nonadherent cells: a comparison of leukemia cell deformability." Biophysical Journal **90**(8): 2994-3003.
Schmid, H. and B. Michel (2000). "Siloxane polymers for high-resolution, high-accuracy soft lithography." Macromolecules **33**(8): 3042-3049.
Schonfeld, F. and S. Hardt (2004). "Simulation of helical flows in microchannels." AIChE Journal **50**(4): 771-778.
Seo, C. T., C. H. Bae, et al. (2004). "Fabrication of circular-type microchannel using photoresist reflow and isotropic etching for microfluidic devices." Japanese Journal of Applied Physics **43**(11A): 7773-7776.
Shah, R. K., J. W. Kim, et al. (2008). "Fabrication of monodisperse thermosensitive microgels and gel capsules in microfluidic devices." Soft Matter **4**(12): 2303-2309.
Shao, Z. and F. Vollrath (2002). "Surprising strength of silkworm silk." Nature **418**(6899): 741.
Shear, W. A., J. M. Palmer, et al. (1989). "A Devonian Spinneret: Early Evidence of Spiders and Silk Use." Science **246**(4929): 479-481.
Shin, S. J., J. Y. Park, et al. (2007). ""On the fly" continuous generation of alginate fibers using a microfluidic device." Langmuir **23**(17): 9104-9108.
Sinha, V. R. and A. Trehan (2003). "Biodegradable microspheres for protein delivery." Journal of Controlled Release **90**(3): 261-280.
Sirichaisit, J., V. L. Brookes, et al. (2003). "Analyis of structure/property relationships in silkworm (Bombyx mori) and spider dragline (Nephila edulis) silks using Raman spectroscopy." Biomacromolecules **4**(2): 387-394.
Smith, D. E., H. P. Babcock, et al. (1999). "Single-polymer dynamics in steady shear flow." Science **283**(5408): 1724-1727.
Smolders, C. A., A. J. Reuvers, et al. (1992). "Microstructures in Phase-Inversion Membranes .1. Formation of Macrovoids." Journal of Membrane Science **73**(2-3): 259-275.

Sponner, A., E. Unger, et al. (2005). "Differential polymerization of the two main protein components of dragline silk during fibre spinning." Nature Materials **4**(10): 772-775.
Sponner, A., W. Vater, et al. (2007). "Composition and hierarchical organisation of a spider silk." PLoS One **2**(10): e998.
Sudarsan, A. P. and V. M. Ugaz (2006). "Fluid mixing in planar spiral microchannels." Lab on a Chip **6**(1): 74-82.
Terry, A. E., D. P. Knight, et al. (2004). "pH induced changes in the rheology of silk fibroin solution from the middle division of Bombyx mori silkworm." Biomacromolecules **5**(3): 768-772.
Teule, F., A. R. Cooper, et al. (2009). "A protocol for the production of recombinant spider silk-like proteins for artificial fiber spinning." Nature Protocols **4**(3): 341-355.
Thorsen, T., R. W. Roberts, et al. (2001). "Dynamic pattern formation in a vesicle-generating microfluidic device." Physical Review Letters **86**(18): 4163-4166.
Trabbic, K. A. and P. Yager (1998). "Comparative structural characterization of naturally- and synthetically-spun fibers of Bombyx mori fibroin." Macromolecules **31**(2): 462-471.
Um, I. C., H. Kweon, et al. (2004). "Wet spinning of silk polymer. I. Effect of coagulation conditions on the morphological feature of filament." International Journal of Biological Macromolecules **34**(1-2): 89-105.
Utada, A. S., L. Y. Chu, et al. (2007). "Dripping, jetting, drops, and wetting: The magic of microfluidics." MRS Bulletin **32**(9): 702-708.
Utada, A. S., A. Fernandez-Nieves, et al. (2007). "Dripping to jetting transitions in coflowing liquid streams." Physical Review Letters **99**(9): 094502.
Utada, A. S., E. Lorenceau, et al. (2005). "Monodisperse double emulsions generated from a microcapillary device." Science **308**(5721): 537-541.
Viney, C. (1997). "Natural silks: archetypal supramolecular assembly of polymer fibres." Supramolecular Science **4**(1-2): 75-81.
Vogelaar, L., J. N. Barsema, et al. (2003). "Phase separation micromolding - PSμM." Advanced Materials **15**(16): 1385.
Vogelaar, L., R. G. H. Lammertink, et al. (2005). "Phase separation micromolding: A new generic approach for microstructuring various materials." Small **1**(6): 645-655.
Vogrin, N., C. Stropnik, et al. (2002). "The wet phase separation: the effect of cast solution thickness on the appearance of macrovoids in the membrane forming ternary cellulose acetate/acetone/water system." Journal of Membrane Science **207**(1): 139-141.
Vollrath, F. (2000). "Strength and structure of spiders' silks." Journal of Biotechnology **74**(2): 67-83.
Vollrath, F. and D. P. Knight (2001). "Liquid crystalline spinning of spider silk." Nature **410**(6828): 541-548.
Vollrath, F., B. Madsen, et al. (2001). "The effect of spinning conditions on the mechanics of a spider's dragline silk." Proceedings of the Royal Society of London Series B-Biological Sciences **268**(1483): 2339-2346.
Wang, L. Y., G. H. Ma, et al. (2005). "Preparation of uniform sized chitosan microspheres by membrane emulsification technique and application as a carrier of protein drug." Journal of Controlled Release **106**(1-2): 62-75.
Wang, X., E. Wenk, et al. (2007). "Silk coatings on PLGA and alginate microspheres for protein delivery." Biomaterials **28**(28): 4161-4169.
Wang, X., E. Wenk, et al. (2007). "Silk microspheres for encapsulation and controlled release." Journal of Controlled Release **117**(3): 360-370.
Weber, J. (2010). Polyamides, General. Kirk-Othmer Encyclopedia of Chemical Technology, John Wiley & Sons.
Wenk, E., A. J. Wandrey, et al. (2008). "Silk fibroin spheres as a platform for controlled drug delivery." Journal of Controlled Release **132**(1): 26-34.
Willcox, P. J., S. P. Gido, et al. (1996). "Evidence of a cholesteric liquid crystalline phase in natural silk spinning processes." Macromolecules **29**(15): 5106-5110.
Wong, C. C., A. Agarwal, et al. (2007). "Fabrication of self-sealed circular nano/microfluidic channels in glass substrates." Nanotechnology **18**(13): -.

Xie, F., H. H. Zhang, et al. (2006). "Effect of shearing on formation of silk fibers from regenerated Bombyx mori silk fibroin aqueous solution." International Journal of Biological Macromolecules **38**(3-5): 284-288.
Xie, R., H. Wu, et al. (2008). "The Preparation of Silk Fibroin Drug-loading Microspheres." Journal of Fiber Bioengineering and Informatics **1**(1): 73-80.
Xu, Q., M. Hashimoto, et al. (2009). "Preparation of monodisperse biodegradable polymer microparticles using a microfluidic flow-focusing device for controlled drug delivery." Small **5**(13): 1575-1581.
Yamada, H., H. Nakao, et al. (2001). "Preparation of undegraded native molecular fibroin solution from silkworm cocoons." Materials Science & Engineering C-Biomimetic and Supramolecular Systems **14**(1-2): 41-46.
Yamaura, K., Y. Okumura, et al. (1985). "Flow-Induced Crystallization of Bombyx-Mori L Silk Fibroin from Regenerated Aqueous-Solution and Spinnability of Its Solution." Applied Polymer Symposia(41): 205-220.
Yeo, J. H., K. G. Lee, et al. (2003). "Simple preparation and characteristics of silk fibroin microsphere." European Polymer Journal **39**(6): 1195-1199.
Zhang, H., X. J. Ju, et al. (2009). "A microfluidic approach to fabricate monodisperse hollow or porous poly(HEMA-MMA) microspheres using single emulsions as templates." Journal of Colloid and Interface Science **336**(1): 235-243.
Zhang, H., E. Tumarkin, et al. (2007). "Exploring microfluidic routes to microgels of biological polymers." Macromolecular Rapid Communications **28**(5): 527-538.
Zhang, Y., C. W. Lo, et al. (2006). "Replica molding of high-aspect-ratio polymeric nanopillar arrays with high fidelity." Langmuir **22**(20): 8595-8601.
Zhao, C., J. Yao, et al. (2003). "Structural characterization and artificial fiber formation of Bombyx mori silk fibroin in hexafluoro-iso-propanol solvent system." Biopolymers **69**(2): 253-259.
Zhou, G. Q., Z. Z. Shao, et al. (2009). "Silk Fibers Extruded Artificially from Aqueous Solutions of Regenerated Bombyx mori Silk Fibroin are Tougher than their Natural Counterparts." Advanced Materials **21**(3): 366-370.
Zhou, L., X. Chen, et al. (2005). "Effect of metallic ions on silk formation in the Mulberry silkworm, Bombyx mori." Journal of Physical Chemistry B **109**(35): 16937-16945.
Zhou, S. B., H. S. Peng, et al. (2008). "Preparation and characterization of a novel electrospun spider silk fibroin/poly(D,L-lactide) composite fiber." Journal of Physical Chemistry B **112**(36): 11209-11216.

Appendices

Appendix A - Preparation of Aqueous *Bombyx Mori* Silk Solution

This protocol is modified from that of the laboratory of Dr. David Kaplan, Tufts University.

Materials

1. Silkworm cocoons

The quality of the cocoons matters. Older cocoons tend to be more difficult to dissolve. Fresh cocoons (not yet heat dried) are always best, but more expensive and difficult to purchase. An excellent source of bulk *Bombyx Mor*i silkworm cocoons (courtesy of Dr. David Kaplan, Tufts University) is,

Tajima Shoji Co. LTD
2-21-1-1005 Sumiyoshicho
Naka-ki, Yokohama, Japan 231-0013
yt-silk2066@u01.gate01.com
(81) 45-664-2066

As of 10/2007, 2 kg of cocoons cost ¥18,600.00

Bad Cocoons

Good Cocoons

2. Sodium carbonate (Na_2CO_3, 105.99 g/mol)
3. Lithium bromide (LiBr, 86.85 g/mol)

Although I have not experienced this myself, I have been told that sometimes the LiBr can be “bad.” Be wary of this if you have trouble with dissolution.

4. 2 L beaker, 100 mL beaker
5. 30 mL syringe
6. 18 gauge syringe needles
7. Pierce Scientific Dialysis Cassette, 3-12 mL capacity, 3.5K MWCO
8. Scissors, stirring plate, stir bars, oven (60°C), plastic weighing dishes, desiccator, pipette, tips

Methods

Degumming

Silkworm silk is covered with a glue called sericin. It is extremely important to remove all sericin from the cocoons, otherwise it will contaminate your solution. Sericin on your silk will inhibit dissolution, and trace amounts of sericin can induce gelation of the aqueous silk solution.

1. Cut dried cocoons into smaller pieces, and collect **10 g** of cocoon pieces.

I recommend using scissors to cut the cocoon in half along its long axis, and the strips along its short axis. The smaller pieces you cut, the easier the degumming the dissolution will be.

2. Fill a glass beaker with **2 L of MilliQ water**, cover with foil, and heat to boiling.

Do not exceed 100°C, as this will degrade the silk protein. The degradation will significantly alter gelation times, viscosity, and elastic behavior of the silk solution. (However, so will residual sericin!)

3. Add 0.02 M Sodium carbonate (**4.24 g Na_2CO_3**) to the water and allow complete dissolution.
4. Put the cocoon pieces into the beaker and allow to boil for 25 minutes. Pour out the supernatant, briefly wash the silk, and boil again in Sodium carbonate for 25 minutes.

The cocoon bits should begin to fluff up. Leave the stirring rod going to help break up the cocoons and occasionally help the stirring process by hand with a glass stirring rod.

Although you can get away with only boiling once, I recommend boiling twice as to be sure to remove all the sericin. This is particularly important if you are going to be concentrating the solution later. Otherwise, the silk seems to quickly gel as a thick film on the inside of the dialysis membrane and inhibits diffusion and the concentration process.

5. Pour out the supernatant into the sink and rinse the silk with MilliQ water (be careful, it is very hot). Squeeze all the water out of the silk.
6. Fill a clean beaker with 2 L of MilliQ water, and add the boiled silk. The silk will hydrate again and puff out. Let the silk sit in MilliQ water, with stirring, for 20 minutes.

In order to aid in dispersion of the silk, I also recommend taking scissors during this time to repeatedly cut the silk fibers as fine as you can. The finer the better. To collect the silk, I recommend using a loose mesh metal grating from the hardware store as a filter when you pour out the water.

7. Change the water and do the same procedure 2 more times (3 times total, of each 20 minutes). Each time you change the water, try to squeeze as much water out of the silk as possible.
8. Squeeze out as much water from the silk as possible, spread out the silk on to a piece of foil, and allow to dry in the hood for at least 12 hours. It should be completely

dry before dissolution, otherwise it will not completely dissolve.

Dissolution

1. Prepare a solution of 9.3 M solution of LiBr in MilliQ water.

I recommend making 20 mL of solution, which will allow filling of two dialysis cassettes. **20 mL** of 9.3 M LiBr amounts to **16.2 g LiBr**. Fill the beaker with the LiBr powder, and then add the measured out MilliQ water, such that you can pour the water along the edges of the beaker and get all the powder. The solution may need a little bit of stirring with a glass rod to completely dissolve.

2. Make a 20 w/v % solution of silk in LiBr.

For 20mL (you have to measure out that much) LiBr solution, 20 w/v % amounts to **4 g of silk**.

Add silk to the LiBr solution bit by bit, pushing the silk slightly to get it wet in order to help dissolution.

There will be debris in the silk solution, but don't worry about them. We'll remove them later.

The silk may not completely dissolve instantly. After four hours in the oven (step 3), it will be solution.

3. Put in the oven at 60°C for 4 hours.

Dialysis

1. Rinse dialysis cassette (3-12 mL capacity, 3.5K MWCO) in MilliQ water for 30 mins.
2. Attach an 18 gauge needle to the 30 mL syringe, and remove the syringe plunger. Pour in ~12 mL of silk solution and replace the plunger.

I recommend pouring the silk into the syringe, rather then sucking it in through the syringe to minimize shearing. The needle on the syringe will provide plenty of resistance from the solution flowing out.

3. Fill cassette with 12 mL of Silk-LiBr solution.

It is important to read the instruction manual for the cassettes. Specifically noting how to fill them and to remove excess air.

The Silk-LiBr solution can be very viscous and will flow slowly, so have patience. Try to fill it as slowly as possible. Fast shearing, and a lot of shearing, will cause the silk to crystallize and precipitate out of solution.

You may have to change the syringe tip half-way through, as it will begin to get clogged by debris.

4. Put the cassette with a buoy in 1 L of MilliQ water, with stirring, and cover with foil.

Stir at a slow to moderate speed. Just not so fast that the cassette is spinning.

I often put two cassettes in 2L of MilliQ water.

5. Change the water after 1 hr, 4 hrs, in the evening, the next morning, the next night, and the following morning (6 changes total). The silk should be dialyzing for ~48 hrs.

Collection

1. Collect the silk solution from the dialysis cassette. It will now be about twice the volume (~24 mL) and ~6-8 w/v %.

Whereas you can do this with a syringe, I prefer not to shear the silk even more. Rather, I cut the membrane with a blade, over a 50 mL centrifuge tube and let the solution leak in.

2. Filter the silk solution in a fine mesh to remove large debris.

I recommend Aquatic Eco-Systems (http://www.aquaticeco.com) 100 micron filter. They sell aquarium filters with various size pores (100 microns, 200 microns, etc).

Alternatively, you can centrifuge the silk for 20 mins at 5-10°C at 9000 rpm, 2 times. However, I find it difficult to remove the smaller debris with this method.

3. You can store the silk in the fridge for up to a month or so. Eventually it will gel up into a solid white block, but that takes awhile. If you're going to concentrate the solution, I would recommend using the freshest solution possible.

Appendix B - Preparation of Concentrated (20-30%) Aqueous *Bombyx Mori* Silk Solution

This protocol is mostly copied from that of the laboratory of Dr. David Kaplan, Tufts University, with assistance from Dr. Xianyan Wang and Michael L. Lovett, but modified and annotated.

Materials

1. 8-10 w/v % aqueous silk solution
2. Polyethylene glycol (PEG, 10kDa)
3. 500 mL beaker
4. 10 mL syringe
5. 18 gauge syringe needles
6. Pierce Scientific Dialysis Cassette, **0.5-3 mL capacity**, 3.5K MWCO
7. Stirring plate, stir bar

Methods

1. Allow the dialysis cassette to hydrate in MilliQ water for 30 minutes.
2. Prepare 10 w/v % PEG in MilliQ water.

400 mL of 10 w/v % PEG amounts to **40 g PEG**. However, when the PEG completely mixes, the solution volume increase to more than 400 mL. You can save the extra solution, or try lowering the volume of PEG solution you create such that you get exactly 400 mL. It should be 10 w/v % though.

3. If your non-concentrated silk solution looks cloudy or dirty, filter it with a syringe filter.

Otherwise the silk will just gel up during the concentration process. Use a 0.2 micron pore syringe filter, and filter the solution slowly. One you feel strong resistance, change the filter because it is clogged. You may have to use several filters to completely filter upward 40 mL of silk solution.

Also, this will help get small aggregates out of your solution, which can clog small diameter spinnerets.

4. Attach an 18 gauge needle to the 10 mL syringe, and remove the syringe plunger. Pour in 10 mL of 8-10 w/v % silk solution and replace the plunger.

I recommend pouring the silk into the syringe, rather then sucking it in through the syringe to minimize shearing. You can attach a stop valve to the end of the syringe to stop the solution from flowing out.

5. Fill a 0.5-3 mL capacity cassette with 10 mL of silk solution.

It is important to read the instruction manual for the cassettes. Specifically noting how to fill them and to remove excess air. However, 10 mL is obviously larger capacity than the cassette. The membrane will puff out a lot, but it can hold 10 mL. Be sure to remove all the air from the cassette after filling.

The silk solution will be viscous and will flow slowly, so have patience. Try to fill it as slowly as possible. Fast shearing, and a lot of shearing, will cause the silk to crystallize and precipitate out of solution.

6. Put the cassette in 400 mL of PEG solution, with stirring, and cover. Allow to dialyze for 22-26 hrs (I would err on the side of 22 hours.)

The ratio of PEG solution:silk will be 40:1. Keep stirring on the lowest setting in order to avoid localized concentration effects. If you decide to use 15 w/v % PEG, allow dialysis for 12-16 hrs.

7. Collect the silk solution from the dialysis cassette. You can store it for about 7-10 days depending on the concentration.

You should be collected about 2.5 mL to 2.7 mL, so you only need to use a 3 mL syringe.

Other Concentration Methods

Others have concentrated silk solution by evaporation. I have tried using centrifugal concentrators, with limited success. Depending on the centrifugal concentrator, you generally end up with highly concentrated solution against the membrane, and low concentration solution on top of that. It is also very difficult to retrieve the highly concentrated silk solution from the concentrators.

Appendix C - Raising and Dissecting Silkworms

These notes are based on my personal experience raising silkworms and dissecting out silk from their silk glands. There are many guides to raising silkworms out there, so if you have trouble, there is no shortage of troubleshooting guides. For some other procedures on washing silk excised from the gland, see the work of J. Magoshi.

Notes on Raising Worms

1. Currently, there are three silkworm suppliers on the west coast:
    a. Mulberry Farms (www.mulberryfarms.com)
    b. Silkworm Shop (www.silkwormshop.com)
    c. Coastal Silkworms (www.coastalsilkworms.com)
2. I prefer to buy large worms, as they are ready to dissect within two weeks, and are easy to raise. However, usually only medium worms are available.
3. For feeding and caring, generally follow the instructions given by the supplier. I found it to be best and easiest to raise the worms at room temperature. I also found it best to keep the worms in a dense environment (crawling all over each other).
4. Try to touch the worms as little as possible, if at all. They are very fragile, and if handled while molting, their molting layer can stick to them and cause them to just die. Most often, I never have to touch the worms while raising them. If a worm does die, I remove it with tweezers.

Dissecting Glands

1. Wait until the worm is just about to spin a cocoon. I have found that if you dissect the silk any earlier, it will be in much more of a gel state than a solution state.
2. Put the worm to be dissected in the fridge for 30 mins.
3. I usually cut off the head of the worm with scissors and allow the silk glands to flow out into buffer solution (see 4). If you would like to do a more proper dissection, dissect the worm in silkworm Ringer's solution, found in Yong-Ho Lee *et al*. Comparative Biochemistry and Physiology Part A 125 (2000) 95–104.
4. Allow the silk glands to soak in 10 mM phosphate buffer at pH 6.6 for 5 minutes. If you leave them too much longer, they may begin to solidify.
5. Peel off the gland epithelium from the silk, trying not to pinch or stretch the silk at all. I have found that it can be helpful to nick the outer edge of the bend, and allow the epithelium to begin to contract. It can then be easily grabbed and slowly pulled off.

6. Because the properties of the silk solution (concentration, crystallinity) change along the length of the gland, it is best just to use the middle section of the gland (between the two bends). Using a fresh blade, cut off the unused sections.
7. The middle section of the gland will be covered in a layer of sericin. Wash of the sericin by soaking the silk in a DI water bath for 20 mins, with very light shaking. Change the water after 10 mins.
8. You can now use the silk for whatever you want. If you want to load it into a syringe, fill the syringe with water or buffer, pull our the plunger, drop the silk in, turn the syringe and push out all the excess solution. You can then leave the solution for several hours to relax and homogenize.

Appendix D - Fiber Mechanical Tester

This is a low cost (~$1200) fiber testing system, set up to perform quasi-static testing of fibers.

Materials

1. World Precision Instruments FORT25 force transducer, 25 g
2. World Precision Instruments 3492 DIN (female) to unwired connector
3. Electronic Innovations EI-1040 dual instrumentation amplifier
4. Zaber Instruments KT-LA13A-S miniature linear actuator, 13 mm travel
5. Zaber Instruments TSB28-I travel stage, 28 mm
6. Zaber Instruments T-USB USB converter
7. National Instruments USB-6008 DAQ
8. Agilent E3630A triple output DC power supply
9. Wires and mounting hardware
10. Computer with 2 USB ports and LabView software
11. Hanging weights for calibrating the force transducer

Assembly

Connection Schematic

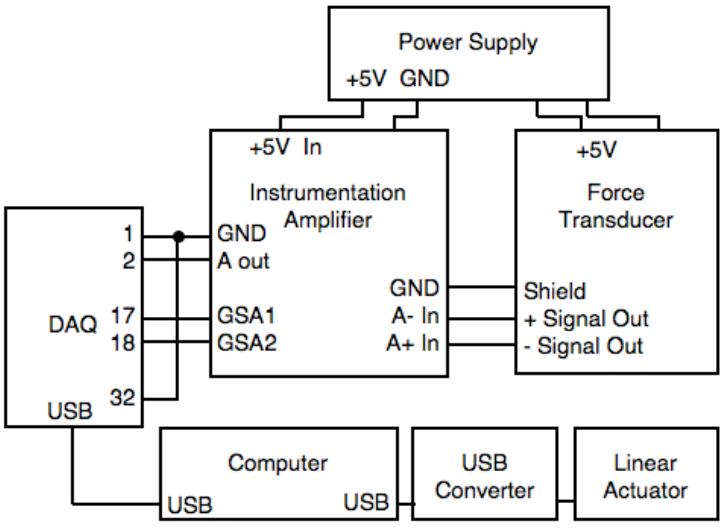

The instrumentation amplifier used here is a low cost, digitally switchable 10-100-1000X gain amplifier for transducers. The gain control is connected to the digital out of the

DAQ so that it can be software controlled. The force transducer connects to the analog in of the amplifier, and the analog output of the amplifier is connected to analog in on the DAQ. The linear actuator has its own USB-based software control.

System Mounting

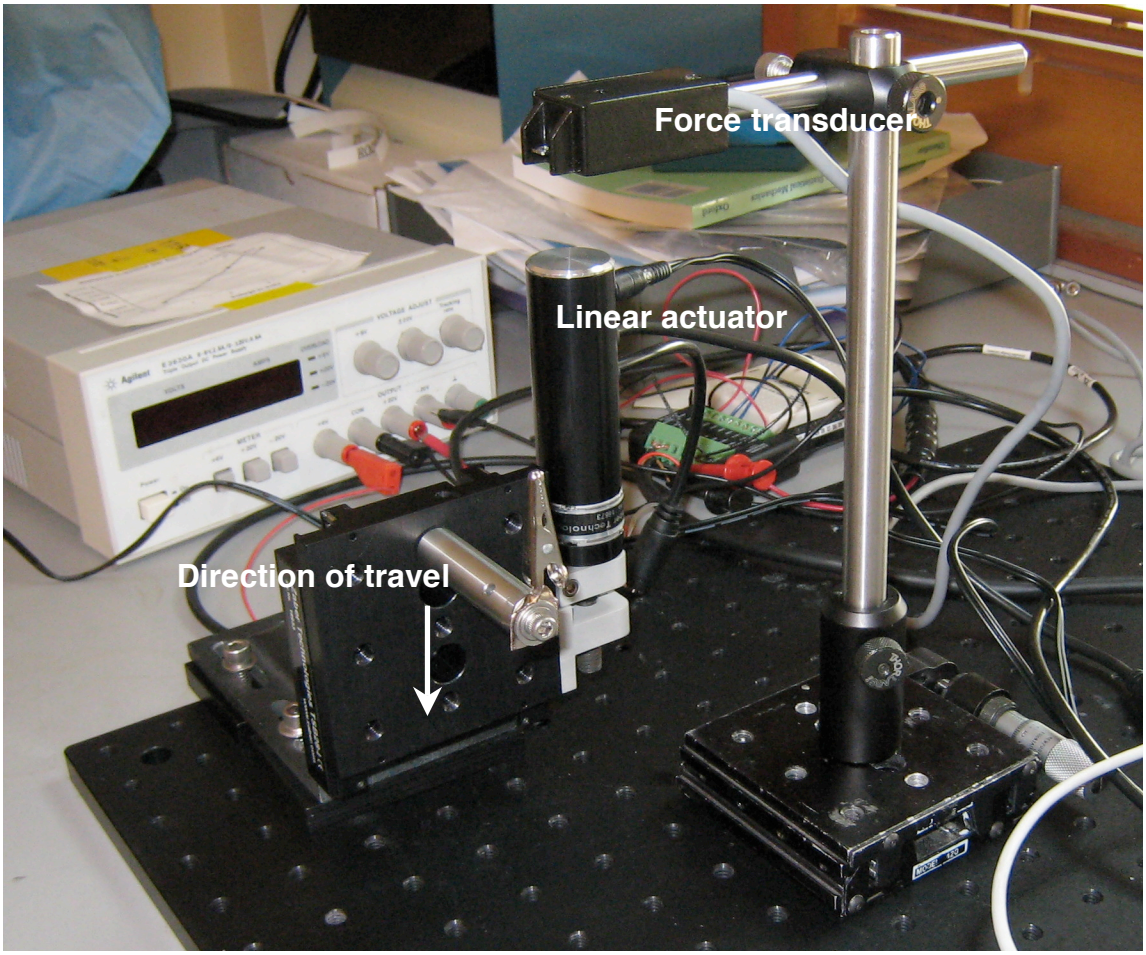

The system can be mounted in a number of ways. As shown above, the force transducer is mounted directly above the linear stage, which has an alligator clip attached. The linear actuation travels downward, extending the fiber.

Fiber Mounting

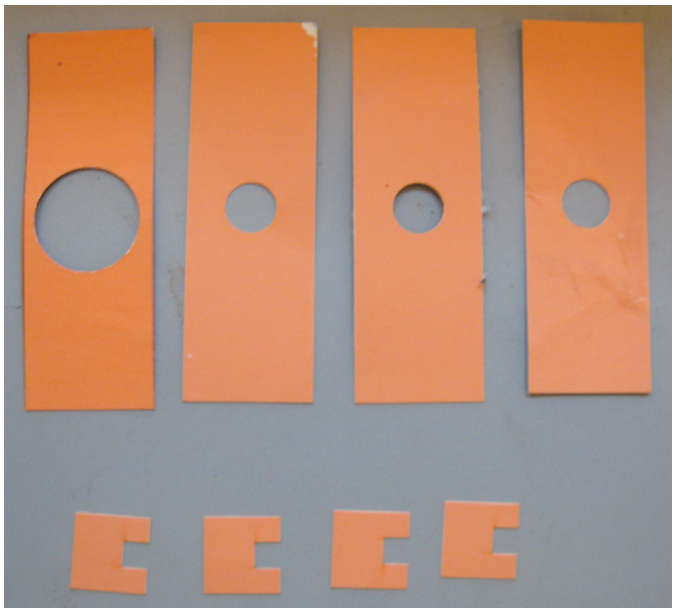

These are different cardboard mounts for fibers, with various gauge lengths (2 cm, 1 cm, 0.5 cm). Lay the fiber on the cardboard, and super glue it down at the edges of the center opening. Poke a paper clip through the top and hang the mount from the force transducer, then clip the bottom with the alligator clip. Before beginning the test, clip the edges of the mount.

Software

Below is the LabView software to operate the system, showing both the front panels and block diagrams:

1. Configure_DAQ.vi : A module to interface with the NI DAQ and open the connection for use.
2. Close_DAQ.vi : A module to close the DAQ when finished with use.
3. Calibration.vi : A program that allows you to sequentially add weights to the force transducer, record each voltage, and calculate the slope of the curve to obtain the calibration constant. All parameters are entered on the front panel.
4. Test_constantspeed.vi : The complete program for performing a mechanical test. All parameters are entered on the front panel.

Configure_DAQ.vi
C:\Documents and Settings\Administrator\Desktop\Fiber Tester\Configure_DAQ.vi
Last modified on 10/21/2009 at 7:20 PM
Printed on 10/27/2009 at 10:40 AM

Configure_DAQ.vi

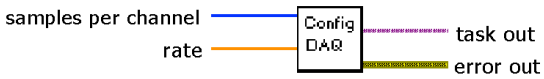

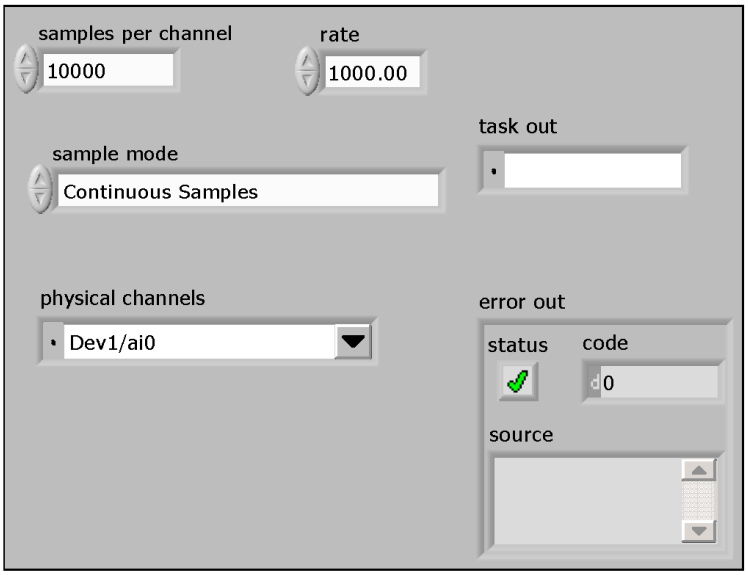

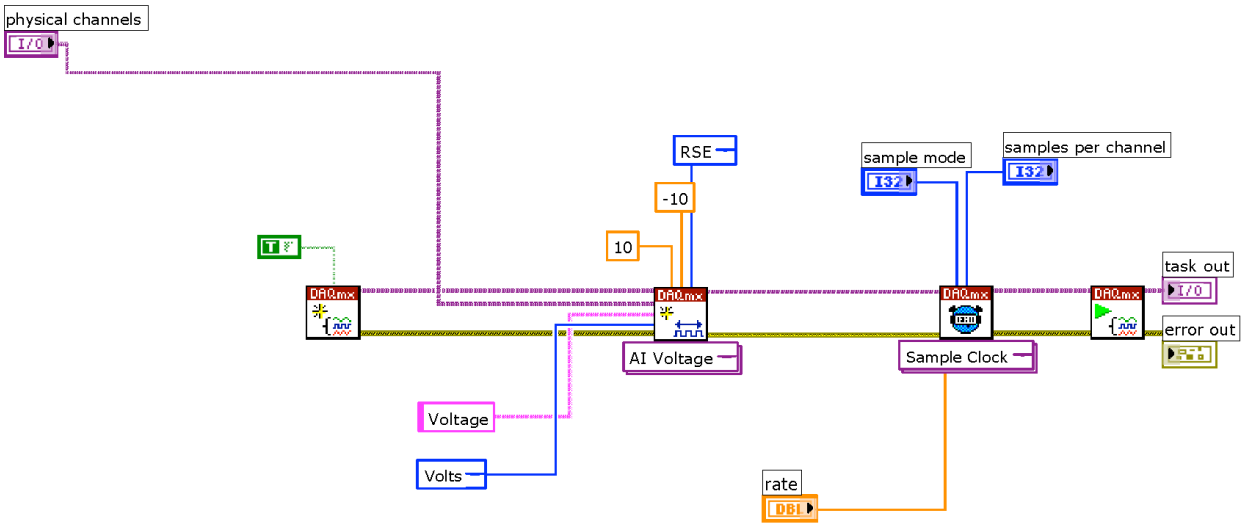

Close_DAQ.vi
C:\Documents and Settings\Administrator\Desktop\Fiber Tester\Close_DAQ.vi
Last modified on 10/19/2009 at 8:15 PM
Printed on 10/27/2009 at 10:40 AM

Close_DAQ.vi

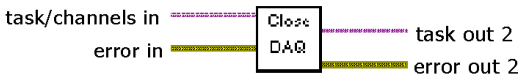

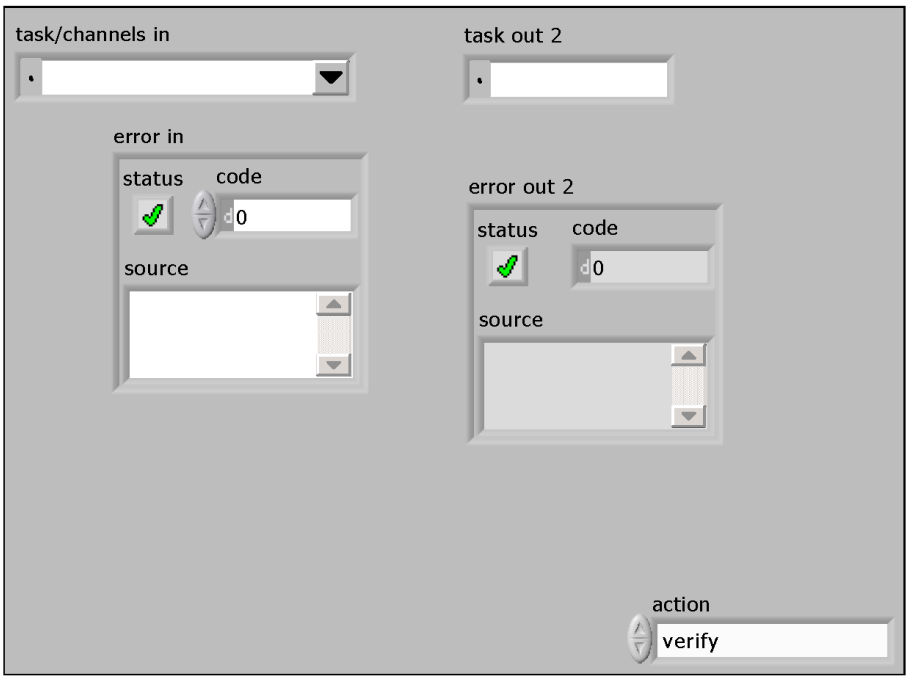

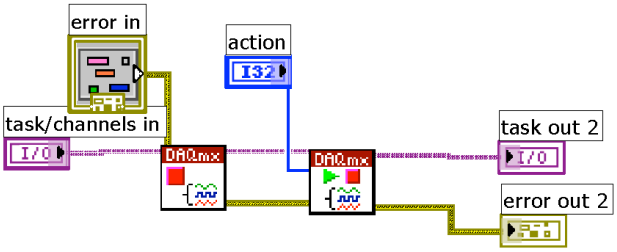

calibration.vi
C:\Documents and Settings\Administrator\Desktop\Fiber Tester\calibration.vi
Last modified on 10/23/2009 at 2:52 PM
Printed on 10/27/2009 at 10:39 AM

calibration.vi

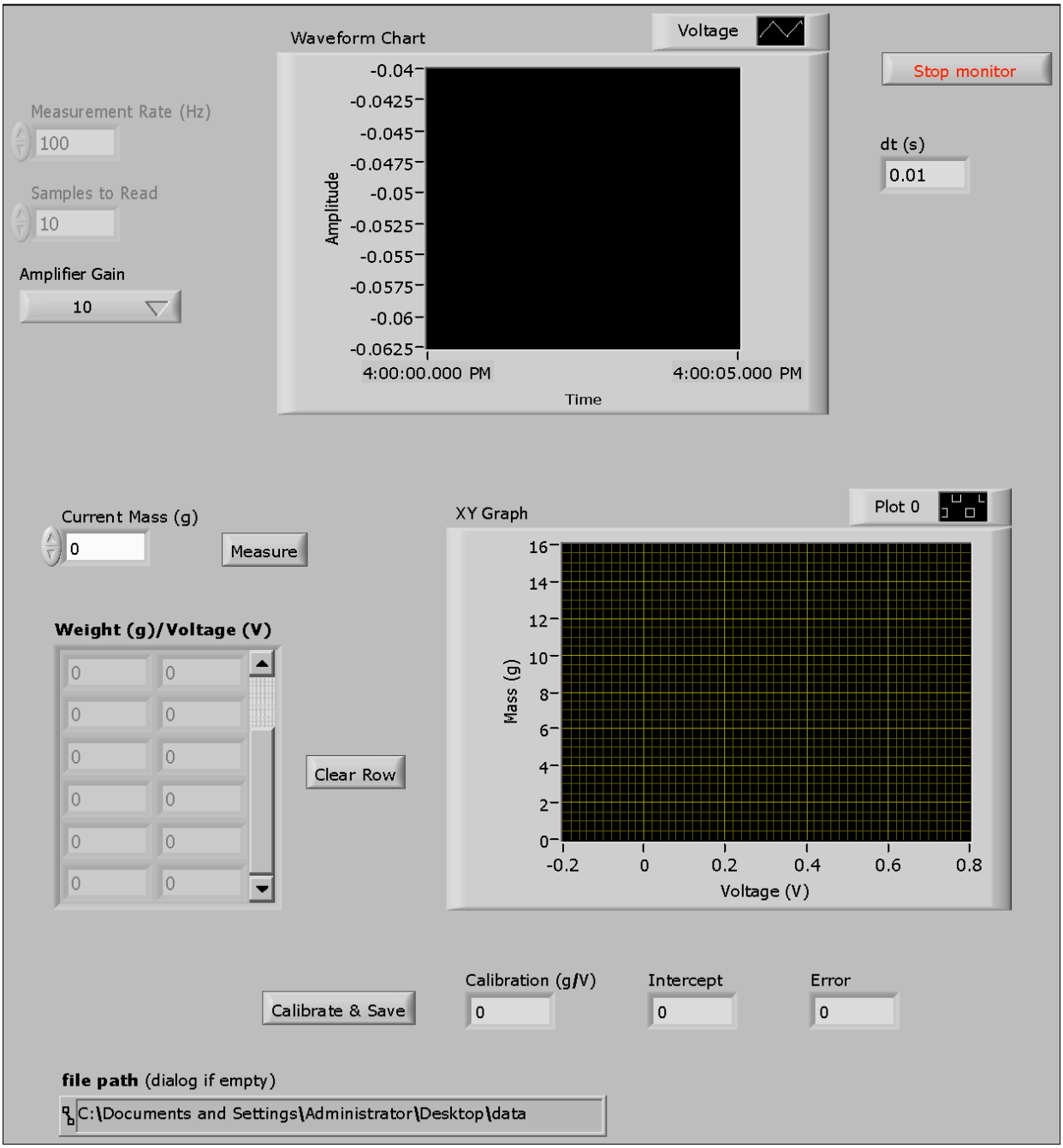

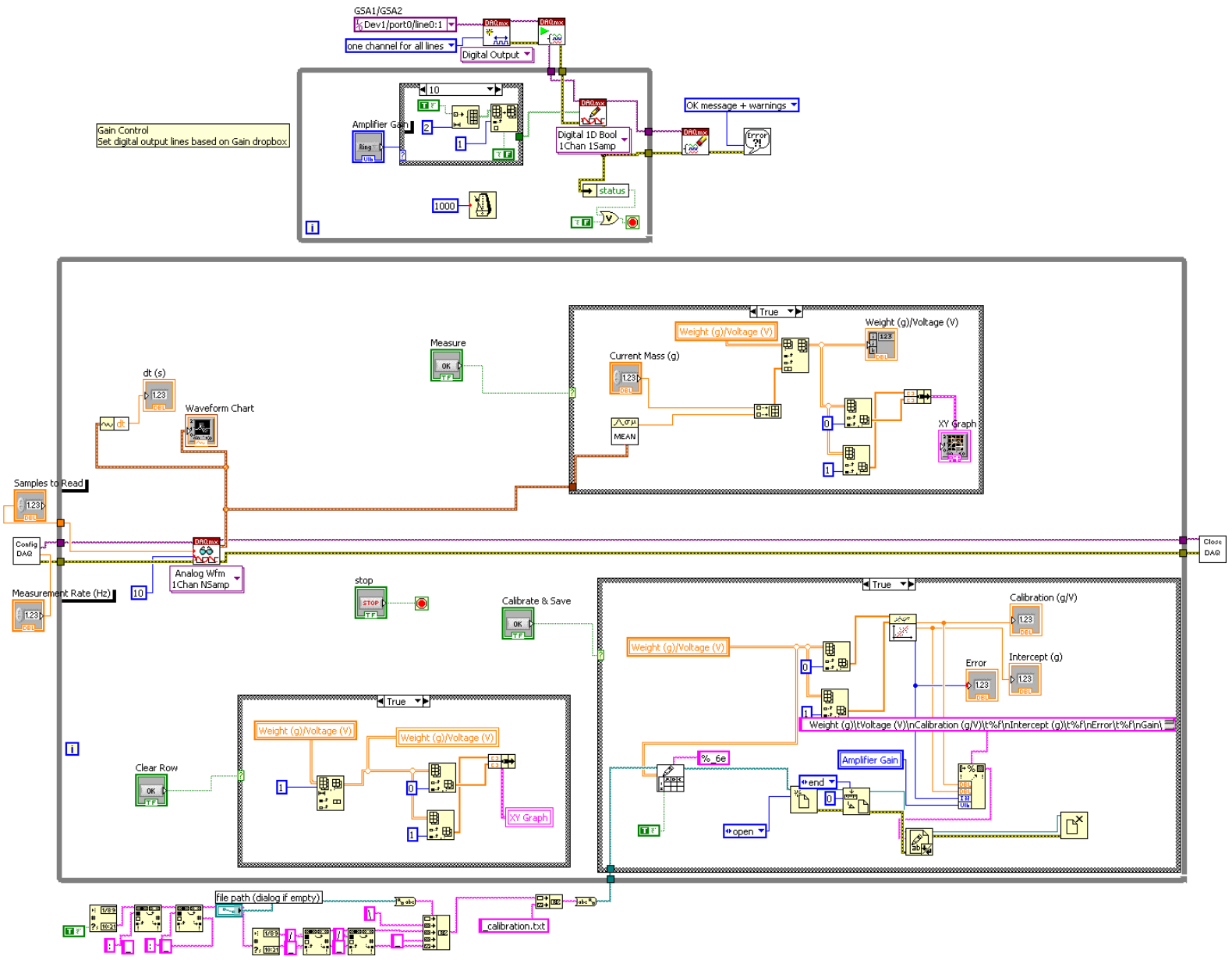
GSA1/GSA2
Dev1/port0/line0:1
one channel for all lines
Digital Output
Gain Control
Set digital output lines based on Gain dropbox
Amplifier Gain
Digital 1D Bool 1Chan 1Samp
OK message + warnings
status
1000
Measure
dt (s)
Waveform Chart
True
Weight (g)/Voltage (V)
Current Mass (g)
MEAN
XY Graph
Samples to Read
Config DAQ
Analog Wfm 1Chan NSamp
Measurement Rate (Hz)
10
stop
Calibrate & Save
Close DAQ
Clear Row
Calibration (g/V)
Intercept (g)
Error
Weight (g)\tVoltage (V)\nCalibration (g/V)\t%f\nIntercept (g)\t%f\nError\t%f\nGain\
%.6e
Amplifier Gain
end
open
file path (dialog if empty)
_calibration.txt

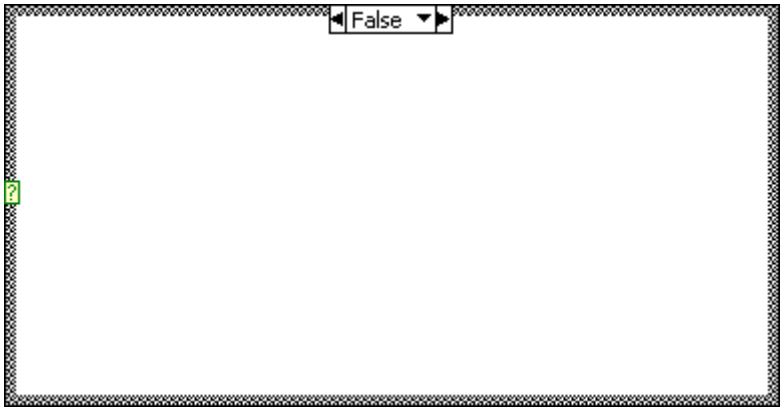
False

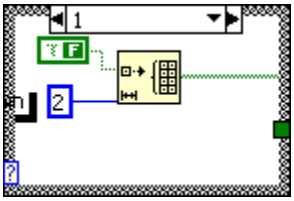
1
2

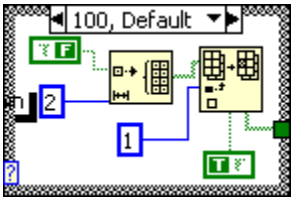
100, Default
2
1

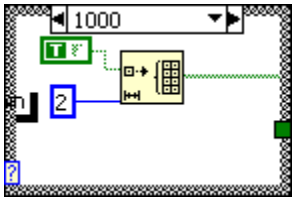
1000
2

Test_constantspeed.vi
C:\Documents and Settings\Administrator\Desktop\Fiber Tester\Test_constantspeed.vi
Last modified on 10/24/2009 at 1:02 PM
Printed on 10/27/2009 at 10:37 AM

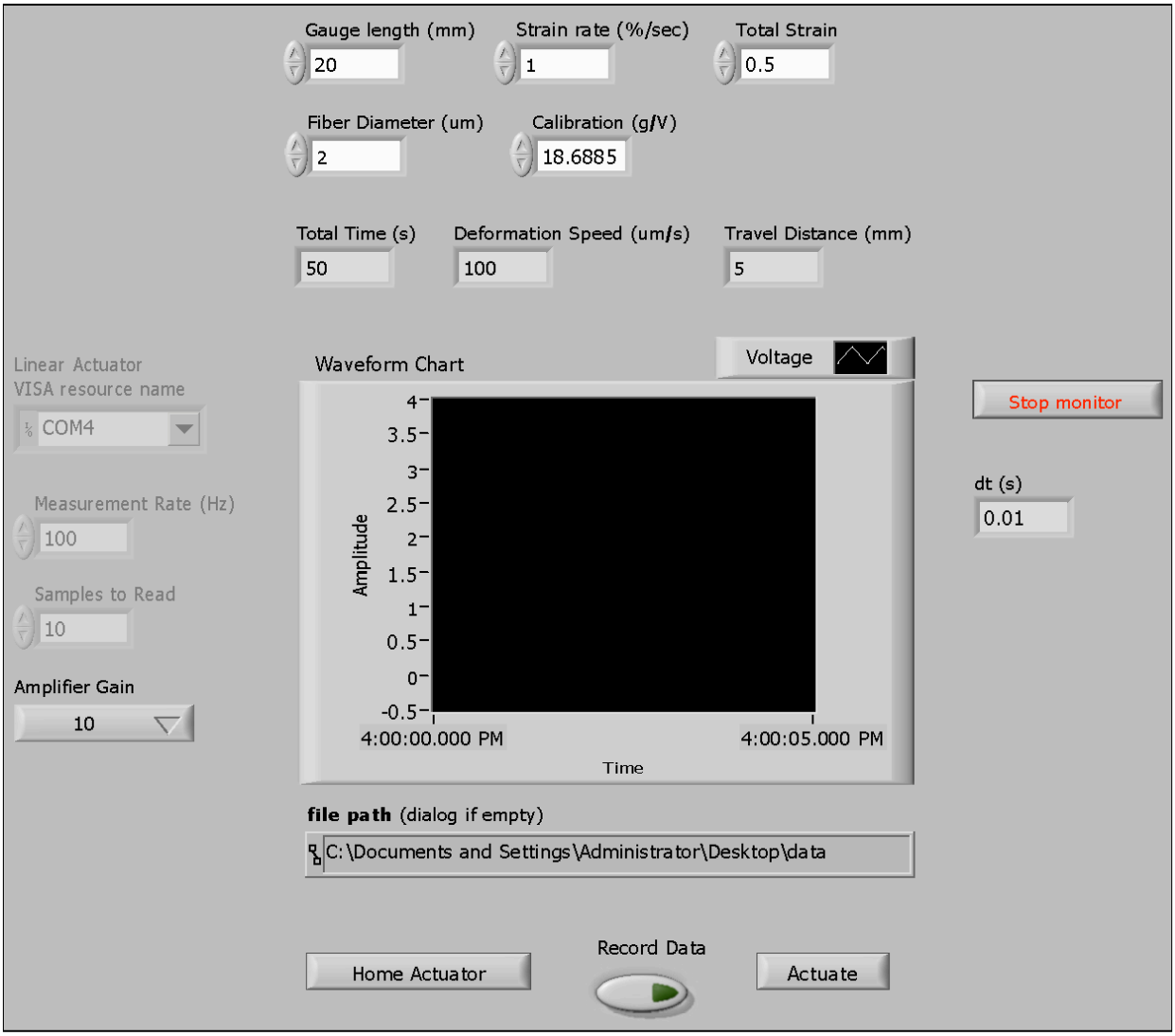

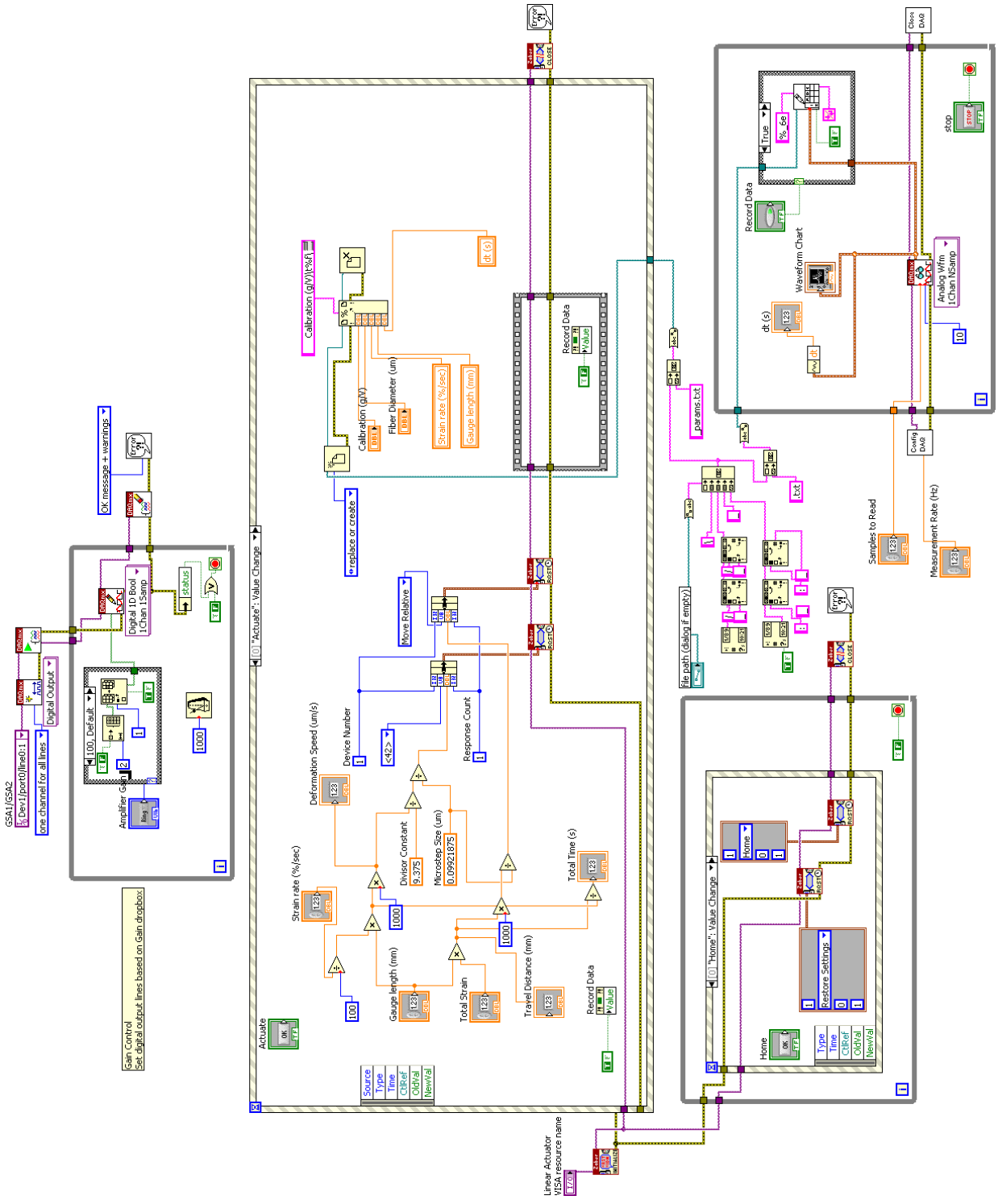
GSA1/GSA2
0:Dev1/port0/line0:1
one channel for all lines
Digital Output
Digital 1D Bool 1Chan 1Samp
OK message + warnings
status
100 Default
Amplifier Gain
1000
Gain Control
Set digital output lines based on Gain dropbox
(0) "Actuate": Value Change
Actuate
Calibration (g/V)(%f\
Calibration (g/V)
Fiber Diameter (um)
Strain rate (%/sec)
Gauge length (mm)
dt (s)
Record Data
Value
+replace or create+
Move Relative
Deformation Speed (um/s)
Device Number
<42>
Response Count
Divisor Constant
9.375
Microstep Size (um)
0.09921875
Total Time (s)
Strain rate (%/sec)
Gauge length (mm)
Total Strain
Travel Distance (mm)
Record Data
Value
100
1000
Source
Type
Time
CtlRef
OldVal
NewVal
Linear Actuator VISA resource name
params.txt
file path (dialog if empty)
.txt
(0) "Home": Value Change
Home
Restore Settings
Home
Type
Time
CtlRef
OldVal
NewVal
Record Data
True
%.6e
Waveform Chart
dt (s)
Analog Wfm 1Chan NSamp
stop
Close DAQ
Config DAQ
Samples to Read
Measurement Rate (Hz)

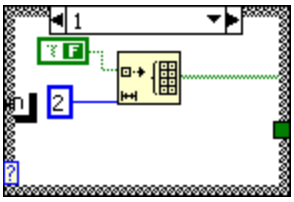
1
F
2
?

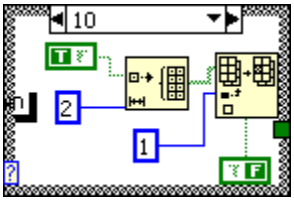
10
T
2
1
F
?

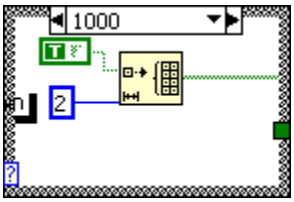
1000
T
2
?

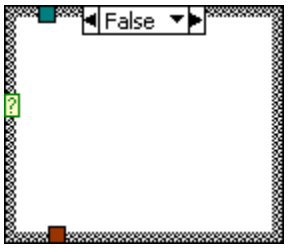
False
?